

Thermal stability and reaction of metallic multilayers

Dissertation
zur Erlangung des Doktorgrades
der Mathematisch-Naturwissenschaftlichen Fakultäten
der Georg-August-Universität Göttingen

vorgelegt von
Constantin Buzau Ene
aus Buzau, Rumänien

Göttingen 2007

D7

Referent: Prof. Dr. Reiner Kirchheim

Korreferent: Prof. Dr. Guido Schmitz

Tag der mündlichen Prüfung: 19.12.2007

To Emilia and Vlad

Contents

1	INTRODUCTION.....	1
2	PHYSICAL BACKGROUND.....	3
2.1	THE PHYSICS OF SOLID STATE INTERREACTIONS.....	3
2.1.1	<i>Growth kinetics.....</i>	3
2.2	MULTILAYER INTERFACE ANALYSIS.....	8
3	EXPERIMENTAL METHODS.....	11
3.1	FIELD ION MICROSCOPY AND ATOM PROBE TOMOGRAPHY	11
3.1.1	<i>Field Ion Microscopy.....</i>	11
3.1.2	<i>Atom Probe Tomography.....</i>	16
3.1.3	<i>Parameters used for APT analysis.....</i>	19
3.2	DATA ANALYSIS	20
3.2.1	<i>Layered structure's reconstruction.....</i>	20
3.2.2	<i>One-dimensional concentration profiles.....</i>	23
3.2.3	<i>Two-dimensional composition maps</i>	24
3.3	COMPLEMENTARY INVESTIGATION METHODS	25
4	SAMPLE PREPARATION.....	27
4.1	SUBSTRATES PREPARATION.....	27
4.1.1	<i>FIM/TAP sample preparation.....</i>	27
4.1.2	<i>Planar samples</i>	28
4.2	DEPOSITION PROCESS	29
4.3	FOCUSED ION BEAM TEM AND FIM/TAP SAMPLE PREPARATION.....	31
4.3.1	<i>TEM sample preparation</i>	33
4.3.2	<i>APT/FIM sample preparation.....</i>	35
4.4	THERMAL TREATMENTS	36
5	INVESTIGATION OF COPPER/PERMALLOY GMR MULTILAYER STRUCTURES....	37
5.1	GIANT MAGNETO-RESISTANCE	37
5.2	STATE OF THE ART OF GMR EFFECT INVESTIGATIONS.....	41
5.3	MOTIVATION OF THE STUDY.....	42
5.4	EXPERIMENTAL RESULTS IN CU/PY MULTILAYERS.....	44
5.4.1	<i>As-prepared state</i>	44

5.4.2	<i>Annealed state investigations</i>	48
5.4.2.1	Volume diffusion	49
5.4.2.2	Grain boundary diffusion.....	54
5.5	PHYSICAL INTERPRETATION.....	60
5.6	CONCLUSIONS.....	69
6	INVESTIGATION OF ALUMINIUM/COPPER MULTILAYER STRUCTURES.....	71
6.1	MOTIVATION AND STATE OF THE ART	71
6.2	AL–CU SYSTEM.....	74
6.3	EXPERIMENTAL RESULTS IN AL/CU MULTILAYERS	75
6.3.1	<i>As–prepared state</i>	75
6.3.2	<i>Thermally treated samples</i>	78
6.4	LAYER MISMATCH AND ELASTICITY ON CURVED SUBSTRATES.....	87
6.5	LAPLACE TENSION	98
6.6	STRESS IMPACT ON THE DIFFUSION RATE	99
6.7	DISCUSSION AND CONCLUSIONS	102
7	SUMMARY AND OUTLOOK.....	107
	BIBLIOGRAPHY	109
	APPENDIX: MACROSCOPIC EXPERIMENT ON THE INTERDIFFUSION OF CU/AL	
	COUPLE	117
	ACKNOWLEDGEMENTS.....	121
	LEBENS LAUF	123

1 Introduction

Thin film systems trigger tremendous research activities both for technological applications as well as for fundamental science. The stacking of different thin films makes it possible to create multilayers with new electrical, magnetical, optical, and mechanical properties which are distinct from those of the constitutive bulk materials.

Compared to bulk solid state interreaction where the volume is the important feature, surfaces and interfaces are playing a more important role in the case of thin films. Thus, knowing the interface morphology is very useful for technological and scientific problems.

An essential point in this regard is the influence of the preparation, on the quality and functionality of the thin films. Another very important aspect is the stress development due to lattice mismatch when two materials with different lattice constants are deposited one on top of another.

In this work the interreaction of thin films is investigated by means of Field Ion Microscopy, Atom Probe Tomography and Transmission Electron Microscopy. The influence of microstructure and stress on the reaction mechanism is exemplified on two different systems: the *Cu/Py* multilayers exhibiting Giant Magneto-Resistance effect (*Py* = $Ni_{79}Fe_{21}$ known as *Permalloy*) and *Al/Cu* sandwich type thin films investigated in the early stages of interreaction. Both systems are interesting for the understanding of fundamentals of solid state reaction processes but they are at the same time important constituents of highly developed technological applications.

The GMR effect is used for numerous electronic devices in data processing (MRAM, hard-disks read heads) or in automotive industry (revolution counter for

ABS-system), while *Al* and *Cu* thin films are the two most important components of current day metallization in semiconductor devices.

Film thicknesses of a few nanometers only are applied both for sensors used in industrial applications as well as for interconnects of integrated circuits. Thus, the thermal stability is an important feature since a fast reaction due to temperature exposure may lead to early device failure.

After this introductory text, chapter 2 presents a short theoretical overview on solid state interreactions and interface description based on the Cahn-Hilliard model. In chapter 3, the experimental methods and the relevant data analysis tools are introduced. The preparation techniques and the parameters used for sample fabrication are presented in chapter 4. The next two chapters constitute the core of the present work. The results obtained on the investigation of *Cu/Py* multilayers are presented and discussed in chapter 5. Also the conclusions concerning the GMR effect breakdown due to temperature exposure are provided here. Chapter 6 presents the experimental results obtained with *Al/Cu* layer systems. These results are discussed using a newly derived analytic model of stress development during the solid state reaction of thin films deposited on a spherical substrate. The influence of Laplace tension on reaction is also discussed as a reasonable explanation of the experimental observations. Chapter 7 summarises this work and gives some hints for further investigations.

2 Physical background

2.1 *The physics of solid state interreactions*

The physics of solid state interreactions is briefly described in this chapter as a starting point for the investigations on the reaction of thin metallic multilayer systems. Reactions in thin films are distinguished by sequential growth, the lack of equilibrium phases or most commonly the observation of only one growing phase. Sometimes the growth of metastable phases is observed in contrast to bulk interdiffusion couples for which simultaneous parabolic growth of all the equilibrium phases is usually noticed. The question whether the first product is determined by a competition in growth or by selective nucleation remains unresolved even after decades of intensive research.

2.1.1 Growth kinetics

The general reaction between two components in layer geometry may be completely characterized by the evolution of a one-dimensional composition profile as shown in Fig. 2–1. As a consequence of the layer geometry, any further thickening of the reaction zone requires atomic transport through the product phases. The resulting diffusion problem was solved by Kirkaldy [Kirkaldy 58] and by Kidson [Kidson 61], assuming that compositions at the interfaces match those of local equilibrium and furthermore, each phase is characterized by a composition independent interdiffusion coefficient.

From the balance of related currents (conservation of matter at interfaces), the movement of an interface can be determined as follows:

$$\frac{dx_k}{dt} = \frac{j_k - j_{k-1}}{c_i^{(k)} - c_f^{(k-1)}} \quad (2.1)$$

with x_k being the position of the interface for the phase k , j_k the current through the phase k . The concentrations $c_i^{(k)}$ and $c_f^{(k)}$ determines the existence range of product phases.

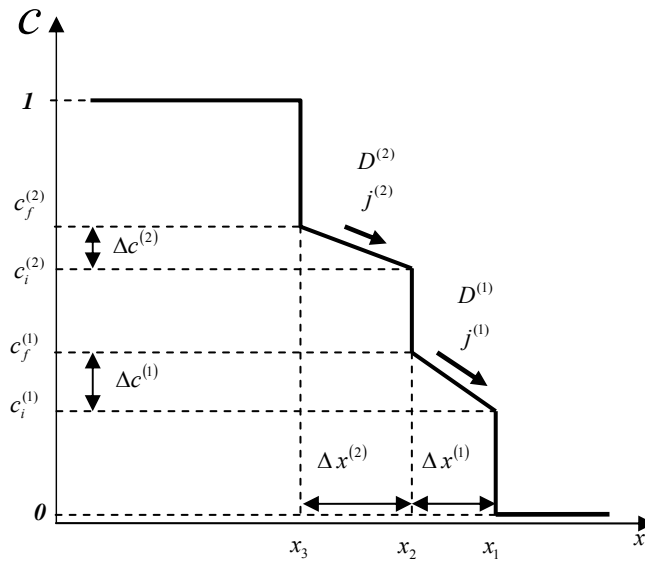


Fig. 2–1: Schematic composition profile through a reaction zone with two reaction products. For simplicity, the solubility of the terminating phases is assumed to be negligible (Schmitz, 2001).

The thickness of the phase layer is defined by the relative position of its two interfaces. Hence, the growth of a phase depends not only on the transport through itself, but also on that through the neighbouring phase, indicating the competitive nature of phase formation. That means, despite the stability in equilibrium conditions, a phase may shrink in competition with its neighbouring phases.

Using the situation sketched in Fig. 2–1, the competition between phases might be discussed in more detail. As seen, there are two intermetallic phases

competing in the interreaction. For simplicity, the solubility of the terminating phases is assumed to be negligible. In this case, the growth of the compound layers is determined by the motion of the phase interfaces according to the following equations [Gösele 82, Schmitz 01]:

$$\frac{d\Delta x^{(1)}}{dt} = \frac{dx_1}{dt} - \frac{dx_2}{dt} = C_{1,1} \cdot j^{(1)} + C_{1,2} \cdot j^{(2)} \quad (2.2)$$

$$\frac{d\Delta x^{(2)}}{dt} = \frac{dx_2}{dt} - \frac{dx_3}{dt} = C_{2,1} \cdot j^{(1)} + C_{2,2} \cdot j^{(2)} \quad (2.3)$$

with the coefficients $C_{1,1}$, $C_{1,2} = C_{2,1}$ and $C_{2,2}$ being:

$$C_{1,1} = \frac{1}{c_i^{(2)} - c_f^{(1)}} + \frac{1}{c_i^{(1)}} \quad (2.4)$$

$$C_{2,2} = \frac{1}{c_i^{(2)} - c_f^{(1)}} + \frac{1}{1 - c_f^{(2)}} \quad (2.5)$$

$$C_{1,2} = C_{2,1} = -\frac{1}{c_i^{(2)} - c_f^{(1)}} \quad (2.6)$$

The current ratio $r := j^{(1)} / j^{(2)}$ reflects the growth competition between the two product compounds. As a consequence of equation (2.2), the growth of compound (1) requires:

$$r > r_1 := -C_{1,2} / C_{1,1} \quad (2.7)$$

Similarly, for the growth of compound (2) according to equation (2.3) it is necessary that:

$$r < r_2 := -C_{2,2} / C_{1,2} \quad (2.8)$$

It must be admitted that the diffusion controlled kinetics does not predict a phase to shrink away. Assuming initially a current ratio $r < r_1$, at first compound (1) will shrink. But at the same time according to the Ficks law $j^{(1)} = -D^{(1)} / \Delta x^{(1)}$,

the current $j^{(1)}$ increase gradually. Thus, the ratio will reach r_1 and the compound starts growing again before it can disappear. Finally, a steady state of constant current ratio is reached. The analogous behaviour is expected for the opposite initial situation $r > r_2$. Therefore, in the steady state both compounds will grow according to a parabolic time law.

The parabolic growth is definitely one of the best confirmed laws of material science. Nevertheless, this is only valid in late reaction stages. For the thin film reactions, the steady state is usually never reached because the unreacted material supply is limited. Furthermore, experimental time exponents significantly deviate from the parabolic growth law.

The difficulties arise from the fact that the transport rates are taken to be infinite at the very beginning of interreaction. To avoid this unphysical assumption, usually reaction barriers at the interfaces are taken into account. These reaction barriers will limit the maximum atomic current. For that, Fick's First Law is subjected to the following modification:

$$j = -\frac{D\Delta c}{\Delta x + D/k} \quad (2.9)$$

The reaction constant k describes the average transport properties at both interfaces of a layer. Thus, in the very early stage, when Δx in the denominator of equation (2.9) is still negligible, j is predicted to be constant and phase growth should be proportional to the annealing time. Linear growth regimes are indeed observed experimentally, particularly in the case of oxidation reactions and the formation of some silicides, but usually not in the case of metals.

Gösele and Tu demonstrated that interfacial barriers in binary A/B diffusion couples are sufficient to explain the suppression of phases in early reaction stages for a sufficiently thin diffusion zone [Gösele 82]. This is seen from equations (2.2) and (2.3), if atomic currents in the form of equation (2.9) are introduced. In the case that the transport through the boundaries of compound (1) is very sluggish, so that

$$\frac{k^{(1)}\Delta c^{(1)}}{k^{(2)}\Delta c^{(2)}} < r_1 \quad (2.10)$$

compound (1) is at first suppressed. Only after compound (2) has grown to reach the diffusion controlled regime ($\Delta x^{(2)} > D^{(2)} / k^{(2)}$), j_2 may be sufficiently decreased, resulting in:

$$r = \frac{k^{(1)}\Delta c^{(1)}\Delta x^{(2)}}{D^{(2)}\Delta c^{(2)}} = r_I \quad (2.11)$$

Thus, compound (2) must have reached a critical thickness $\Delta x_{crit.}^{(2)} = r_I D^{(2)} \Delta c^{(2)} / k^{(1)} \Delta c^{(1)}$ before compound (1) can start growing.

The experimental proof of the theory is rather difficult although the suppression of phases is successfully explained. A large number of parameters must be known for a quantitative check. In particular, it is difficult to determine interfacial reaction constants and in addition they seem to depend on preparation conditions [Gösele 82].

On the other hand, the effect of interfacial barriers for reactions between metals is still a matter of discussion, since in a metallic system diffusion coefficients of the compounds often differ by several orders of magnitude. Regarding the phase thicknesses predicted for the steady state of diffusion, fast growing phases may reach a thickness of several microns before slower ones become visible in the reaction zone. The very simple rule stated by d'Heurle, that the phase of highest diffusivity is formed first, yields a correct prediction for the major number of cases [d'Heurle 97]. Hence, minor factors like interfacial reaction barriers or thermodynamic driving forces are overwhelmed by a large difference in compound diffusivities.

2.2 Multilayer interface analysis

The Cahn-Hilliard approach can be used to describe inhomogeneous thermodynamical systems [Cahn 58]. This approach supposes a binary solution A/B with an inhomogeneous concentration c , the mole fraction of the B component. Furthermore, it is supposed that in the regions with non-uniform composition the local free energy per volume f depends not only on the local composition, but also on the composition of the surrounding volume. Thus, expanding the local free energy in a Taylor series of local composition derivatives, leads to a relation between free energy and volume f_0 (for the homogeneous solution) and an additional “gradient energy”, as named by Cahn and Hilliard, $\kappa(\nabla c)^2 + \dots$ depending on the square of the local composition gradient. With N_V the number of atoms per unit volume, the total free energy of volume V is:

$$F = N_V \int (f_0 + \kappa(\nabla c)^2 + \dots) dV \quad (2.12)$$

where κ is a positive constant called gradient energy coefficient.

For a flat interface of cross-sectional area A between coexisting α and β phases the total free energy can be written as follows if higher order terms are neglected:

$$F = A \cdot N_V \int_{-\infty}^{+\infty} \left[f_0(c) + \kappa \left(\frac{dc}{dx} \right)^2 \right] dx \quad (2.13)$$

The specific interfacial free energy σ , defined according to [Cahn 58] as the difference per unit area of interface between the actual free energy of the system and the volume free energies of the adjacent phases, can be written:

$$\sigma = N_V \int_{-\infty}^{+\infty} \left[\Delta f(c) + \kappa \left(\frac{dc}{dx} \right)^2 \right] dx \quad (2.14)$$

with

$$\Delta f(c) = c[\mu_B(c) - \mu_B(e)] + (1-c)[\mu_A(c) - \mu_A(e)] \quad (2.15)$$

$\mu_A(c)$ and $\mu_B(c)$ are the chemical potentials of a homogeneous mixture of the components A and B and $\mu_A(e)$ and $\mu_B(e)$ the chemical potentials of A and B for the two phases forming the interface at equilibrium.

The equilibrium state is characterized by a minimum in surface energy. According to Eq. 2.14 the more diffuse the interface is, the smaller is the contribution of the gradient energy term $\kappa \left(\frac{dc}{dx} \right)^2$ to the interfacial free energy σ .

On the other hand, a more diffuse interface will increase the term $\Delta f(c)$. The composition at equilibrium minimizes Eq. 2.14 which implies after using the Euler[§] equation:

$$\frac{dc}{dx} = \sqrt{\frac{\Delta f}{\kappa}} \quad (2.16)$$

Assuming a regular solution model with symmetrical concentration dependence, the equilibrium solubility far away from the interface is:

$$k_B T = \frac{(2c_e - 1) \cdot \omega}{\ln \left[\frac{c_e}{1 - c_e} \right]}, \quad \text{with} \quad \omega = 2k_B T_c \quad (2.17)$$

The gradient energy coefficient is derived by Cahn from the regular solution model as:

[§] Identifying the integrant in Eq. 2.14 as I , the minimum of σ is obtained if the equation $I - (dc/dx)[\partial I / \partial (dc/dx)] = 0$ is satisfied.

$$\kappa = \frac{\omega \lambda^2}{2} \quad (2.18)$$

with λ being the “interaction distance” for the energy in a concentration gradient. Thus, for a regular solution (subscript R) the total free energy in a volume V can now be written as:

$$F_R = N_V \int_V \left[f_R + \frac{\omega \lambda^2}{2} (\nabla c)^2 \right] dV \quad (2.19)$$

The interfacial free energy of the regular solution σ_R has the following expression:

$$\sigma_R = 2 \cdot N_V \cdot \lambda \cdot k_B \cdot T_c \cdot \sigma_r \quad (2.20)$$

The term σ_r is a reduced interfacial energy defined as

$$\sigma_r = \int_{c_e}^{1-c_e} \left(\frac{\Delta f_R}{k_B \cdot T_c} \right)^{\frac{1}{2}} dc \quad (2.21)$$

with

$$\Delta f_R = -\omega(c - c_e)^2 + k_B \cdot T \left[c \ln \frac{c}{c_e} + (1 - c) \ln \left(\frac{1 - c}{1 - c_e} \right) \right] \quad (2.22)$$

For the interface thickness the following expression can be derived:

$$l_R = \sqrt{\frac{\kappa}{\Delta f_R}} = \lambda \sqrt{\frac{\omega}{2 \Delta f_R}} \quad (2.23)$$

Finally, the interface thickness depends on two parameters: the gradient energy term κ and the critical temperature T_c defining the regular solution.

3 Experimental Methods

In this chapter Atom Probe Tomography (APT), a combination of Field Ion Microscope (FIM) with a Position Sensitive Detector (PSD), and its physical principle will be described. The relevant data analysis tools are presented and a short overview about the other characterization techniques used in this work is given.

3.1 Field Ion Microscopy and Atom Probe Tomography

Since the invention by E. W. Müller in 1951, the Field Ion Microscopy and later in combination with PSD detector – the Tomographic Atom–Probe (TAP), have been proven as valuable tools in surface physics and physical metallurgy. Owing to its chemical analysis of outstanding resolution, the method is able to solve several critical problems of reaction kinetics [Miller 96, Schmitz 07].

3.1.1 Field Ion Microscopy

The Field Ion Microscope gives the possibility to image the surface of an electrically conducting sample by field ionization with a magnification of 10^6 – 10^7 . The image formation in the Field Ion Microscope differs considerably from those of optical and electron microscopes and is remarkable for its simplicity. The image is produced by applying a high voltage to the specimen with respect to a phosphorus screen in the presence of the so-called imaging gas (*Ne*, *He*,

H_2 , Ar or some mixtures of them), as sketched in Fig. 3–1 on the left–hand side. The conducting material to be investigated is prepared as a tip with a very small radius, usually in the $20 - 100 \text{ nm}$ range. During the investigation the tip–like specimen must be cooled down to cryogenic temperatures, usually of $20 - 100 \text{ K}$, in ultra high vacuum with $\sim 10^{-7} \text{ Pa}$.

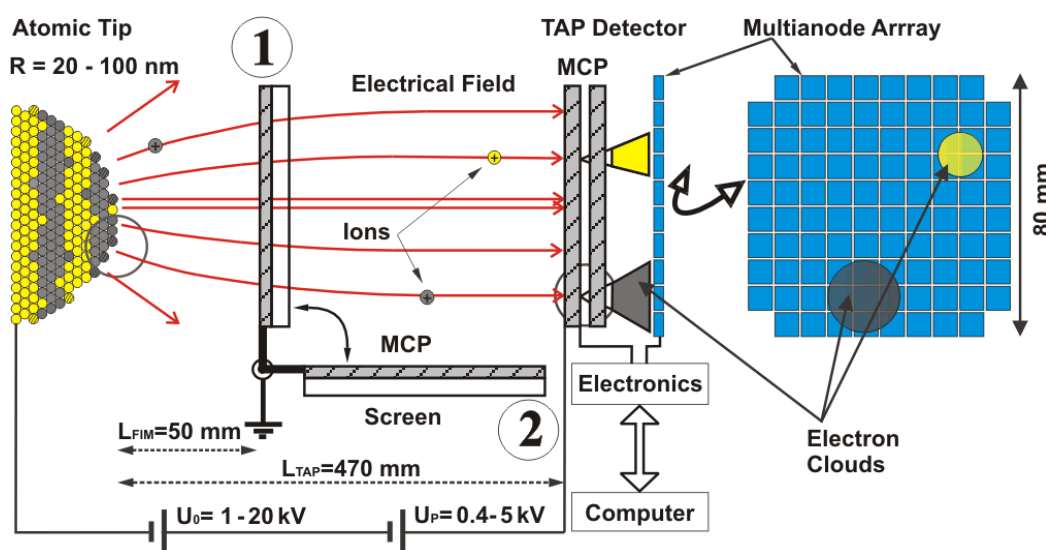


Fig. 3–1: Schematic drawing of the Field Ion Microscope (left–hand side) and the Tomographic Atom–Probe (right–hand side). In the FIM mode the screen is turned upwards (pos. 1) in front of the specimen and the imaging gas is leaked into the instrument chamber. For the 3D analysis in TAP mode the screen is turned downwards (pos. 2), the chamber is evacuated and the field evaporated ions from the specimen's surface are sensed by the position sensitive detector (PSD) and recorded with the help of electronic and computer systems.

The basic principle is the generation of a high electric field between the sample and the phosphor screen. In order to amplify the incoming events Chevron–type Microchannel Plates (MCP) are placed directly in front of the phosphor screen. The tip to MCP distance is usually $R = 50 - 200 \text{ mm}$. The very high electric field, which might reach up to 50 V/nm , is provided by a positive high voltage, $U_0 = 1 - 20 \text{ kV}$ applied to the small tip–like specimen. The electric field which is induced at the tip apex by the high voltage applied is:

$$E = \frac{U_0}{\beta \cdot R} \quad (3.1)$$

The factor β depends on the geometrical shape of the tip. Its value is usually between 5 and 7 [Miller 96] and takes into account the deviation of the tip from an ideal hemispherical cap. The main chamber of the instrument in which the specimen is investigated is backfilled with imaging gas to approximately $5 \cdot 10^{-3}$ Pa. If the chamber is continuously evacuated, the imaging gas is leaked in order to maintain the above mentioned pressure. The imaging gas atoms become polarized and are attracted towards the tip surface due to the inhomogeneous electric field. By inelastic collisions with the surface atoms of the tip, the polarized atoms lose their kinetic energy. In this way, they are cooled down to the tip surface temperature and trapped in the ionization zone, approximately 0.5 nm above the tip surface (field induced adsorption).

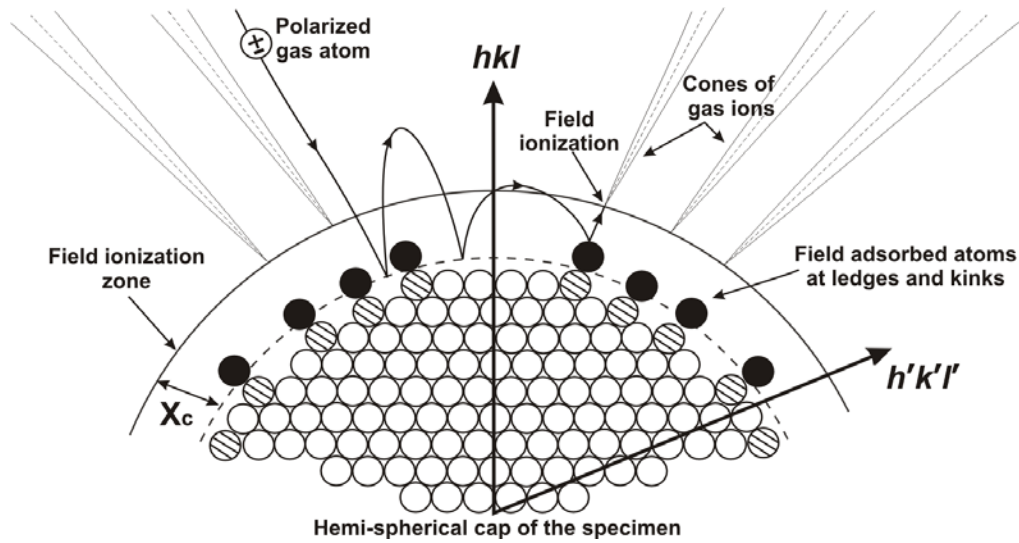


Fig. 3–2: Schematic drawing of the field ionization process of gas atoms over the high field regions of the hemi-spherical tip surface. Protruding atoms are shaded.

If the field is sufficiently high (imaging gas specific field ionisation strengths, e.g. He $\sim 44 \text{ V/nm}$, Ne $\sim 35 \text{ V/nm}$, H $\sim 22 \text{ V/nm}$), gas atoms reaching the surface become field adsorbed in high field sites above the prominent surface atoms [Miller 89]. Further gas atoms arriving subsequently will migrate along the

surface above the field adsorbed layer until they are ionized by the quantum–mechanical tunnelling process of field ionization as sketched in Fig. 3–2 [Al–Kassab 02].

In this process, an electron from the gas atom tunnels through the surface potential barrier into a vacant energy level in the specimen, leaving a positively charged gas ion above the surface. These ions are accelerated along the field lines from the sample towards the MCP/phosphorus screen, where they form a highly magnified, projection image of the specimen’s surface at which they were ionised.

Ions impinging at the front side of the micro channel plates generate secondary electrons which are multiplied in an avalanche like process. The electron clouds generated in this way illuminate the screen. Thus, the image appears in form of bright spots on the phosphorus screen as shown in Fig. 3–3. A few thousands of gas atoms per second must be ionized at the same site of a surface atom in order to produce an observable image on the phosphorus screen.

The interception of each crystallographic plane with the hemispherical cap of the tip surface has the form of a ring. The most prominent atoms on the surface, lying at these edge rings of the atomic layers, image brightly in the FIM. Thus, successive atomic terraces lying parallel to a particular crystallographic plane generate a family of concentric rings in the image as exemplified in Fig. 3–3 by a FIM image of a tungsten specimen taken at 5.0 kV in $5\cdot 10^{-3}\text{ Pa He}$ imaging gas and 70 K tip temperature.

The major crystallographic planes may be identified and their Miller indices assigned by determining the symmetry elements of the sets of rings in the image and their angular relationships. The main poles are also indexed in Fig. 3–3.

The FIM image corresponds approximately to a gnomonic projection of the tip surface with a magnification of $10^6 - 10^7$. The mean magnification at the tip apex might be calculated as:

$$M = \frac{L}{k \cdot R} \quad (3.2)$$

R is the specimen radius and L is the distance specimen to screen or in the case of APT the distance specimen to PSD detector. The factor $k \approx 1.6$ is empirically determined and takes into account the image deviation from the gnomonic projection.

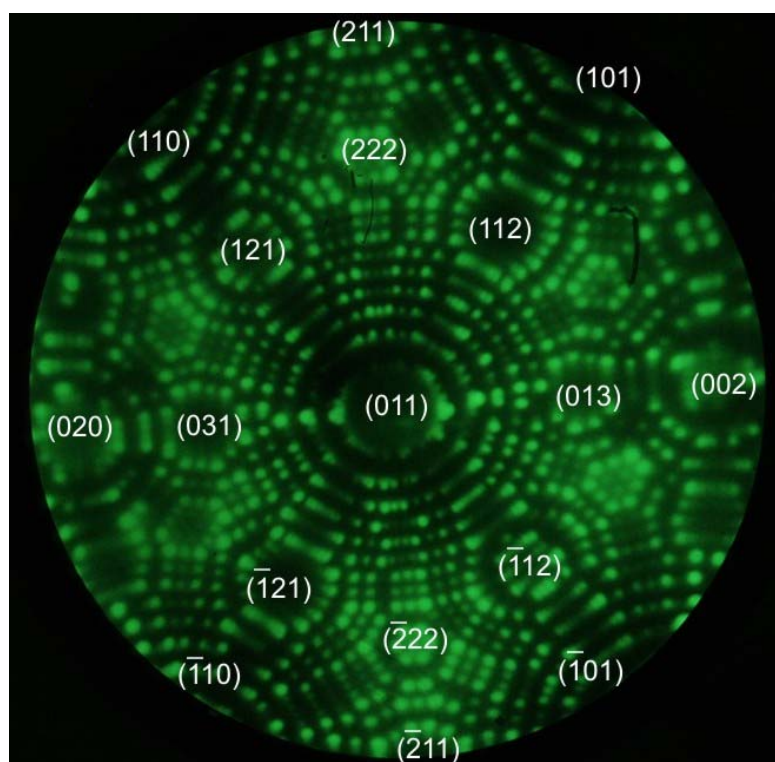


Fig. 3–3: Indexed FIM image of a tungsten tip specimen taken in $5 \cdot 10^{-3}$ Pa He imaging gas at 5.0 kV and 70 K tip temperature.

If the applied high voltage and by that the electric field strength is increased beyond the ionization strength of the imaging gas, then it is possible to remove atoms from the specimen's surface. The most prominent atoms on the surface, lying at the edges of the atomic layers, are the ones which are removed first (Fig. 3-2). This process is called field evaporation.

By removing atoms layer by layer from the specimen's surface, the tip curvature radius increases with increasing voltage. Simultaneously the magnitude of the magnification decreases. Hence, the FIM setup might be used to develop specimens to a desired geometrical shape. This is a very important property, since it allows to develop such specimens to a certain very smooth shape and use them further as substrates for thin film deposition with a very good reproducibility as presented in section 4.2. By that, thin film APT and FIM investigations are possible.

3.1.2 Atom Probe Tomography

In the TAP mode, the imaging gas leak is interrupted and the remaining imaging gas is pumped out of the chamber. The screen used for imaging the specimen's surface must be removed out of the optical axis, too Fig. 3–1 (pos 2).

If one superimposes high voltage pulses on the standing voltage U_0 applied in the FIM mode, single atoms may be field evaporated from the specimen's surface in a controlled manner. The high voltage pulse is $U_P = 15 - 25 \%$ of the standing voltage with a very short pulse length $t_P < 10 \text{ ns}$ and a pulse frequency of $500 - 2000 \text{ Hz}$. With each pulse a clock starts and it stops by the ion impingement onto the TAP detector. In this way, it is possible to chemically identify each collected ion by means of time-of-flight spectroscopy. Using the principle of energy conservation one can gain information on the mass of the atom by the energy balance:

$$\frac{m \cdot v^2}{2} = q \cdot U_{total} \quad (3.3)$$

$U_{total} = U_0 + U_P$ is the total voltage applied to the specimen, $v = L / t$ is the speed of the ion accelerated in the electric field and q is the ion charge. The final velocity is reached shortly after the ion has left the specimen's surface due to the strong localization of the electrical field at the tip apex and remains constant over the flight length as shown experimentally and by simulations [Miller 96],

[Nowak 04]. Introducing these parameters in (3.3) we obtain for the mass to charge ratio:

$$\frac{m}{q} = 2 \cdot (U_0 + U_p) \left(\frac{t}{L} \right)^2 \quad \text{or} \quad \frac{m}{n} = 2 e \cdot (U_0 + U_p) \left(\frac{t}{L} \right)^2 \quad (3.4)$$

with n being the ionization state.

By removing atoms layer by layer from the tip and collecting the ions at the detector, it is possible to perform a three dimensional analysis of the specimen. Using a position sensitive detector, the initial lateral position x and y of the atom at the momentary surface are determined. The PSD is build as an array of 10×10 anodes as sketched in Fig 3–1 (the right hand side). By the ion impingement upon the micro channel plates a relatively large electron cloud will be generated which irradiates in average 3 to 9 anodes of the detector. From the charge distribution over the anodes array one can determine the position of the centre of gravity of charge cloud (x_a, y_a) . The initial position of the atom inside the specimen is afterwards derived from the magnification M :

$$(x = \frac{x_a}{M}, y = \frac{y_a}{M}, z) \quad (3.5)$$

The progress in the depth coordinate z is calculated from the number of field–evaporated atomic layers, i.e. from the number of detected ions N and the volume V_{at} of the evaporated atoms:

$$dz = \frac{V_{at} \cdot dN}{S_D \cdot a^2} \quad (3.6)$$

with $S_D \sim 0.5$ being the detector efficiency and a^2 the detector surface.

In addition, the curvature of the tip surface needs to be taken into account (see Fig. 3–4) and the depth z is refined as [Bas 95]:

$$z = z_0 + z' \quad (3.7)$$

with

$$z' = R - \sqrt{R^2 - (x^2 + y^2)} = R \left(1 - \sqrt{1 - \frac{x_a^2 + y_a^2}{R^2 \cdot M^2}} \right) \quad (3.8)$$

where R is the momentary tip radius.

The application of this reconstruction scheme frequently yields atomic resolution for the z direction (see Fig 3–5.). The lateral resolution is limited to 3 – 5 Å due to imprecision of the back projection to the tip surface.

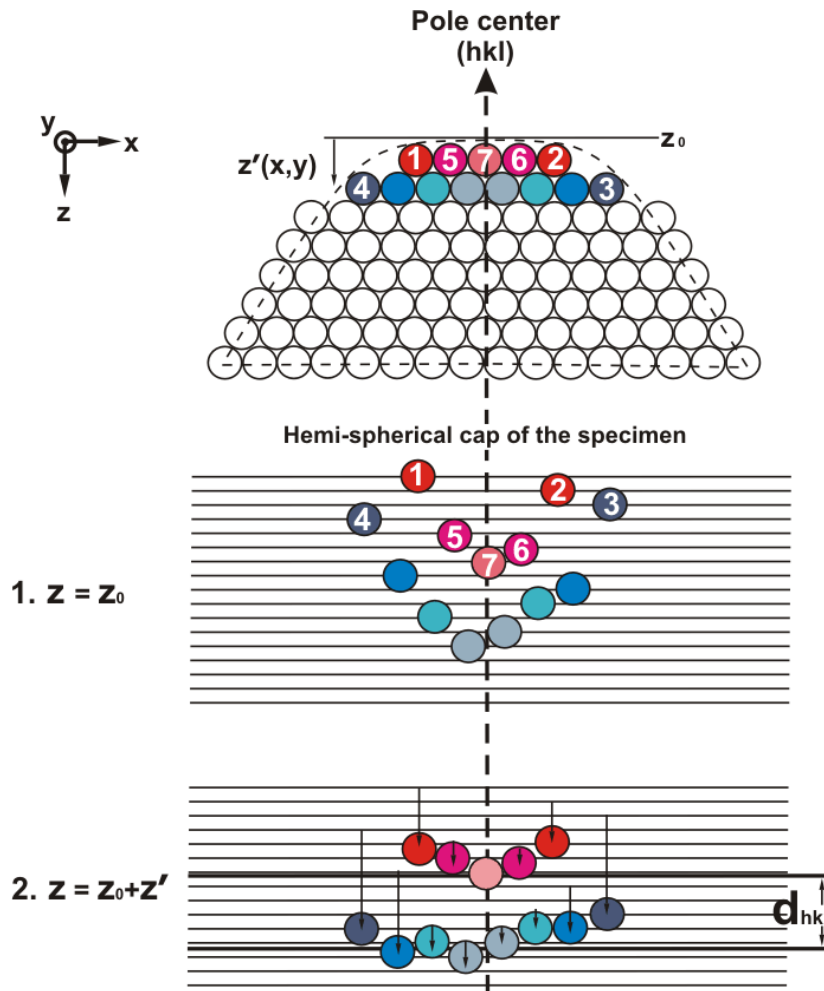


Fig. 3–4: The depth scaling of the TAP measurements. The numbers present the probable field evaporation sequence of the surface atoms. By taking into account the tip curvature for depth correction in the second step, inter-atomic distances might be resolved.

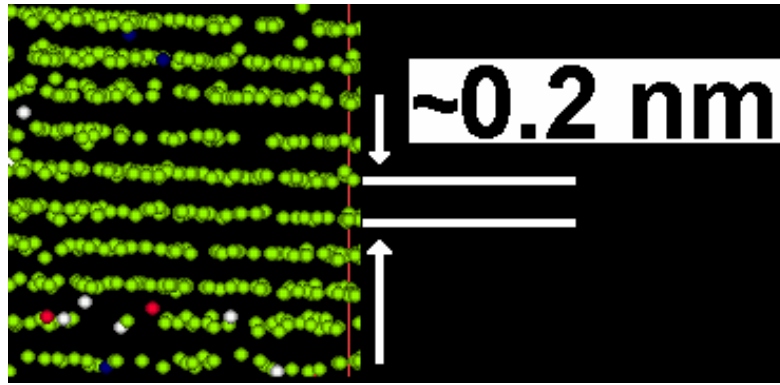


Fig. 3–5: Example of the depth scaling in a reconstructed Cu layer showing clearly resolved Cu {111} planes. Cu atoms are represented by green spheres. There is no relation between the spheres and the atom size. The size of spheres was chosen for optimum presentation.

3.1.3 Parameters used for APT analysis

The operation of the TAP instrument requires the adjustment of several specific parameters like pulse rate, pulse fraction and specimen temperature for each type of investigated material. For a statistically significant analysis a minimum of $5 \cdot 10^5$ collected atoms for bulk materials and $1 \cdot 10^6$ atoms for multilayered structures are necessary. The choice of appropriate measurement parameters is done in order to prevent a specimen failure under the mechanical stress induced by the applied high electric field, which reaches up to 10^{10} Pa. The simplest solution to avoid specimen fracture would be the choice of a relatively high specimen temperature (70 K or more) and a lower U_p/U_0 pulse fraction (~ 0.15). But for some multicomponent systems this may lead to uncontrolled field evaporation of components with a low evaporation field strength. As a consequence, the concentration would be underestimated for these components. By choosing lower temperatures (15 – 25 K) and higher pulse fractions (~ 0.25) one is able to avoid this uncontrolled field evaporation even in the case of multilayers like Al/Cu which have a relatively large difference in evaporation field strength, however with some costs on the yield of successful measurements.

The TAP parameters used for the measurements in this work are summarized in Table 3.1:

Table 3.1.

Parameter	<i>Cu/NiFe</i>	<i>Al/Cu</i>
Tip temperature [K]	25 – 60	15 – 25
Pressure [Pa]	$\sim 5 \times 10^{-8}$	$\sim 5 \times 10^{-8}$
Pulse ratio [%]	25	15 – 25

3.2 Data analysis

The data acquired by the TAP measurement representing the information about the flight time and electrical charge registered by the detector's anodes for each incoming ion must be further processed in order to obtain the desired chemical identification and three-dimensional visualization of the measured volume. For that, dedicated evaluation software based on AVS package was used. The reconstruction principle and some of the analysis tools are briefly presented in the following sections.

3.2.1 Layered structure's reconstruction

The use of equation (3.1) allows the calculation of the curvature radius of the tip-like specimen as a function of the applied voltage U , evaporation field strength E and the geometrical factor β . For this, the product βE is assumed

constant during the entire measurement. This was found as a good approximation which yields reliable reconstructions for small precipitates embedded into a matrix [Blavette 98]. Nevertheless, in the case of thin films the evaporation field strength varies from one layer to the other and the reconstruction may reveal severely distorted volumes [Jeske 01]. Fig. 3–6(a) presents such an example for the case of one of the systems investigated in this work—*Al/Cu* multilayer deposited on *W* substrate.

Therefore, for the thin film reconstruction problem a different reconstruction algorithm was developed [Schmitz 01]. This algorithm is based on geometrical considerations and assumes a constant specimen shaft angle γ . Thus, the tip radius is easily estimated from the geometrical relation resulting straight forward from Fig 3–7:

$$\frac{dR}{dz} = \frac{\sin \gamma}{1 - \sin \gamma} \quad (3.9)$$

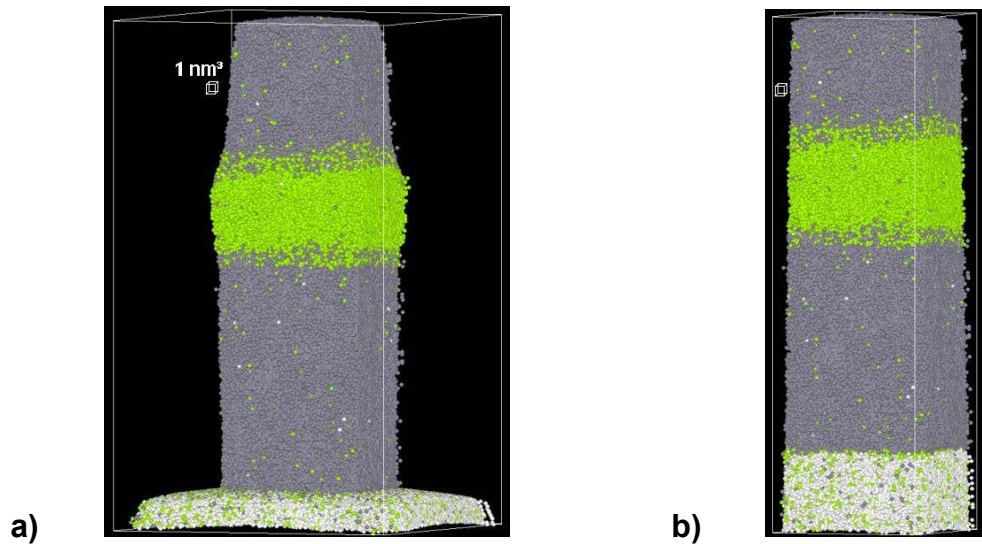


Fig. 3–6: Reconstruction of an Al/Cu/Al trilayer (Al–gray spheres, Cu– green spheres) deposited on W (white spheres) substrate. (a) Severely distorted interfaces in reconstruction based on Eq. (3.1). (b) Correct reconstruction based on Eq. (3.9)

In order to apply this algorithm, the initial radius and the shank angle must be known. Using electron microscopy, these parameters can be directly measured from the micrographs. There is also the possibility to choose them as free parameters at the beginning of the reconstruction and to vary them later on, until the evaporation fields known from calibration measurements are reproduced (Fig. 3–8).

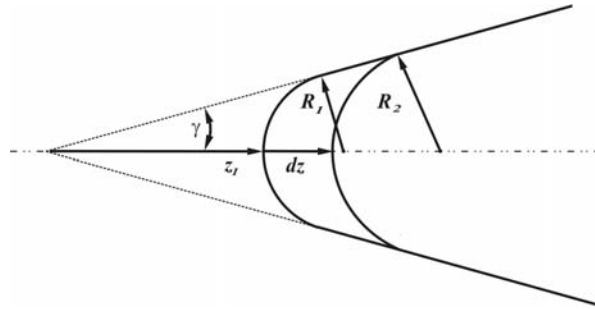


Fig. 3–7: Geometrical model for the tip radius evolution with a constant shaft angle γ .

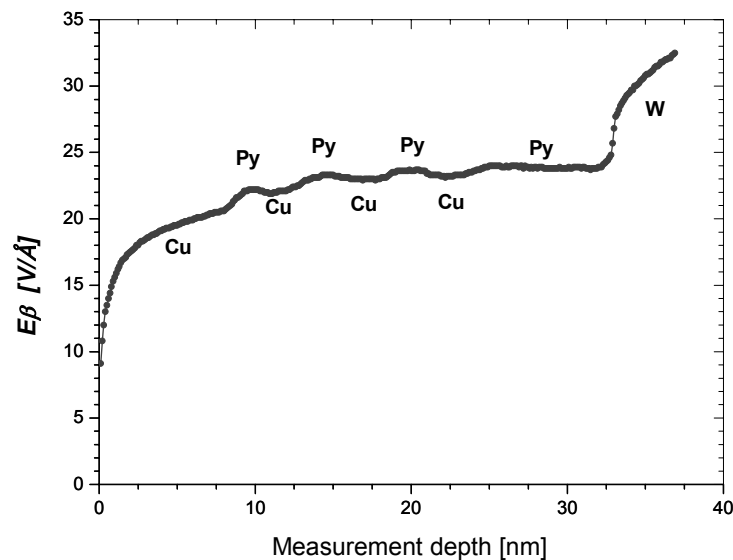


Fig. 3–8: Evaporation field curve ($\beta \approx 7$) for a multilayer stack copper/permalloy deposited on tungsten (Py = Permalloy = $\text{Ni}_{79}\text{Fe}_{21}$).

3.2.2 One-dimensional concentration profiles

The reconstructed measurement itself offers only a three-dimensional visual image of the investigated volume of the specimen. For a quantitative data interpretation in terms of e.g. concentration gradients, a 1-d composition profile is a very suitable tool. For that, a cut-out volume along the desired direction is divided in smaller volumes (slices) and the concentration is determined for each of these sub-volumes. The values obtained in this way are plotted against the depth. Typically, a cylindrical volume, often called the analysis cylinder, of a few nanometers radius is chosen.

In order to get relevant statistics, every small volume has to contain a sufficient number of atoms to be analyzed and hence a minimum size. Since the average number of atoms N included in the slice is proportional to its volume, the choice of too small volumes leads to an increase of the statistical error σ of the determined concentration:

$$\sigma = \sqrt{\frac{c(1-c)}{N-1}} \quad (3.10)$$

As known from the binomial distribution, about 96 % of the values of the distribution are included in the variance (2σ) interval, which means that only outside this interval concentration variations might be interpreted as real and not as statistical fluctuation. For example, a disk-shaped slice of 3 nm radius and 0.3 nm thickness in Cu/Al contains around 300 detected atoms. If the mean composition is 50 at%, then the 2σ interval is approximately 44 at% to 56 at%. For 99 at% composition, the 2σ interval is approximately 98 at% to 100 at%.

In this work the typical radius of the analysis cylinder is 3nm and is oriented with its axis normal to the interfaces between the deposited layers (Fig. 3–9 a). Local compositions are derived by a moving average along the cylinder axis. For that, the cylinder is subdivided into overlapping, disk-shaped slices with a typical thickness of 0.3 nm spaced by 0.1 nm.

3.2.3 Two-dimensional composition maps

From the three-dimensional reconstructed volume it is also relatively easy to derive two-dimensional composition maps. A plane mesh is positioned inside the analyzed volume. At each point of the mesh the local concentration is determined inside a small cube and afterwards a colour is attributed to each concentration value (Fig. 3–9 b). This way, the colour distribution reflects the concentration distribution. Again the cube volume has to be chosen in such a way that enough atoms are contained ($N \geq 100$), but on the other hand, the volume must be smaller than the features which are intended to be resolved. In the present work a cube with 1.7 nm edge length and a grid spacing of the mesh of 0.5 nm were used.

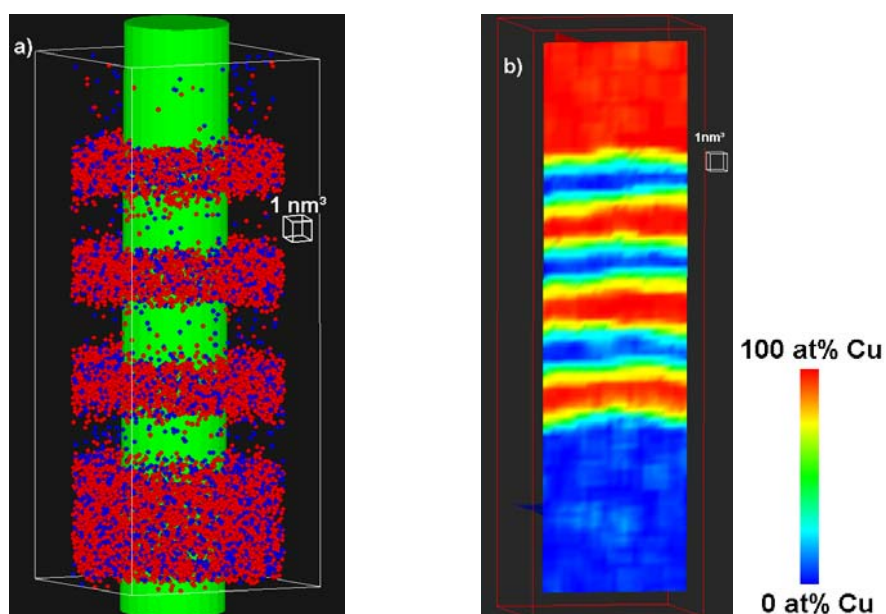


Fig. 3–9: Analysis methods: a) cylinder positioned perpendicularly to the local multilayer interfaces used for a one dimensional composition profile analysis in an as-prepared Cu/Py multilayer (red spheres Ni, blue spheres Fe, Cu atoms are hidden); b) two dimensional composition map of Cu in an as-prepared Cu/Py multilayer.

3.3 *Complementary investigation methods*

Obviously the quantitative investigations on atomic scale with small concentrations make necessary the complementary use of several analysis methods. Thus, besides the atom probe tomography other analysis methods were used to investigate the thin films samples under consideration.

Transmission Electron Microscopy (TEM) was used for investigation of both FIM tips and planar deposited multilayers. For the examination of the geometry of FIM/TAP specimens an instrument type “Philips CM 12” was used. High resolution pictures of the thin films deposited on planar substrates were taken at the Institute of Material Physics at the University of Münster with an instrument type Zeiss Libra, equipped with a field emitter and operated with an acceleration voltage of 200 kV.

The macroscopic interreaction in *Al/Cu* system was investigated by Scanning Electron Microscopy (SEM) and Energy Dispersive X-ray Microanalysis (EDX). The SEM used was a Leo SupraTM 25 equipped with a Noran System Six EDX.

4 Sample preparation

The preparation of thin films samples requires particular effort and time. Besides the film deposition, the most difficult tasks are the preparation of the tip-shaped substrates and the TEM and FIM sample preparation from thin films deposited onto planar substrates. This chapter presents all the preparation techniques and the parameters used.

4.1 *Substrates preparation*

4.1.1 FIM/TAP sample preparation

As presented in the previous chapter, the samples for FIM/TAP investigation are very sharp needles. Only a few techniques may be applied to position the interfaces of interest into a needle shaped tip of a radius of curvature below 50 nm.

The first one, and the most suitable method due to its throughput, is the deposition onto pre-shaped tips. Tungsten (W) is chosen as a substrate material because of its ideal properties for field ion microscopy and, furthermore, because of its high melting point, which prevents reactions with the investigated materials. For that, 0.1 mm wire is cut to an approximate length of 1.5 cm and crimped in a copper tube. Afterwards, the wire is inserted into 2 mol NaOH solution. Using a platinum electrode and 2 – 4 V, 3Hz, AC voltage with the shape of a sine wave the wire is electropolished to a very small tip radius of 20 – 50 nm. The sine shaped AC voltage allows a very good reproducibility of

the substrates preparation by formation of a neck-like zone near the air–electrolyte interface as sketched in Fig. 4–1.

Using a conventional field ion microscope, tungsten substrates obtained by electropolishing were field evaporated up to 14 kV in order to obtain a smooth surface and a suitable reproducible radius of curvature. After the field development, these substrates were coated by ion beam sputtering (IBS – see section 4.2) with the thin films to be investigated and finally measured in the as sputtered state or after appropriate thermal treatments (section 4.4).

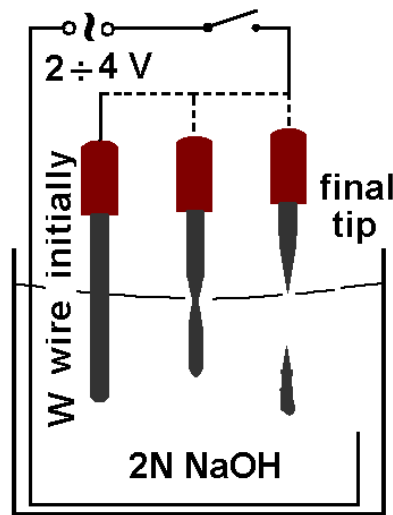


Fig. 4–1: Schematic illustration of the electropolishing process.

4.1.2 Planar samples

In order to compare the results obtained on curved substrates, thin films were deposited also onto planar *Si*, *Cu* and *W* substrates. The *Si* substrate was (100) oriented highly n–doped (Arsenic) with $0.01 - 0.02 \Omega\text{cm}$ resistivity. The idea behind the highly doped *Si* was to use the same planar *Si* as for the most electronic devices. Since this is conductive, it might be investigated after appropriate preparation also by FIM/TAP. For the *W* and *Cu* planar substrates $10 \times 10 \times 0.7 \text{ mm}$ plates were cut by spark erosion and mechanically polished to

less than $0.3\ \mu\text{m}$ roughness before deposition. TEM and FIM specimens were prepared out of these planar samples by means of a focussed ion beam (FIB) in a rather elaborate process which is described in section 4.3.

4.2 Deposition process

The investigated thin films were deposited by ion beam sputtering on *Si* and metallic substrates prepared as described in the previous sections. The ion beam sputtering is a physical vapour deposition process in which a current of energetic ions generates a flux of target atoms that can be used to coat the substrates situated in front of the target. The remaining adsorbate atoms and eventually oxides on substrates and targets surfaces are removed directly before deposition by *Ar* ion etching. This is required in order to obtain chemically clean interfaces and improved mechanical stability of the APT specimens. The IBS setup (Fig. 4–2) used for the sample preparation in the present work was constructed by Schleiwies [Schleiwies 01].

In practice, the specimens are obtained in three steps: in a first step, substrates are protected with a shutter and rotated out of the beam, while the targets are cleaned (each target is positioned in front of the beam by rotating the multiple targets holder), in the second step, the substrates are positioned in front of the beam to be cleaned (pos 1 Fig. 4–2) and in the final step, the substrate holder is rotated to position 2 in Fig. 4–2 and the deposition sequence is performed. The deposition of chemically different layers is possible by a multiple targets holder (up to 4 different targets) which allows switching between different materials within less than one second. Since the deposition rates are usually in the $2\text{--}5\ \text{nm/min}$ range, nearly atomically sharp interfaces are obtained. The deposition was carried out at room temperature using a base pressure $\leq 5 \times 10^{-6}\ \text{Pa}$. The most important parameters of the sputtering process are presented in table 4.1.

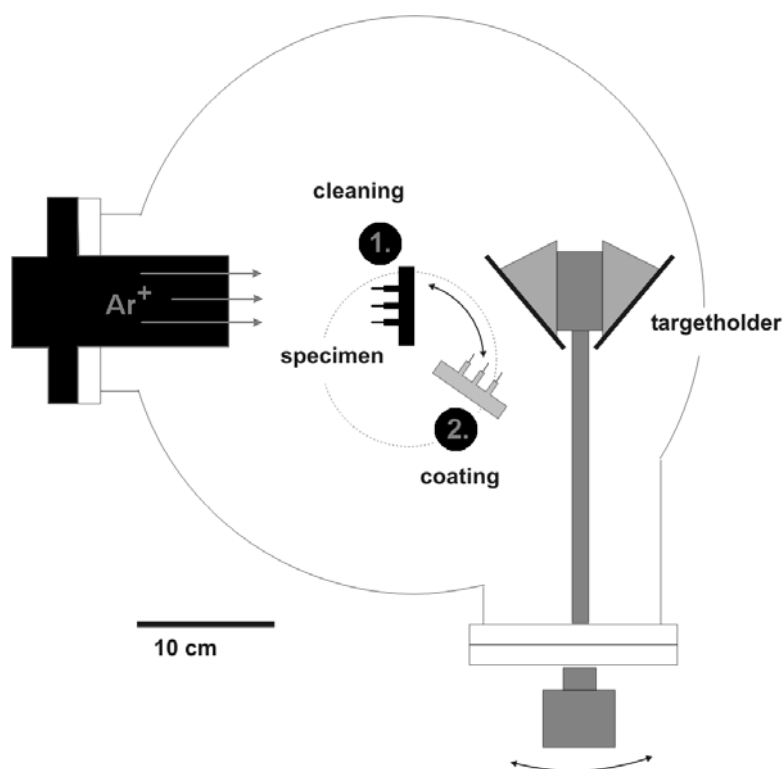


Fig. 4–2: Schematic illustration of the sputter deposition device (Schmitz, 2001). Switching between tip cleaning (1) and coating (2) is achieved by a simple rotation of the specimen stage.

Table 4.1. Parameters of the sputtering process.

Procedure	Current density [mA]	Beam-voltage [V]	Ar-pressure [Pa]	Time [s]
Target cleaning	25	600	1.5×10^{-2}	120 (each)
Substrate cleaning	10	500	10^{-2}	15

Procedure	Current density [mA]	Beam-voltage [V]	Ar-pressure [Pa]	Time [s]
Deposition of <i>Cu</i> / <i>Py</i> multilayers.				
<i>Cu</i>	12	550	10^{-2}	20
<i>Py</i> ($Ni_{79}Fe_{21}$)	12	550	10^{-2}	45
Deposition of <i>Al</i> / <i>Cu</i> multilayers.				
<i>Al</i>	12	550	10^{-2}	300–360
<i>Cu</i>	12	550	10^{-2}	100–120

4.3 Focused Ion Beam TEM and FIM/TAP sample preparation

The Focused Ion Beam (FIB) system uses a sharply focused beam of gallium ions to raster over the surface of a sample similarly to the electron beam in a scanning electron microscope. This can be operated at low beam currents for imaging or at high beam currents for site specific sputtering or milling. The generated secondary electrons (or ions) are collected and form a high resolution image of the sample's surface. The ion beam allows the milling of small holes in the sample at well localized sites, so that cross-sectional images of the structure can be obtained or modifications in the structures can be made. The possibility to obtain cross-sectional images is a very important tool for failure analysis in semiconductor industry. Site specific milling might be also used to prepare TEM and even APT specimens [Giannuzzi 98, Thompson 04, and Miller 04].

A Dual Beam Focused Ion Beam/ Scanning Electron Microscope type FEI NovaTM 600 Nanolab was used for the TEM and APT specimen preparation from thin films samples deposited onto planar substrates. The Fig. 4–3 presents schematically the configuration of the instrument.

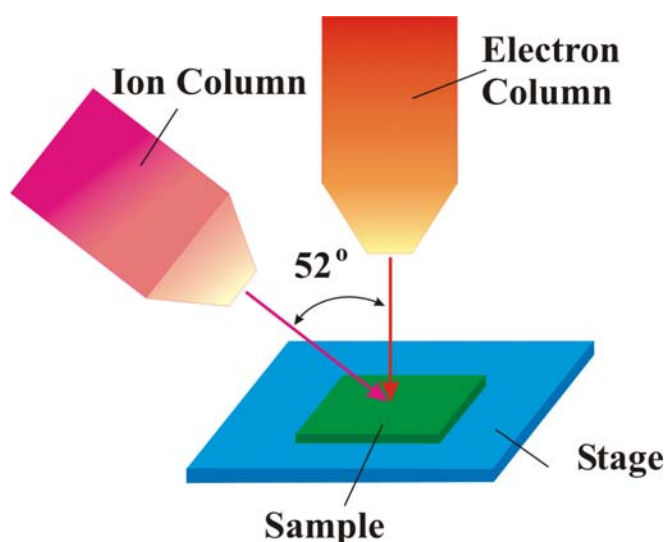


Fig. 4–3: Schematic illustration of the Dual Beam Focused Ion Beam / Scanning Electron Microscope.

The most important technical characteristics are presented in table 4.2:

Table 4.2. Technical characteristics of FEI NovaTM 600 Nanolab FIB/SEM.

	Accelerating voltage	Probe current	Resolution
FIB	5 – 30 kV	1 pA – 20 nA	7 nm
SEM	0.2 – 30 kV	≤ 20 nA	1.1 nm (15 kV)

4.3.1 TEM sample preparation

TEM samples manufactured by the FIB lift-out technique provide a faster way to obtain thin electron transparent foils compared to the conventional cross-section specimen preparation technique. The specimens are milled out from a relative large sample ($10 \times 10 \text{ mm}$ *Si* wafer for the present work).

In the first step, after choosing the appropriate location by STM observation, a thin ($\sim 200 \text{ nm}$) *Pt* protective film is deposited by decomposition of a gaseous organometallic compound due to the interaction with the electron beam. This layer is further increased to $\sim 2 \text{ }\mu\text{m}$ by ion beam – gas interaction (higher deposition rate). Volatile organic impurities which are released, are removed by the vacuum system, leaving behind the desired metal deposited on the surface of the sample. Afterwards, using a large beam current for fast ion milling, two trenches are milled on either side of interest, and then the area in the middle is almost cut free by the FIB. Before finishing the cut, the lamella is *Pt* welded on the sharp needle probe of a micromanipulator (Omni probe). Afterwards, the lamella is cut free, the Omni probe is retracted and the lamella is welded on a *Cu* holder suitable for the TEM analysis. Subsequently, the Omni probe is separated from the sample by FIB cutting. On the *Cu* holder using smaller beam currents in steps, the membrane is thinned and polished to a thickness between 150 and 50 nm which enable electron transparency for most materials. The different steps in TEM sample preparation are presented in Fig. 4–4.

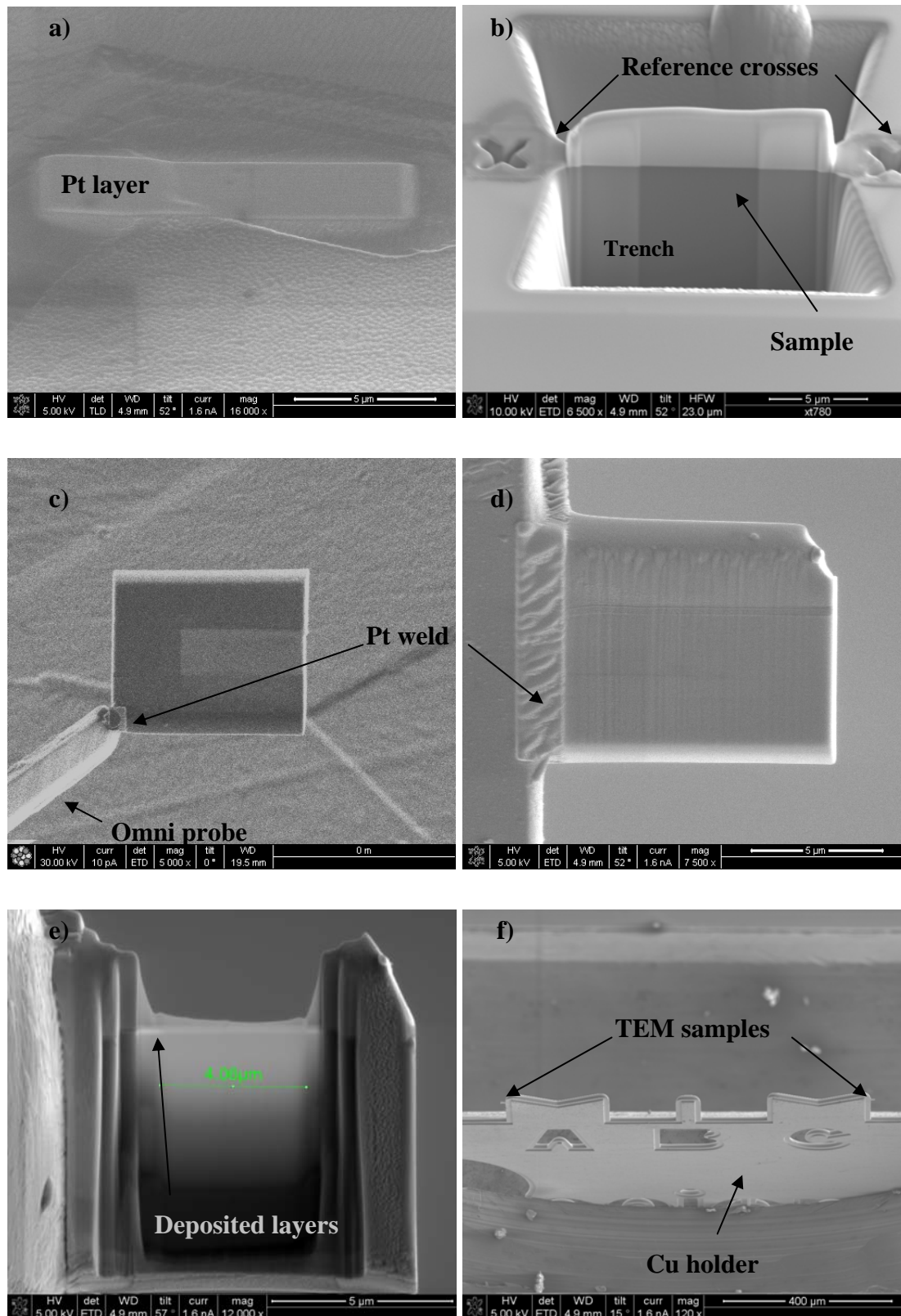


Fig. 4-4: Steps in TEM sample preparation: a) Pt protective layer deposited on top of the interesting area; b) Trenches milling; c) Lifted-out lamellae to be welded on the TEM holder; d) Welded lamellae on the Cu holder; e) Thinning to transparency; f) View of the Cu holder with two TEM samples as indicated by arrows.

4.3.2 APT/FIM sample preparation

Compared with the TEM sample preparation, the FIM sample preparation is even more complex due to the smaller dimension which has to be reached (~ 50 nm tip radius). The same lift-out method is used as in the case of TEM samples but in this case the *Cu* holder is replaced by a *W* tip suitable for APT/FIM measurements. The most important steps in FIM sample manufacture are presented in Fig. 4–5.

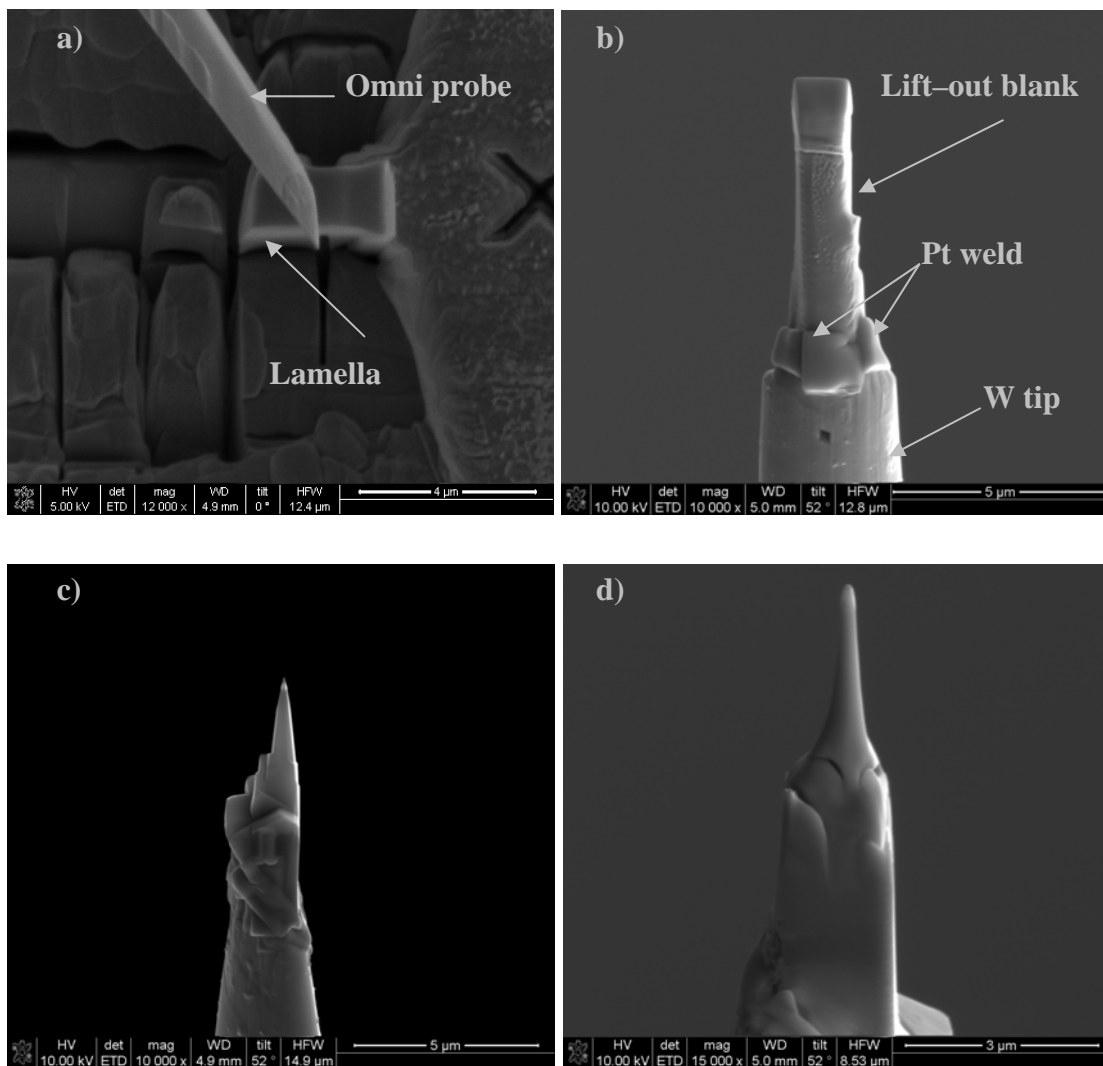


Fig. 4–5: Different steps in APT/FIM sample preparation: a) Lift-out of a 2×2×5 μm post from a lamella similar to the TEM sample; b) Welding on the W tip; c) Side milling to reduce the samples dimensions; d) Final polish by annular milling.

4.4 Thermal treatments

Both systems, *Cu/Py* and *Al/Cu* were investigated in as-prepared and thermally treated states. The thermal treatments of the APT samples were done under vacuum with a base pressure of $\leq 10^{-6}$ Pa. The oven consists of a vacuum recipient with a *Cu* plate in which the specimen holder can be screwed. The specimen holder is manufactured from a *Cu* alloy to assure a good heat transfer from the *Cu* plate to the specimen. For optimal control of temperature and annealing time, the plate was first heated to the chosen temperature and afterwards the specimen holder was screwed into the *Cu* plate.

The heat is provided by two 150 W halogen lamps, which heat the *Cu* plate through a quartz glass window. Since the heat source is outside the recipient, it is possible to have a stable vacuum $\leq 10^{-6}$ Pa during the thermal treatments. The annealing time and annealing temperatures are shown in Table 4.3.

Table 4.3.

System	Annealing time [min]	Annealing temperature [°C]
<i>Cu/Py</i>	20 – 80	150 – 500
<i>Al/Cu</i>	5 – 80	80 – 200

The thin films deposited on planar substrates were annealed directly after deposition in the sputter chamber using a ceramic heating element attached to the sample holder. The temperature was measured using the same type of thermo-element as for the halogen oven placed in contact with the substrate's surface on which the film was deposited.

5 Investigation of Copper/Permalloy GMR multilayer structures

This chapter introduces briefly the Giant Magneto–Resistance (GMR) effect [Baibich 88, Binash 89], points out the state of the art of research and presents the experimental results obtained by APT/FIM measurements during the present work. The results are discussed afterwards and compared with results obtained by different investigation techniques as reported in the literature.

5.1 *Giant Magneto–Resistance*

One of the most important and fascinating discoveries in the last two decades in solid state physics is that of the giant magneto-resistance effect [Baibich 88, Binash 89]. For their finding Peter Grünberg and Albert Fert have been honoured with the highest distinction of the scientific world, the Nobel Prize.

The oscillatory ferromagnetic coupling between ferromagnetic layers separated by non-magnetic spacer layers [Allenspach 98] attracts a remarkable scientific interest because of its application of magnetic data storage and sensoric. This kind of coupling mechanism has been observed in a large number of ferromagnetic layers and many spacer layers including noble metals [Bennett 90] and non-ferromagnetic transition metals [Parkin 91]. The coupling energy between two or more ferromagnetic layers oscillates, changing from ferromagnetic coupling, in which case the magnetization is parallel, to antiferromagnetic coupling with an anti-parallel magnetization, depending on the thickness of the spacer layers.

The conduction electrons are delocalized in metallic systems and are able to carry magnetic spins through non-ferromagnetic metallic spacer layers. That means, the conduction electrons mediate the coupling as described by the RKKY (Ruderman–Kittel–Kasuya–Yosida) interaction [Ruderman 54]. Studies of this phenomenon led to the discovery of Giant Magneto–Resistance (GMR). In some transport experiments on anti-ferromagnetically coupled Fe/Cr multilayers, Grünberg and Fert found negative magneto–resistance i.e., the electrical resistance decreases as the applied magnetic field is increased, with the change in resistance being a few orders of magnitude higher than the change in case of Anisotropic Magneto–Resistance (AMR) [Baibich 88, Binash 89]. A recent review article from Tsymbal and Pettifor presents the actual state of understanding of the physics beyond the GMR effect and points out the tremendous technological progress made within only a decade after the discovery of GMR effect [Tsymbal 01].

The sketch in Fig. 5–1 illustrates the change in resistance of a trilayer as a function of the applied magnetic field, and the trilayer’s magnetization configurations (indicated by the arrows) at various magnetic fields. The magnetizations are aligned anti-parallel at zero field and parallel when the external magnetic field H is larger than the saturation field H_S .

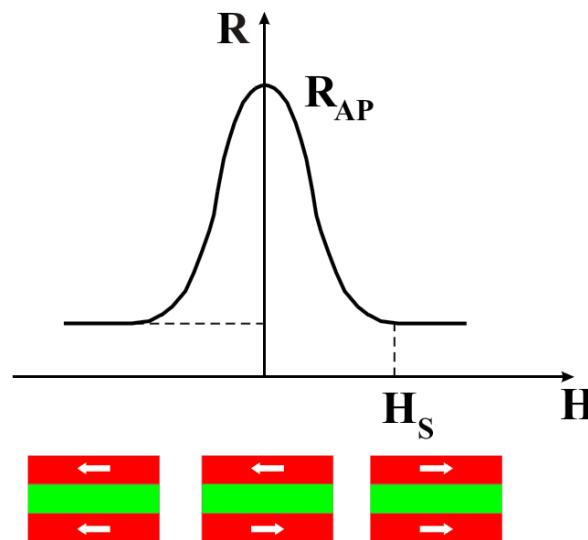


Fig. 5–1: Schematic representation of the change in resistance of a trilayer. The magnetization of the layers is aligned parallel for H larger than H_S and anti-parallel at zero-field as indicated by arrows.

The GMR effect can be explained in terms of bulk or interface scattering as the mean free paths (MFP) of minority spin and majority spin carriers are different. The conducting electrons are scattered by successive ferromagnetic layers. Let us consider two or more ferromagnetic layers with magnetizations either parallel or anti-parallel to each other, separated by non-magnetic or noble metallic layers. If the mean free path of the conducting electron is much greater than the thickness d of the single layers ($\text{MFP} \gg d$) and the conduction is modelled in terms of two largely independent conducting channels as proposed by Mott [Mott 36, 64], corresponding to spin-up and spin-down electrons, one can imagine situations in which one channel is less scattered than the other or both channels are equally scattered. The first situation occurs for the case that all the magnetizations are parallel to each other. For the ferromagnetic coupled multilayer (Fig. 5-2 a), the spin-up electrons pass through the structure almost without scattering, whereas the spin-down electrons are scattered strongly within both ferromagnetic layers. Since conduction occurs in parallel for the two spin channels, the total resistivity of the multilayer is low. In the second case, for the antiparallel-aligned multilayer (Fig. 5-2 b), both the spin-up and spin-down electrons are scattered strongly within one of the ferromagnetic layers, and the total resistivity of the multilayer is high. Each of the two cases is illustrated in the lower row of Fig. 5-2 by a parallel resistor network. In the resistor model each ferromagnetic layer is treated as an independent resistor. Within each spin conduction channel the resistors are added in parallel or in series depending on the relationship between the MFP and the layer thickness. If the MFP is short compared to the layer thickness, then each layer conducts the electric current independently and the resistors have to be added in parallel. Obviously in this case, the electrical resistances of the parallel and anti-parallel configurations are exactly the same leading to GMR zero. In order to obtain a non-zero GMR the mean free path must be sufficiently long compared to the layer thickness ($\text{MFP} \gg d$). In this case, for the two configurations in Fig. 5-2 we can calculate the electrical resistance (the interface resistance is neglected for simplicity) as follows:

$$R_p = \frac{2 \cdot R_{\uparrow} \cdot R_{\downarrow}}{R_{\uparrow} + R_{\downarrow}} \quad (5.1)$$

$$R_{AP} = \frac{R_{\uparrow} + R_{\downarrow}}{2} \quad (5.2)$$

with R_p and R_{AP} the total resistance of the parallel and anti-parallel multilayer alignments, respectively. Thus, the magneto-resistance ratio is determined by the expression

$$\frac{\Delta R}{R} = \frac{R_{AP} - R_p}{R_p} = \frac{(R_{\downarrow} - R_{\uparrow})^2}{4R_{\downarrow} \cdot R_{\uparrow}} \quad (5.3)$$

In this definition the GMR is normalized to the low resistance R_p [Tsymbal 01]. Although within this definition the GMR can be larger than 100%, it is used in most papers devoted to GMR.

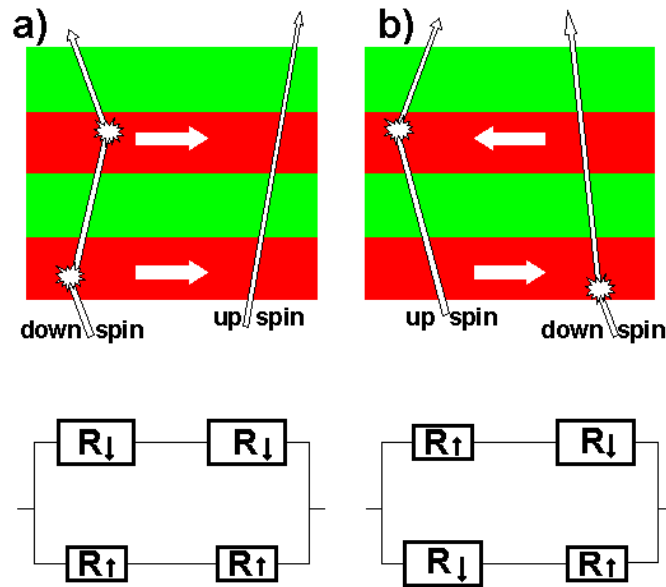


Fig. 5–2: Schematic representation of the electron transport in a multilayer: parallel magnetization (a) and anti-parallel magnetization (b) of successive ferromagnetic layers, as indicated by arrows. In the bottom row, resistor networks are drawn for each magnetization configuration.

5.2 State of the art of GMR effect investigations

During the last ten years, application of the Giant Magneto–Resistance effect in technical devices enabled a dramatic increase in magnetic recording density and the development of new safety features in automotive industry. More than a decade after the discovery of the effect in *Fe/Cr* thin film multilayers [Baibich 88, Binash 89], magnetic multilayers still attract a remarkable amount of scientific interest because of their already proved utility in data storage and magnetic sensor technique. *Cu/Co* and *Cu/Py* ($Ni_{79}Fe_{21}$ = Permalloy = *Py*) are two of the most often used systems. *Cu/Co* presents higher GMR amplitudes, but a pronounced hysteresis reduces the sensitivity and introduces some ambiguity in the signal of positional or orientational sensors. For the latter application, *Cu/Py* multilayers are promising candidates because of their higher sensitivity and lower hysteresis. However, for many potential applications, as e.g., angular sensors in motor vehicles, the thermal stability of the device is an important issue. It is known that the *Cu/Py* system is much more sensitive to thermal load than *Cu/Co*. Heat treatments at a temperature of 150 °C already modify the GMR amplitude of *Cu/Py* multilayers and above 250 °C the GMR amplitude disappears almost completely [van Loven 00, Heitmann 00, Hecker 02]. In contrast to *Cu/Py* layers, the GMR amplitude of *Cu/Co* systems remains unchanged up to 400 °C [Hecker 02].

Different explanations for the mechanisms, which are responsible for the GMR degradation, have been proposed: van Loven et al. [van Loven 00] argue that at least two different mechanisms contribute to the breakdown of *Cu*–based GMR multilayers (*Cu/Co* and *Cu/Py*), namely grain boundary diffusion and inter– or de–mixing at the interface. Grain boundary diffusion of *Ni* in *Cu* was found also by Schleiwies et al. [Schleiwies 01] in a *Co/Cu/Py* triple layer using local chemical analysis. Since the thickness of these layers is a few nanometers only, their investigation with conventional techniques is rather difficult or even impossible. Brückner et al. [Brückner00] performed a complex investigation on a *Py_{100 nm}/Cu_{200 nm}/Py_{100 nm}* model tri–layer, including resistance measurements,

Auger electron spectroscopy, X-ray diffraction and laser-optical stress measurements, and they conclude that interdiffusion over only short distances dominate the degradation of the GMR amplitude in *Cu/NiFe* multilayers at moderate temperatures. For Hecker and co-workers [Hecker 02] the alloying tendency of *Ni* and *Cu* above 250 °C determines the decay of the GMR and the change in the magnetic properties of the *Cu/Py* multilayers. They investigated the effect of annealing on a *Cu/Py* multilayer by X-ray diffraction, electron microscopy and transport properties measurements, magneto-optical Kerr effect and ferromagnetic resonance.

5.3 Motivation of the study

The remarkable difference between the thermal stability of *Co* and *Py* – based systems seems to be due to the different thermodynamics of the respective phase diagrams. While *Cu* and *Co* are nearly immiscible, *Cu* and *Ni* form a continuous range of solid solutions with a solubility gap determined rather poorly at low temperatures. Thus, the latter system is already unstable in terms of bulk thermodynamics, whereas the first one may be only destabilized by interfacial contributions.

There is a major interest in the reaction mechanisms. In particular, several questions need to be answered such as: i) which elements are the mobile ones; ii) at which point (temperature, annealing time) is the structure of dense layers destroyed; iii) what is the role of structural defects like grain boundaries or interfacial roughness?

In view of the small periodicity of the multilayers restricted by the RKKY coupling [Ruderman 54] to the range of 2 – 4 nm, state of the art analysis methods of highest spatial resolution are required.

A further complicating factor, which motivates the interest to investigate such a system in detail, arises if the clear layer structure is disturbed in later stages of the reaction. In this case, three-dimensional information is needed to understand phenomena like the transport along the grain boundaries or the formation of local layer breakthroughs. Therefore, in this work atom probe tomography (APT) is applied; a technique which allows a three-dimensional reconstruction of the spatial distribution of the various atomic species with single atom sensitivity and a spatial resolution in the range of $1.5 - 3 \text{ \AA}$ slightly depending on the analysis direction.

The APT technique has been used successfully over the last few years to study magnetic multilayers. Investigations were conducted by Larson et al. [Larson 00, Larson 04] or Schleiwies et al. [Schleiwies 01] on different systems exhibiting GMR. In a $(\text{Ni}_{82}\text{Fe}_{18}/\text{Co}_{90}\text{Fe}_{10}/\text{Cu}/\text{Co}_{90}\text{Fe}_{10}) \times 10/\text{Ni}_{82}\text{Fe}_{18}$ grown on *Si*, they found that there is an enrichment of Fe at the interface where *Cu* is grown on *CoFe* and a depletion of Fe where *CoFe* is grown on *Cu* [Larson 00]. Investigating $\text{Cu}_{2 \text{ nm}}/\text{Co}_{2 \text{ nm}}$ annealed at $360 \text{ }^\circ\text{C}$ for 1 h , they found an increase in grain size, but no apparent change in the interfacial mixing between *Cu* and *Co*. They studied also *CoFe/Cu* films deposited in the presence of oxygen and observed that the GMR of these specimens becomes more sensitive to heat treatment compared to layers produced in a clean vacuum atmosphere. No detailed physical mechanism could be postulated for this effect yet, which may be partly due to the fact that they studied only very few specimens owing to their fascinating but complicated preparation method [Larson 04].

Concerning the *Cu/Py* system, no APT results were reported in the literature. This motivates the start of this work which is the first complete APT investigation over a large temperature range aiming to identify the mechanism of the already reported temperature induced GMR signal degradation.

5.4 Experimental results in Cu/Py multilayers

The $Py_{5nm}/(Cu_{2nm}/Py_{2nm})_{3-5}/Cu_{7nm-10nm}$ stacking sequence was deposited on tungsten pre-shaped tips by ion beam sputtering using the conditions indicated in Table 4.1. In the following, the experimental results obtained in as-prepared state and after different thermal treatments are presented and discussed. To determine the effect of volume diffusion, which is expected to appear homogeneously along the interfaces, measurements were performed in random area mode, i.e., tips are oriented approximately parallel to the flight axis of the atom probe without any further checking by means of FIM images. In order to detect the distinguished influence of grain boundaries, measurements were also done in selected area mode as explained later in section 5.4.2.

5.4.1 As-prepared state

The typical reconstruction of the atomic distribution inside the Cu/Py multilayer is presented in Fig. 5-3. As reported in the literature [Lang 03] and will be shown also later, there is a textured columnar growth of deposited layers close to the tip axis due to the wire texture of the tungsten substrate material which makes possible the growth of $\{111\}$ Cu and NiFe layers on top of $\{110\}$ W planes. The inset in Fig. 5-3 shows clearly resolved atomic planes mostly in the Cu layers. These layers were identified as $\{111\}$ Cu planes with an interplanar distance of about 0.2 nm which was used for calibrating the depth axis [Ene1 07]. Inside Permalloy, the lattice planes are usually less clear. This is due to a disturbance of the field evaporation sequence induced by the random arrangement of different alloy components and their different critical evaporation fields (33 V/nm for Fe and 36 V/nm for Ni) [Miller 89]. In the inset one can observe the remarkable interface sharpness: practically in 2 to 3 monolayers the composition changes from $100\text{ at.}\% \text{ Cu}$ to $100\text{ at.}\% \text{ Py}$.

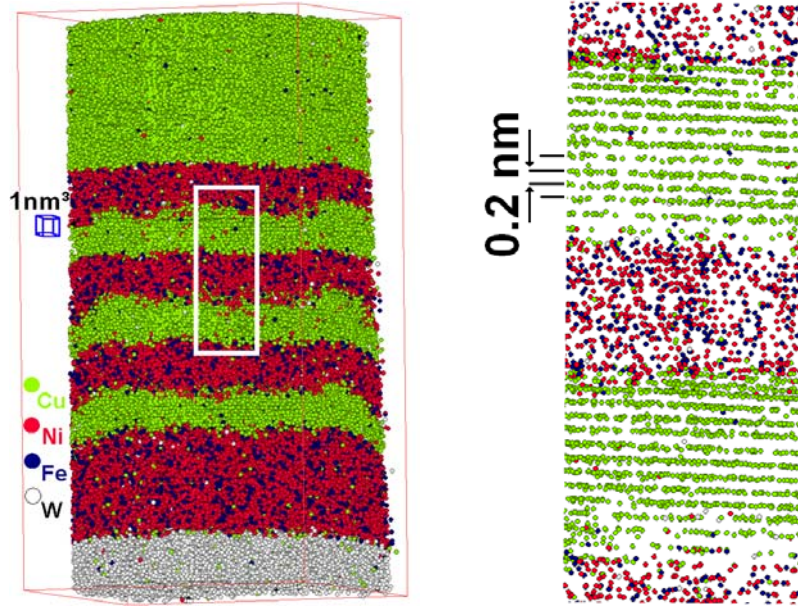


Fig. 5-3: Three-dimensional reconstruction of the atom distribution of a $W/Py_{5nm}/(Cu_{2nm}/Py_{2nm})_3/Cu_{10nm}$ multilayer in the as-deposited state with a detail at the right hand side showing clearly resolved $\{111\}$ atomic planes in Cu layers. Remarkable is the interface sharpness: the change from one material to the other takes place in less than 3 monolayers. The scale is indicated by the small $1nm^3$ cube.

The mass spectrum corresponding to the volume reconstruction shown is presented in Fig 5-4. It reveals the expected peaks for singly and doubly charged Cu ($\sim 63, 65$ amu singly charged and $\sim 31.5, 32.5$ amu for doubly charged Cu) and doubly charged Ni (29, 30, 30.5, 31 and 32 amu) and doubly charged Fe (27, 28, 28.5, 29 amu). Small traces of C are also found in the mass spectrum. Excepting a small overlap of Fe and Ni peaks at 29 amu (Fe^{58} 0.28% occurrence), the different elements are easily identified as one can observe in the graph. Thus, neglecting this overlapping, there is no need to make any correction of the mass spectrum as it is necessary for example in the case of Ni and Co, in which Co peak overlaps with two of the Ni peaks in a range of ~ 0.9 amu [Kuduz 04]. A further peak overlapping which exists between the Cu singly charged and W triply charged does not disturb, since the interesting part of measurement is the multilayer and not the W substrate. In most evaluations presented below, the results are disregarded for the first few nanometers and the later substrate part in such a way that any influence of the transient state at

the beginning of the measurement or the tungsten tip at the end of measurement are excluded (the field evaporation conditions are not reached yet and respectively influenced by the difference in evaporation fields strengths – 35 V/nm for Ni compared to 52 V/nm for W).

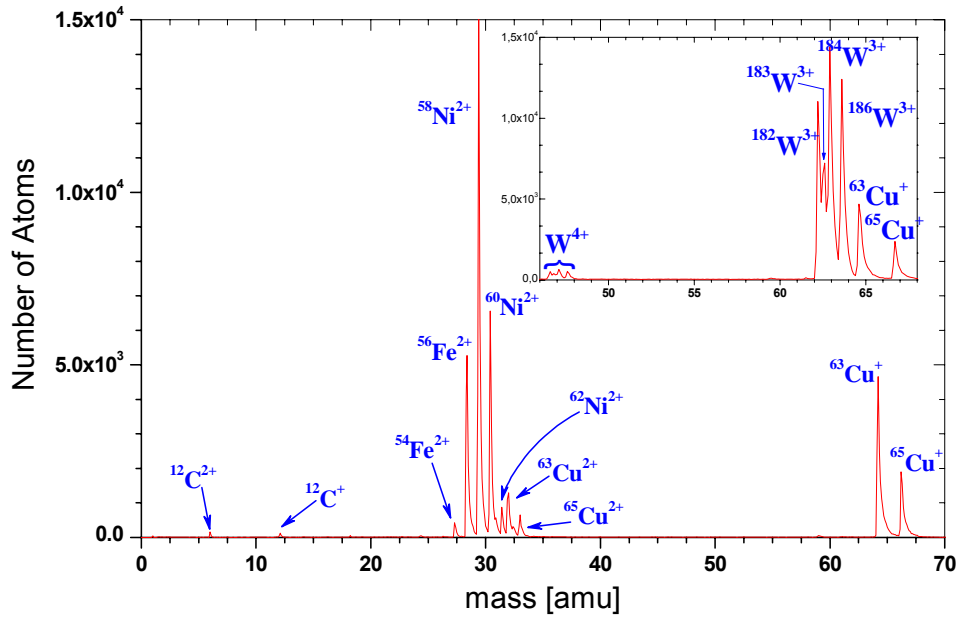


Fig. 5–4: Mass spectrum of the TAP measurement presented in Fig. 5–3. The different peaks are indicated in the picture. The measurement was interrupted right before the W substrate in order to present clearly the Cu singly charged peaks. In the inset, the mass spectrum of a measurement with three and four fold charged W peaks is presented.

The dense almost planar layer structure allows the characterization of the sample by one-dimensional composition profiles. For that, a cylinder of 3 nm radius is oriented normal to the interfaces and cut into overlapping slices 0.5 nm in thickness spaced by 0.2 nm to each other. The local composition is determined within these coarse grained volumes as described in section 3.3.2. The composition profile derived in this way is shown in Fig. 5–5, plotted vs. the measurement depth, i.e. with the axis of the analysis cylinder parallel to the direction of measurement.

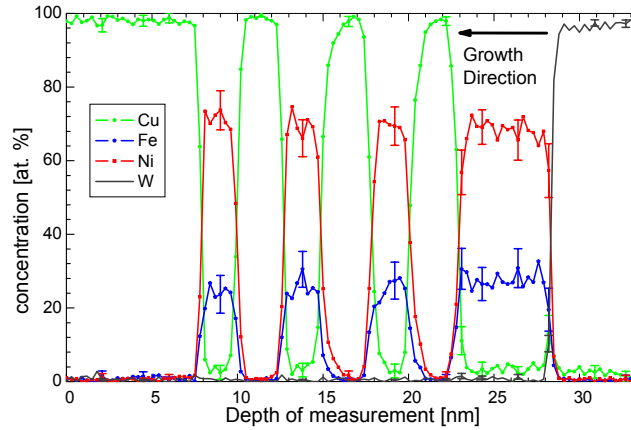


Fig. 5–5: Concentration depth profiles perpendicularly to the local interfaces using cylindrically shaped averaging volume of 6 nm diameter and 0.5 nm thickness with a step size of moving average of 0.2 nm. The error bars represent the statistical 2σ interval.

From the concentration profiles, one can determine the composition of each layer. According to the quantitative analysis, the permalloy layers seems to be slightly enriched in *Fe* compared to the composition of the alloy target. This is due to the different sputtering rates of the alloy constituents, i.e. *Ni* and *Fe*. Since the current investigation has a model character, we are not interested in obtaining the ideal magnetic properties of this alloy but we are aiming to understand the atomic transport mechanisms in the multilayer, so that this deviation in composition has not been corrected.

In the measurement shown in Fig. 5–5 as well as in all other measurements of as prepared samples the concentration profiles reveal a significant asymmetry between the interfaces on both sides of the *Cu* layers. Defining the transition zone thickness (change from one pure layer to the other) as the width between 10% and 90% of the concentration amplitude, we find for example for the measurement presented in Fig.5.5 the following numbers: 0.6 ± 0.2 nm for the interfaces where *Cu* grows on top of *Py* and 0.9 ± 0.2 nm for the interfaces where *Py* grows on top of a *Cu* layer (average over all interfaces in the multilayer). As the average on all measurements of the as prepared state, we

found $0.5 \pm 0.1 \text{ nm}$ for *Cu* on *Py* interface and $0.8 \pm 0.2 \text{ nm}$ for the *Py* on *Cu* interface stacking.

A similar asymmetry was found both experimentally by Larson for *CoFe/Cu* multilayers [Larson 01] investigated by APT and by Zhou and Wadley [Zhou 98] in molecular dynamic simulations of *Ni/Cu/Ni* trilayer, respectively. Larson found roughly a factor of two difference in the width of the intermixing zone comparing the deposition of *CoFe* on top of *Cu* ($0.7 - 1.0 \text{ nm}$) with the reversed sequence ($0.3 - 0.5 \text{ nm}$). The simulations of the *Ni/Cu* system showed a higher degree of interface mixing when *Ni* is deposited on *Cu*, compared to *Cu* deposited on *Ni*. The authors of the study explain this asymmetry by the differences in atomic-exchange probabilities. Energy barrier differences calculated from the molecular dynamics model showed that the barrier was lower for a *Cu* atom to exchange its site with a *Ni* surface atom, than for a *Ni* atom to exchange with a *Cu* surface atom. Since *Ni* is the majority component in our *Py* layers, one may regard our experimental observation as a confirmation of the MD simulations.

In conclusion, in the as prepared state we found absolutely dense layers without any breakthroughs or pinholes. Concentration profiles in Fig. 5–5, reveal an intermixing zone thickness of $0.4 - 0.9 \text{ nm}$ which corresponds to $\sim 2 - 4$ interplanar distances of the $\{111\}$ atomic planes with a pronounced asymmetry in relation to the stacking sequence.

5.4.2 Annealed state investigations

A reported effect of the thermal load is the degradation of the GMR amplitude [van Loyen 00, Heitmann 00, Hecker 02]. It was suggested, and is naturally expected that a simultaneous transformation of the microstructure is correlated to the degradation of the GMR effect. In order to investigate potential reactions, i.e. atomic transport mechanisms in the multilayer, sample structures as presented in Fig. 5–3 were subjected to different thermal treatments at temperatures between $150 \text{ }^{\circ}\text{C}$ and $500 \text{ }^{\circ}\text{C}$ for $20 - 80 \text{ min}$. From the volume

reconstructions, it is possible to distinguish two different types of the reaction development which will be presented in the following sections: volume diffusion reaction and grain boundary diffusion reaction.

5.4.2.1 Volume diffusion

The first measurements of the annealed states were done on samples thermally treated at 150 and 200 °C. As observed in Fig. 5–6 and in the composition profiles of Fig. 5–7 there is no change in the microstructure or in the chemical composition to a first sight. The result is the already known dense layer stacking which means that the initially deposited layers are preserved.

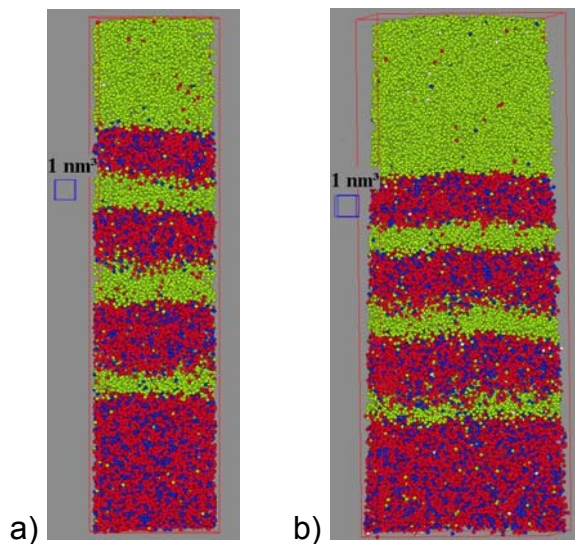


Fig. 5–6: Atomic reconstructions of thermally treated sample: a) 3nm radius cylindrical detail of a measurement after annealing 150°C/20 min; b) reconstruction of a 200°C/20 min annealed state.

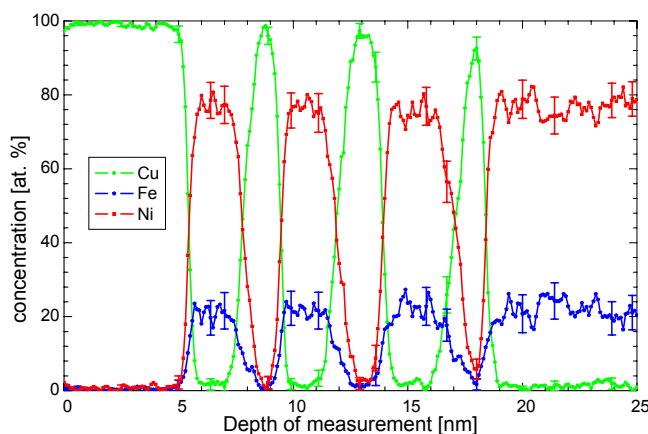


Fig. 5–7: Composition profiles after annealing at 200°C for 20min. The error bars represent the statistical 2σ interval.

The next step in the temperature scale at which we annealed our samples is the critical temperature indicated in literature, i.e. 250°C where degradation of the GMR effect was observed [Hecker 02]. At this temperature we made many measurements with different annealing times, but surprisingly again no severe structural or chemical transformation of the multilayer compared with the as-deposited state and the previous annealing temperatures (150°C and 200°C respectively) were observed. Fig. 5–8 presents the reconstruction of a $250^{\circ}\text{C}/30\text{min}$ annealed state.

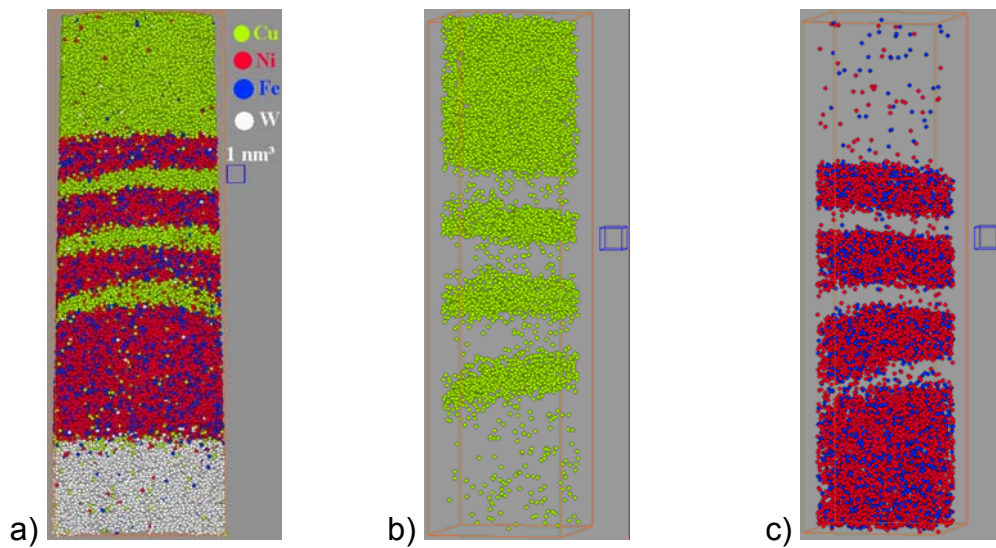


Fig. 5–8: Atomic reconstructions of a $250^{\circ}\text{C}/30\text{min}$ thermally treated sample: a) whole volume reconstruction; b) 3nm radius cylindrical detail showing only the Cu atoms (green circles); c) 3nm radius cylindrical detail showing only the Ni (red circles) and Fe (blue circles) atoms. The small cube is a $1\times1\times1\text{ nm}^3$ scale.

The composition profile of the measurement is shown in Fig.5–9. Although the first deposited Cu layer indicated by the arrow in Fig. 5–9 (in composition profiles the growth direction is from right to left as it was indicated in Fig. 5–5) does not reach $100\text{ at}\% \text{ Cu}$, which may indicate that this layer is not a dense one, it is easily seen in Fig. 5–8 b) and c) that the layer curvature is responsible for this effect. In fact, the Cu layer is closed, but the positioning of the cylinder is not perpendicularly to the local interface. This measurement was randomly made a bit aside from the tip apex and the analysis cylinder was perpendicularly oriented to 7 of the total of 9 interfaces.

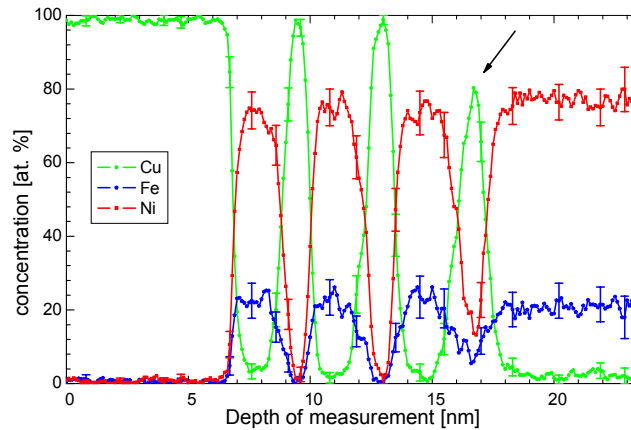


Fig. 5–9: Composition profiles after annealing at 250°C for 30 min. The error bars represent the statistical 2σ interval. The reason for the less than 100 at.% Cu of the layer indicated by the arrow is a none-perpendicular aligning of interfaces with respect to the cylinder axis.

All the measurements of samples annealed up to 250°C temperatures prove the preservation of the layered structure in contrast to the total degradation of the GMR signal. Even more puzzling is the preservation of the layered structure after thermal treatments at 300°C/20 min and even at 350°C for 20 min as can be seen in the partial reconstruction and the corresponding composition profiles presented in Fig. 5–10 and Fig. 5–11 for a 350°C/20 min annealed specimen.

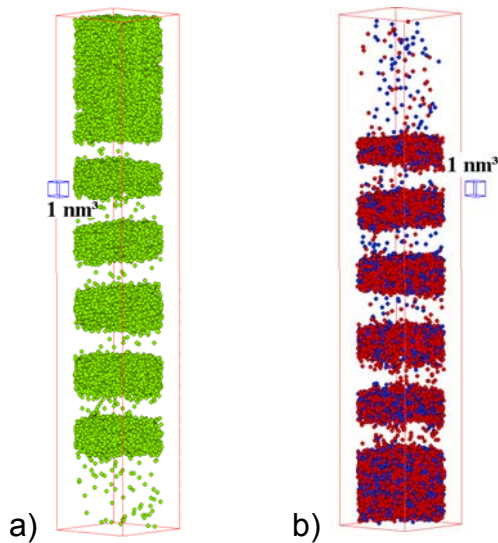


Fig. 5–10: Atomic reconstructions of a 350°C/20 min thermally treated sample:

a) 3nm radius cylindrical detail showing only the Cu atoms (yellow circles);

b) 3nm radius cylindrical detail showing only the Ni (red circles) and Fe (blue circles) atoms.

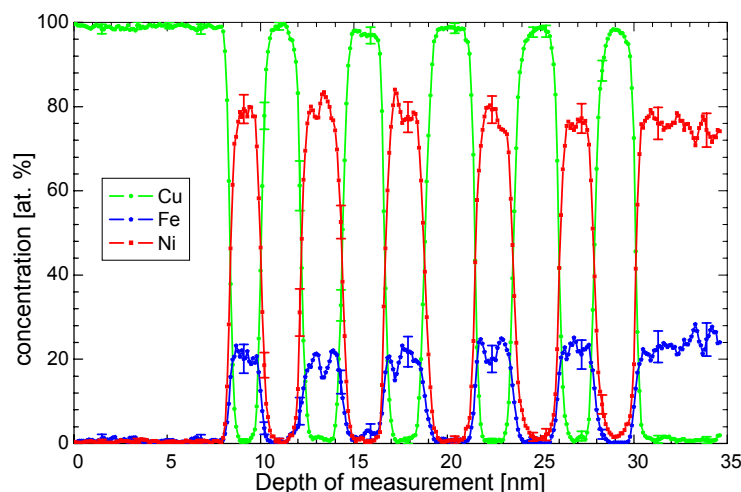


Fig. 5–11: Composition profiles after annealing at 350°C for 20 min. The error bars represent the statistical 2σ interval. Surprisingly, we still find a closed layer structure even though the annealing temperature significantly exceeds the critical temperature of GMR degradation of 250°C.

First with annealing at temperatures of 400°C and above clear chemical and structural modifications of the initial layered structure were observed. Finally, a remarkable volume diffusion of *Ni* into the *Cu* layers of up to 25 at. % *Ni* was detected for samples annealed at 500 °C for 40 min. Such an example is shown in Fig. 5–12 (a) and (b). From the partial reconstructions (Fig. 5–12), and the corresponding composition profiles (Fig. 5–13), it becomes obvious that only *Ni* diffuses into the *Cu* layer, whereas *Fe* remains at its original position. Furthermore, the mobility inside the *Cu* layer is much higher than inside *Py*, which is suggested by the difference in the melting points of the two materials. The asymmetry in the behaviour of *Ni* and *Fe* is naturally explained by the related binary phase diagrams. *Ni* and *Cu* form a well-miscible system, while only negligible contents of *Fe* are soluble in *Cu* and vice versa [Massalski 90].

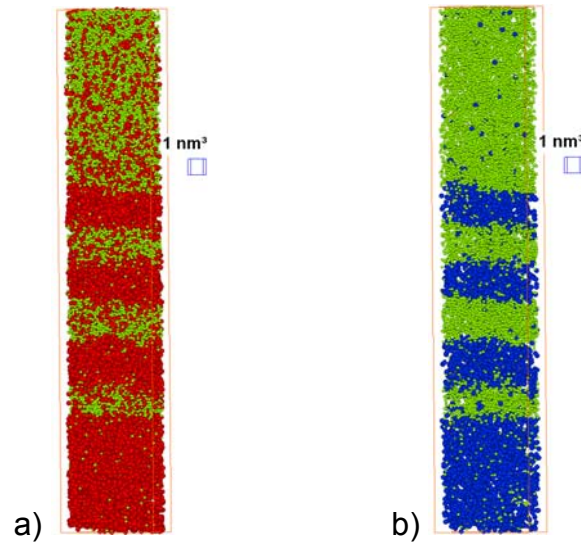


Fig. 5–12: Partial atomic reconstructions of a 500°C/20 min thermal treated sample: a) 3nm radius cylindrical detail showing only the Cu (yellow circles) and Ni (red circles) atoms; b) 3nm radius cylindrical detail showing only the Cu (yellow circles) and Fe (blue circles) atoms. While Ni diffuses into the Cu layers, no diffusion of Fe is observed.

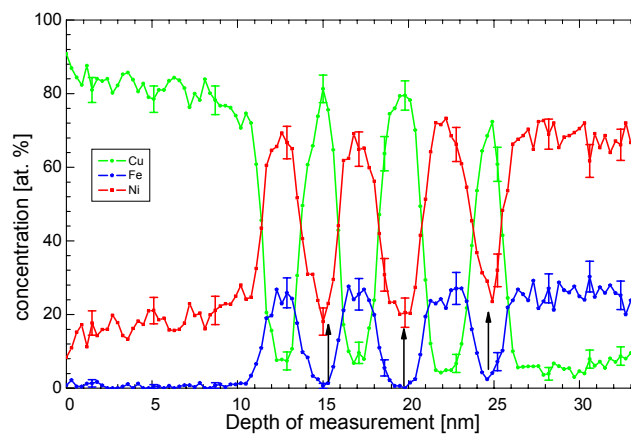


Fig. 5–13: Composition profiles after annealing at 500°C for 20 min. The error bars represent the statistical 2σ interval. The Ni content inside the Cu layers exceeding 20 at. % is indicated by black arrows.

Obviously, the thermal reaction takes place very slowly, so that the compositional profiles must be studied in detail to detect even minor modifications. As an indicator of a potential reaction, the slope of the

composition profile at the interfaces may be used. This is defined as the width between 10% and 90% of the concentration amplitude (see the inset of Fig. 5–14). Plotting the slope vs. the annealing temperature, a monotonous decrease is indicated apart from some experimental scattering.

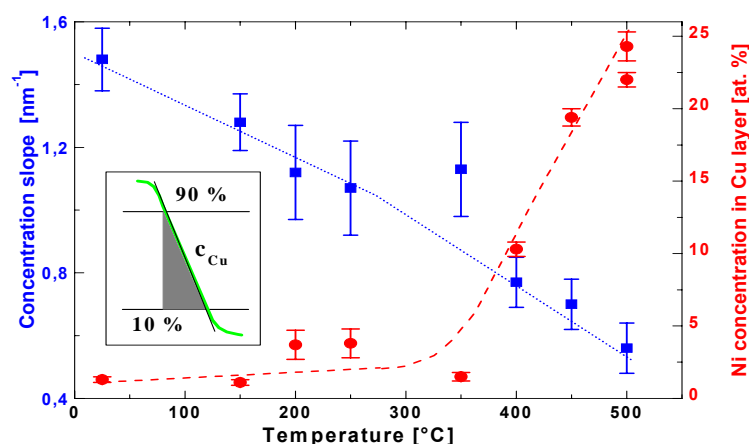


Fig. 5–14: Development of characteristic reaction indicators with annealing temperature. Blue squares: Average slope of Cu concentration at the interface. Red circles: Ni content inside Cu layers. (Isochronal treatments of 20 min.).

The Ni content inside the Cu layers may be used as an additional parameter to characterize the progress of the reaction and, therefore, is plotted in Fig. 5–14, too. The onset of significant interdiffusion leading to a mixture of Ni and Cu obviously occurs between 350 and 400 °C.

5.4.2.2 Grain boundary diffusion

The accuracy of the atomic reconstruction is sufficient to resolve lattice planes only in suitable circumstances, e.g., orientation of dense packed lattice planes almost perpendicular to tip axis, grains of sufficient size to allow a well-ordered evaporation sequence. Thus, it is a rather difficult and not reliable task to

determine grain boundaries directly from the misorientation between lattice planes. However, often at grain boundaries a reduced volume density of atoms is seen, which is due to an artefact of the field evaporation process. Hence, diluted zones can help to localize a grain boundary. The only very clear indicator for a grain boundary is provided by chemical markers, which may be due to equilibrium or dynamic grain boundary segregation.

By chance, in two measurements made after 30 *min* annealing at 400°C and 20 *min* at 450°C, a clear indication of grain boundary diffusion was observed. The corresponding reconstructions of the atom distribution are presented in Fig. 5–15. It is obvious from local enrichment of respective impurities that *Cu* migrates along grain boundaries of the *Py* layer and *Ni* along grain boundaries through *Cu* layers, as well. Owing to the accelerated transport, the layered structure appears to be almost completely destroyed in this grain boundary region. The corresponding concentration profiles determined across the grain boundaries in Fig. 5–15 (a) are shown in Fig. 5–16 and Fig. 5–17. We determine a maximum *Cu* concentration of about $54.1 \pm 5 \text{ at.}\%$ inside the *Py* layer and a maximum *Ni* concentration of $24.3 \pm 3.6 \text{ at.}\%$ at the GB inside the *Cu* cap layer. Interestingly, inside the *Cu* decorated grain boundary of the *Py* layer, the *Fe* content decreases to $3.6 \pm 1.8 \text{ at.}\%$. Obviously *Fe* is squeezed out owing to the repulsive chemical interaction between *Fe* and *Cu*.

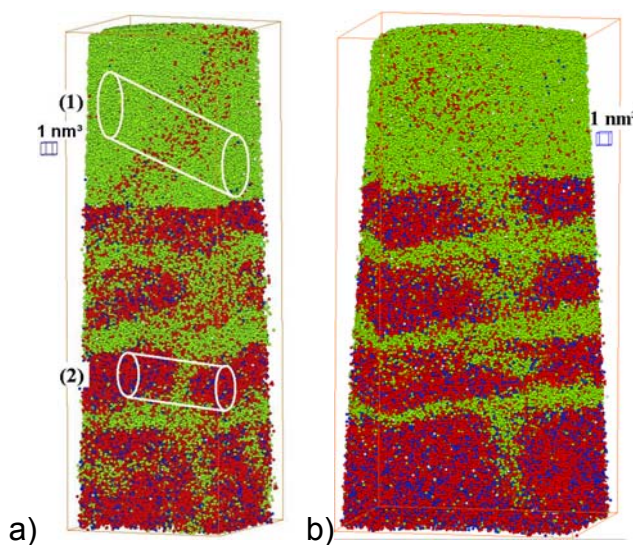


Fig. 5–15: Reconstructions of two specimens annealed at (a) 400 °C for 30 min and (b) 20 min 450°C. Ni and Cu are transported along grain boundaries. Labels (1) and (2) indicate the cylinder positions used for the composition profiles shown in the next figures.

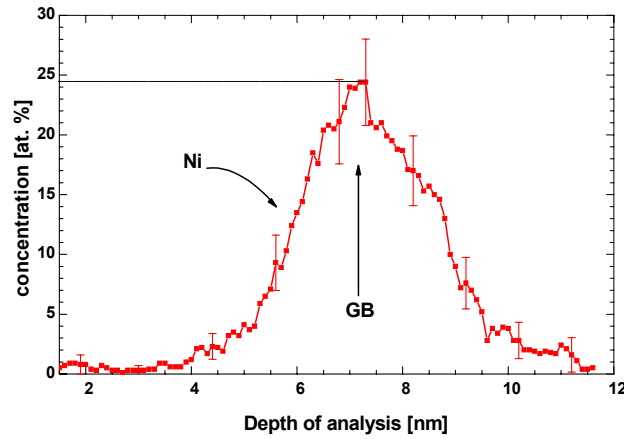


Fig. 5–16: Composition profile across a grain boundary in the Cu cap layer showing enrichment of Ni. The corresponding analysis cylinder is labelled in the reconstruction in Fig. 5–15(a) by (1).

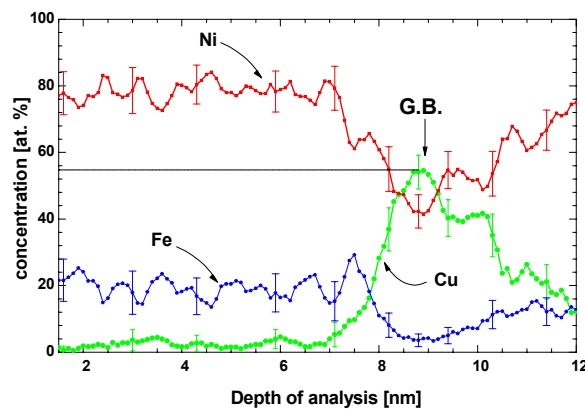


Fig. 5–17: Composition profile across a grain boundary in a Py layer showing enrichment of Cu and depletion of Fe. The corresponding analysis cylinder is labelled in the reconstruction in Fig. 5–15(a) by (2).

Although the grain boundary density on our curved substrates is already much higher than in planar systems of similar layer thicknesses [Lang 03], the chance of locating such a boundary inside the analysis volume of maximal $20 \times 20 \times 40 \text{ nm}^3$ is quite low. The grain size is obviously still considerably larger than the analysis volume, especially in the central region of the tip apex. Hence, using random area mode for the measurements, we did observe clear effects of grain

boundary transport only in two cases out of more than 40 successful measurements. However, the fact that a temperature of 400°C marks already the onset of volume diffusion with approximately $10\text{ at.}\%$ *Ni* in the *Cu* layers (see Fig. 5.14) suggests that significant grain boundary transport should begin already at lower temperatures. In order to clarify this aspect, specimens were investigated in selected area mode. That means, the microstructure of the layers is imaged in a first step by field ion microscopy with a much larger field of view ($\sim 200\times 200\text{ nm}^2$), so that grain boundary regions can be observed and located and afterwards the analyzed volume can be positioned accordingly by an off-axis tilt of the tip sample.

In Fig. 5–18 a series of FIM images of a specimen annealed at 350°C for 20 min are presented [Ene 05]. A scheme of the deduced geometry is also shown. The grain boundary structure of the thin films is seen most clearly in images of the *Cu* cap layer as shown in Fig. 5–18 (a,b). The micrograph in Fig. 5–18 (e) proves the epitaxial orientation relation expected for columnar grain morphology, since the concentric ring structure of the lattice planes often spreads coherently across several successive layers. In consequence, there is a high probability that a grain boundary observed in the upper *Cu* cap is continued into the layer system underneath and this was also seen in the reconstructions in Fig. 5–15. Thus, the experimental strategy was to image the nanostructure of the cap layer and to orient a grain boundary into the aperture area for analysis. In this way, it was possible to perform TAP measurements of selected grain boundary regions. States after annealing at 300°C and 350°C for $20 - 60\text{ min}$ were intensively investigated in order to detect the onset of grain boundary diffusion.

Fig. 5–19 (a) presents a measurement, obtained by the selected area method described above, along a grain boundary of a specimen annealed at 350°C for 60 min . Only *Ni* diffusion into the grain boundaries of *Cu* has been detected with a concentration of approximately $6\text{ at.}\%$ as one can see in the corresponding composition profiles in Fig. 5–19 (b), whereas inside the grain boundaries of *Py* no significant amount of *Cu* is seen.

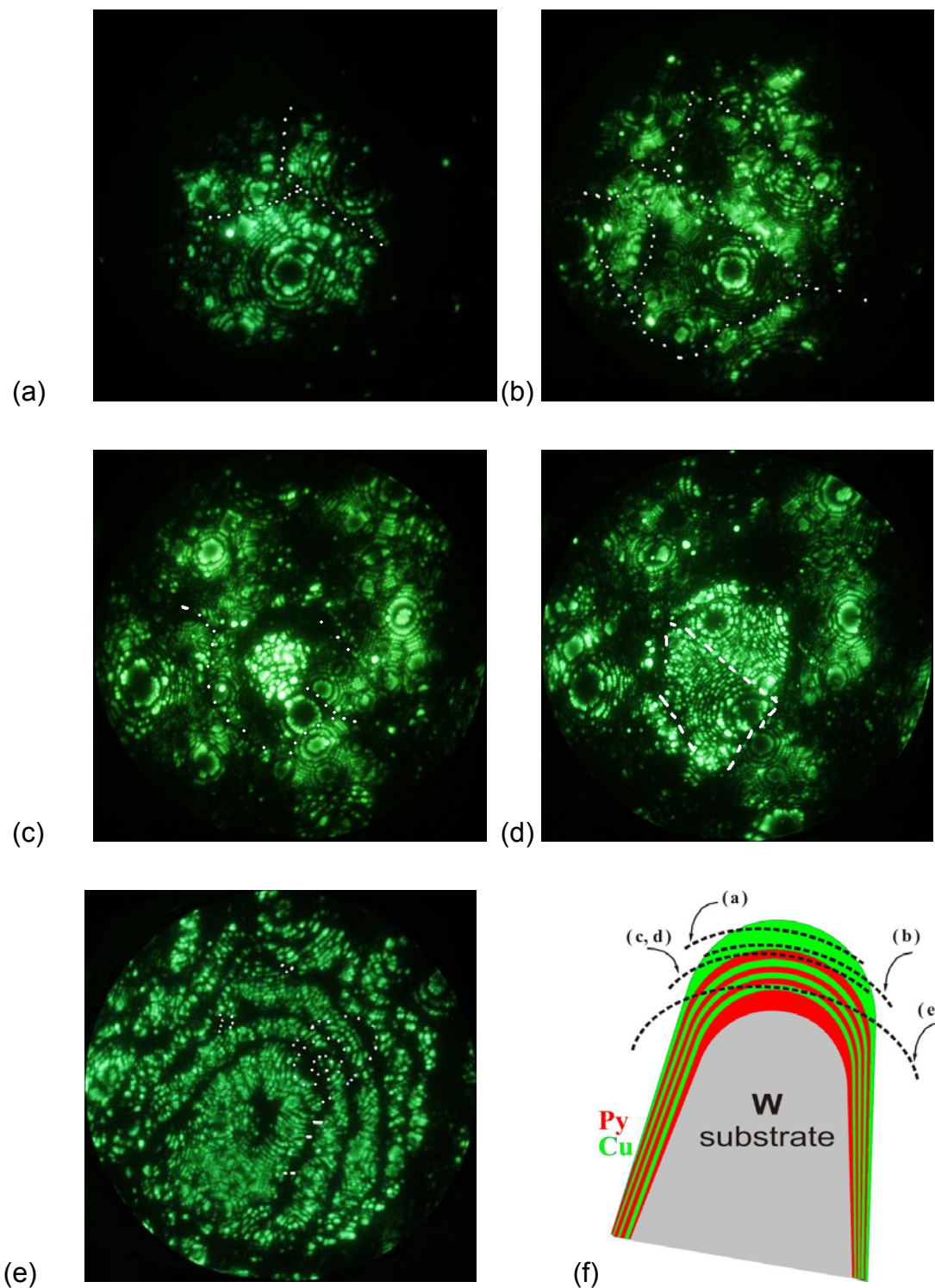


Fig. 5–18: FIM investigation of a Py/Cu multilayer (imaging gas Ne, 30 K). (a,b) Sections through the cap layer at a tip voltage of 6 kV with clear indication of grain boundaries. (c) The underlying Py (brighter spots) layer starts to field evaporate. (d) The grain structure of the Cu cap layer is preserved in the underlying layer. (e) Section through several layers, taken at a tip voltage of 7.1 kV. Py layers appear much brighter than Cu ones. Between different Py layers, a coherent lattice orientation is seen (ring structure through 5 layers). (f) Sketch of the geometry deduced from the FIM pictures.

Remarkably, several cases were found under the same annealing conditions, in which either resolved lattice planes or a 2D region of decreased atomic density indicated that the strategy to position a grain boundary into the analyzed volume worked as expected, but nevertheless no chemical segregation was seen. The grain boundary transport obviously takes place only in a smaller fraction of the grain boundaries, in dependence on the orientation relation between adjacent grains. The segregation amplitude determined from Fig. 5–19 (b) is already significantly lower than that observed at 400°C , so that it can be expected that grain boundaries no longer affect the stability of the specimens at even lower temperatures. And indeed, it was not possible to detect any segregation zone at grain boundaries in any of our specimens after annealing up to 60 min at 300°C . A very clear example is presented in Fig. 5–20. A grain boundary spreading across several single layers is indicated by a distinct mis-orientation of resolved $\{111\}$ lattice planes and locally reduced atomic density as well. Nonetheless, no segregation of any diffusing species is seen. To summarize, the results of the measurements conducted in selected area mode leads to the conclusion that the onset of significant grain boundary diffusion is between 300°C and 350°C .

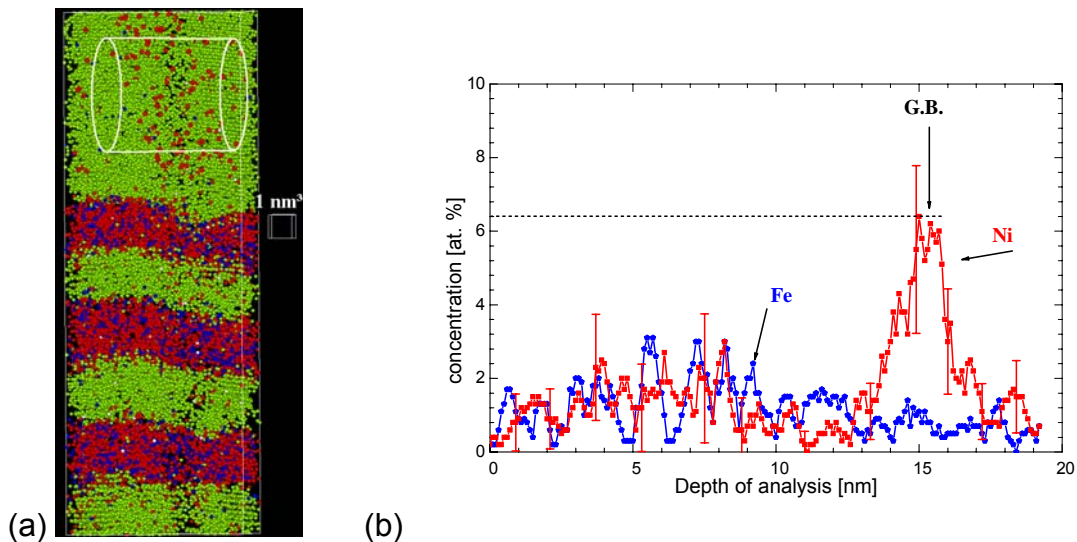


Fig. 5–19: (a) *Reconstruction of a grain boundary region after annealing at 350°C for 60 min. The grain boundary is identified by mis-orientation of lattice planes and a diluted zone almost perpendicular to the layers.* (b) *Composition profile across the grain boundary inside the Cu cap layer (see cylinder in (a)) revealing Ni enrichment.*

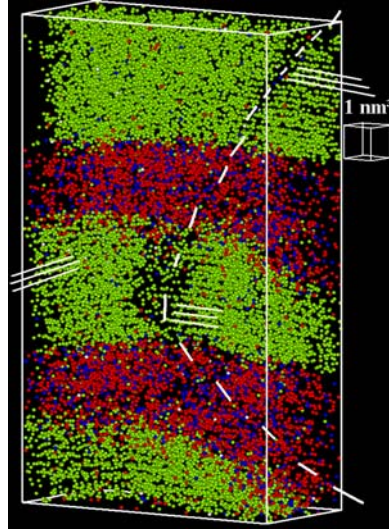


Fig. 5–20: Reconstruction of a grain boundary region after annealing at 300° C for 60 min. The grain boundary is clearly identified by a diluted zone and also indicated by the lattice plane inclination (see the white guide lines), but no segregation of any impurity is detected.

5.5 Physical interpretation

The rather sluggish thermal reaction of the multilayers demonstrated by the present nano-analysis contrasts to the GMR effect breakdown of *Cu/Py* multilayers at low temperature. Therefore, one is tempted to conclude that the behaviour of the model layers used in this study is different from that of technical systems deposited on flat substrates. However, one has to realize that the radius of curvature R of the thin films is at least a factor of 15 larger than the layer thickness w . In order to estimate the thermodynamic driving force for microstructural transformations g_V , the contribution of flat interfaces is considered:

$$g_V = \frac{\gamma_{\alpha\beta}}{w}, \quad (5.4)$$

were $\gamma_{\alpha\beta}$ is the interfacial energy. For the additional effect of the curvature the following relation holds:

$$g_V^{(c)} = \frac{2 \cdot \gamma_{\alpha\beta}}{R} \quad (5.5)$$

In all cases, the latter contribution is much less than the former for $w/R < 15$, so that a severe influence on the reaction is not very likely. In addition, one has to consider an eventual difference in the microstructures. Taking the example of *Cu/Au* layers, they are also face-centred cubic materials as majority components in the present study, it was found that grains of metallic thin films deposited on FIM tips tend to be smaller than those of comparable planar systems [Lang 03]. That means the specific microstructure of the FIM tip is likely to affect the process in terms of accelerating the degradation of the multilayer by short circuit transport along grain boundaries rather than slowing it down.

Besides these indirect arguments, it is instructive to compare in detail the reported temperature dependence of resistivity [Hecker 02] with our nano-analytical observations. Such a comparison is presented in Fig. 5–21. The *Ni* content determined inside the *Cu* layer by APT is plotted together with resistivity data of Hecker et al. [Hecker 02] versus annealing temperature. The maximum resistivity R_{max} under anti-parallel alignment of the ferromagnetic layers and the minimum resistivity under parallel alignment R_{sat} , established by a saturation field, are presented separately. The desired GMR effect is given by the difference of these two resistivities.

Indeed, it is seen that the GMR effect vanishes below 300° C. However, more important in this context, the average resistivity stays more or less constant up to this temperature to show a dramatic increase only afterwards. Since the increase of resistivity is probably induced for its major part by alloying the pure *Cu* layers with impurities, it follows that both the resistivity data obtained for planar technical systems and the nano-analysis obtained for model FIM tips, indeed reveal the same high temperature reaction. In consequence, one can

conclude that it is well justified to generalize the results obtained for our model system to technical multilayers.

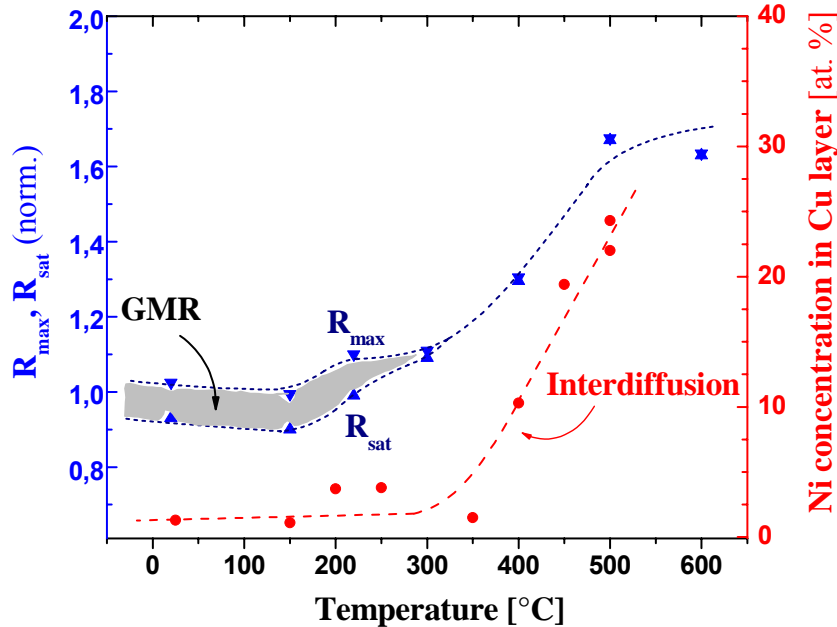


Fig. 5–21: Development of resistivity vs. annealing temperature (after Hecker) in direct comparison with the data of diffusional mixing presented in Fig. 5–14. Both microstructural parameters develop in parallel.

Hence, in agreement to the results of the nano-analysis, only two microstructural mechanisms can be held responsible for the degeneration of the GMR effect: (1) either the grain boundary transport taking place already below 400° C or (2) the short range interfacial mixing that is observed already after annealing at 150 °C which still preserves the integrity of the layer structure.

Kinetic segregation at grain boundaries may lead to boundary phases of different magnetic properties and thus to two-dimensional defects disturbing the stack of ferromagnetic layers. If sufficient diffusion of *Ni* into the grain boundaries of *Cu* takes place then these *Ni* enriched grain boundary zones could produce ferromagnetic bridges, which would magnetically shorten neighbouring *Py* layers (Fig. 5–22 (a)). Vice versa, *Cu* diffusion into the grain

boundaries of *Py* may introduce paramagnetic boundary phases that insulate *Py* grains from each other. If the grain boundary layer had an appropriate thickness in the range of $1 - 2 \text{ nm}$ (corresponding to the 1st and 2nd antiferromagnetic coupling maximums for *Cu/Py* system [Hütten 99]), depending on the orientation and properties of the grain boundary phase, this would lead to an anti-ferromagnetic coupling. In consequence a situation of frustration would develop (see scheme in Fig. 5–22 (b)), so that the overall anti-ferromagnetic coupling of the multilayer diminishes, lowering by that the GMR signal.

However, one has to realize the experimentally proven level of grain boundary segregation and to compare it with the stability of ferromagnetism in *FeNi–Cu* alloys. In Fig. 5–23, the dependence of the Curie temperatures on the *Cu* content of *PyCu* and of *NiCu* alloys are plotted, as calculated by linear superposition of the properties of the related binary systems [Massalski 90]. It is clearly seen that the observed amount of *Ni* segregation, up to $24 \text{ at.}\%$, is by some way not sufficient to form a ferromagnetic grain boundary phase. In consequence, one can rule out the magnetic bridging between two ferromagnetic layers as a reasonable mechanism. By contrast, the level of *Cu* segregation, found up to $54 \text{ at.}\%$, is sufficient to transform the grain boundary into a paramagnetic spacer phase. Thus, the isolation of *Py* grains is a realistic scheme, at least in principle. However, one has to take into account the density of these segregation defects inside the specimens and to consider whether it is sufficient to cause a total loss of the GMR amplitude.

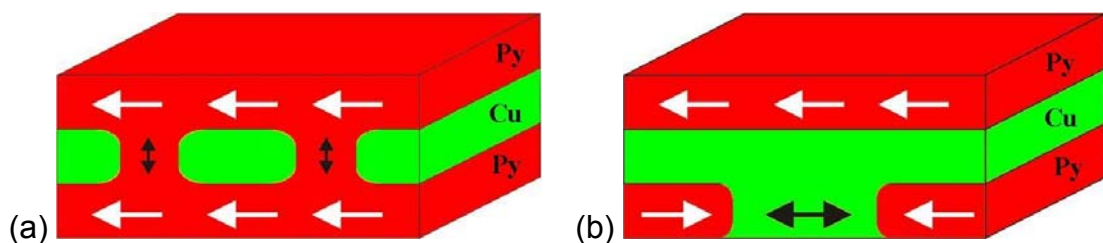


Fig. 5–22: Potential grain boundary mechanisms of GMR effect degeneration: (a) ferromagnetic bridges through Cu spacer; (b) antiferromagnetic coupling of *Py* grains across grain boundaries leading to frustration. (Orientation of magnetization is marked by white arrows; black arrows indicate the interlayer coupling.)

As a general trend, the 3-dimensional atom probe analysis demonstrated that significant grain boundary transport happens only in a smaller fraction of all investigated boundaries. The required *Cu* diffusion in grain boundaries of *Py* has been proven after annealing at 400°C , while at 350°C only *Ni* diffusion in *Cu* grain boundaries remained, yet with significantly reduced concentration amplitude. Since the melting temperature of *Py* is considerably higher than that of *Cu*, it is suggested that grain boundary diffusion in *Py* is still too slow at 350°C to produce a significant local enrichment of *Cu*. In view of the low probability of detecting grain boundary segregation after annealing at 350°C , and the failure of detecting even a single case in samples annealed at 300°C , it must be stated that grain boundary transport is not a likely process to explain the early breakdown of the magneto-resistivity in *Cu/Py* systems.

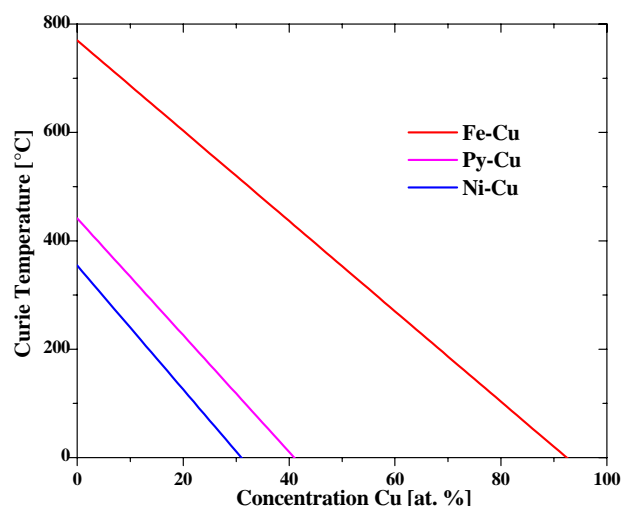


Fig. 5–23: Composition dependence of the Curie temperature of a NiFeCu alloy estimated by linear extrapolation of the binary systems FeCu and NiCu.

Hence, from all the detected mechanisms, the intermixing on a very short length scale that takes place already at 150°C remains the only candidate to explain the observed change in magneto-resistivity. Therefore, this diffusion process will be discussed more quantitatively.

The concentration profiles at the interfaces determined in these early stages are fitted reasonably by the thick film solution of the diffusion equation as shown in Fig. 5–24:

$$c(x,t) = \frac{\Delta c}{2} \left(\operatorname{erf} \left[\frac{x}{\sqrt{4 \cdot D \cdot t}} \right] - 1 \right) \quad (5.6)$$

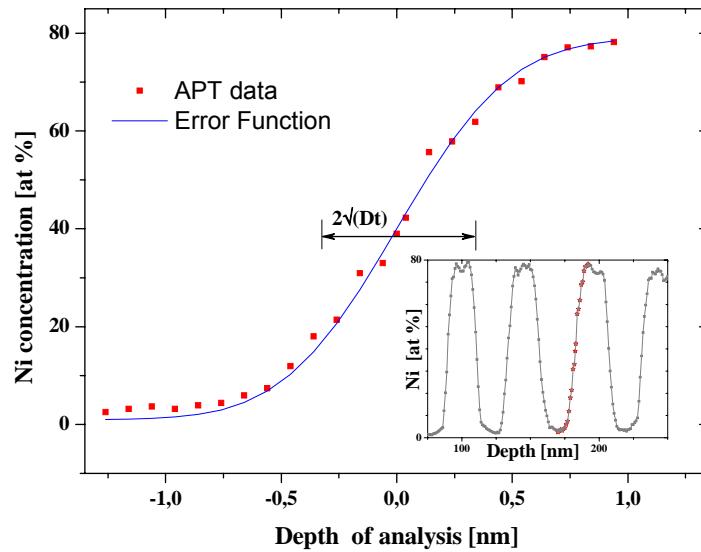


Fig. 5–24: Fit of a theoretical diffusion profile (error-function-shaped) to the experimental concentration profile obtained at the layer interface after 60 min annealing at 350° C. The inset presents the Ni profile with the red stars showing the fitted composition section.

The reasonable fit of Fig. 5–24 indicates no composition dependence of diffusivity for these short-ranged profiles. Having adapted the error function, a theoretical interdiffusion coefficient at the interface is easily determined, since the annealing time is known.

In Fig. 5–25, diffusion coefficients derived in this way are presented in an Arrhenius plot in direct comparison to appropriate diffusion coefficients stated in literature [NIMS database, Divinsky 03, Divinsky 02].

Surprisingly, from the plot in Fig. 5–25 a very low activation energy is derived, namely 0.36 eV . This value is much smaller than all known activation energy values for volume diffusion and even for grain boundary diffusion in the binary system Cu/NiFe [Divinsky 03, Divinsky 02] and this is a strong argument for a non-diffusive controlling mechanism of the interface mixing observed by APT.

Definitely, for the observed mixing at the lower experimental temperatures (up to $350\text{ }^{\circ}\text{C}$) it is difficult to provide an explanation based on thermal volume diffusion, but the homogeneity of the mixed zone along the interface which was proven by the 3D spatial resolved analysis, excludes any grain boundary effect, either. Thus, the observed short range intermixing must be controlled by a Cahn-Hilliard thermodynamic equilibrium approach of the interface as described in chapter 2.2.

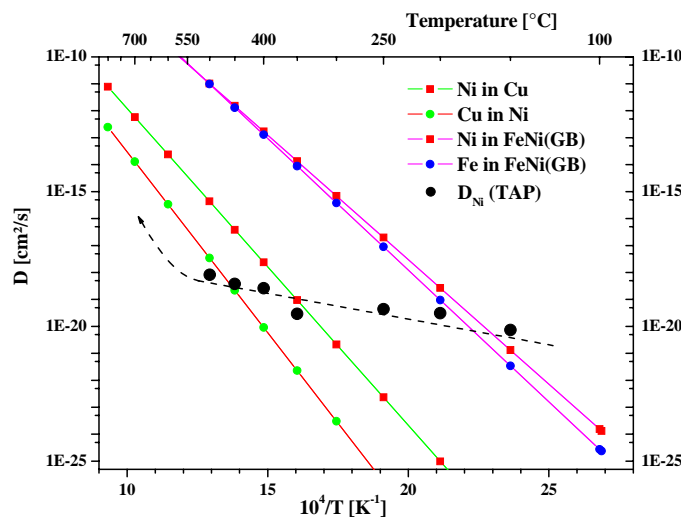


Fig. 5–25: Diffusion coefficient in comparison to literature diffusion data determined in bulk specimens.

Considering the Cu/Py as a pseudo-binary system and using the Cahn-Hilliard model described in section 2.2, the interface thicknesses obtained experimentally can be very well fitted as shown in Fig. 5–26 for a critical temperature $T_c = 1035\text{ K}$ and a gradient energy term $\kappa = 0,008\text{ eV}\cdot\text{nm}^2$.

Hence, instead of a kinetic control by limited diffusion which request much higher activation energy, we suppose a non-thermal relaxation in order to decrease the gradient of concentration and to achieve the required equilibrium at the *Cu/Py* interfaces. Thinking in terms of the length scale of the multilayer, in order to achieve this energetically minimum state at the interfaces it is enough that some of the atoms in the first two monolayers on both sides of such an interface change their sites with atoms from the neighbouring layer. Thus, it is inappropriate to consider this process as a diffusive random walk.

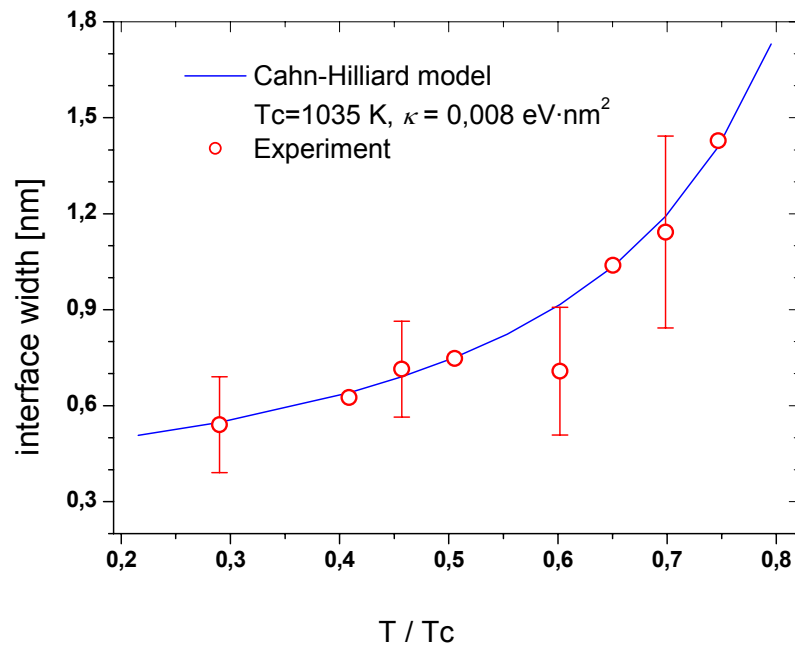


Fig. 5–26: Intermixed zone thickness versus annealing temperature. The Cahn-Hilliard model fits very well the experimental data.

In the ternary phase diagram presented in Fig. 5–27 the alloy *Cu 50 at.%, Ni 40 at.%, Fe 10at.%* is found close to the 1073 K isotherm of the miscibility gap. That means the miscibility gap closes for such an alloy above this critical temperature. This temperature is in a very good agreement with the one required for the best fit of the experimental data in Fig. 5–26. Moreover, fitting the experimental interface thickness data provided a new method for the

determination of the energy gradient term. The value obtained for $\kappa = 0,008 \text{ eV}\cdot\text{nm}^2$ is a quite reasonable one and in good agreement with recent literature data of *Ag/Cu* [Galinski 07]. The parameter λ – “interaction distance” for the pair energy can be calculated from the gradient energy coefficient. The value obtained is $\lambda = 0.3 \text{ nm}$ which is in view of the mean next neighbour distance of approximately 0.21 nm a quite reasonable number.

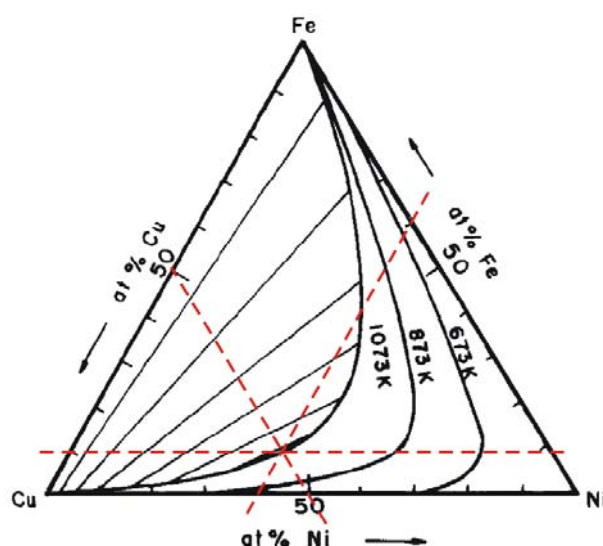


Fig. 5–27: Ternary phase diagram of Cu-Ni-Fe after [Lopez 93]. The intersection of the red lines indicates the average composition of the studied multilayers. Above 1073 K the multilayer would form a homogeneous ternary solution.

Summarizing the discussion, it has to be pointed out that a mixing of *Ni* and *Cu* at the interfaces to a depth of 0.8 to 1 nm after annealing at 300° C is sufficient to destroy the GMR signal. To understand this behaviour, one has to realize that alloying increases the scattering rate of mobile electrons and that each scattering process has a certain probability of destroying the spin coherence. In particular those electrons that cross the interlayer boundaries are essential for the GMR effect, since they do sense the orientation difference between neighbouring ferromagnetic layers. However, just these electrons are scattered

predominantly by the thin alloyed zone at the interfaces, which may explain the dramatic effect of the short-range interdiffusion. In addition, the GMR amplitude depends very sensitively on the correct thickness of the paramagnetic spacer. Initially this thickness has been optimized for pure *Cu* layers. However, if the spacer layers get partly alloyed with *Ni*, the Fermi level and thus the coupling length are changed. In consequence the optimum antiferromagnetic coupling is no longer obtained and the GMR amplitude is reduced.

5.6 Conclusions

For the first time a complete nano-analytical investigation on GMR model systems consisting of *Py/Cu* multilayers of 2 nm single layer thickness over a large temperature (150 – 500° C) and time (20 – 80 min) spectrum was carried out. Specimens have been deposited onto needle-shaped substrate tips suitable for Atom Probe Tomography investigations. The transport of the different atomic species could be determined individually owing to the atomic sensitivity of the method. Thus, very clear results on the thermal reaction and stability of this system were possible. The interpretation of the results obtained during this investigation and the comparison with other results published in the literature leads to the following conclusions.

Depending on the annealing temperature, different mechanisms of thermal reaction were detected. At very low temperatures, a short-ranged intermixing of *Cu* and *Py* layers at the interfaces to a maximum width of 1 nm is proven. The activation energy of this reaction and the comparison with known diffusion data indicates that this intermixing is based on a non-diffusive mechanism. The degree of intermixing can be accurately described by the Cahn-Hilliard model of interface equilibrium.

It was demonstrated that grain boundary transport most likely does not explain the early breakdown of the GMR effect in the *Cu/Py* system since only at

temperatures between 350°C and 400°C grain boundary transport of *Ni* and *Cu* was observed along the grain boundaries of the *Cu* and *Py* layer, respectively.

The onset of significant thermal volume interdiffusion is found after annealing at 400°C . The process leads to the solution of *Ni* into the *Cu* layers to a total content of about 25 at.% after heat treatments at 500°C . The asymmetry in the solution behaviour of the two species is naturally explained by their different melting temperatures and thus by their different mobility.

A comparison of the temperature dependence of the resistivity with the observed microstructural transformations strongly suggests that the reactions proceeding in the FIM specimens are comparable to the behaviour of planar layer systems and thus, the identified basic features of the thermal reaction may be reasonably generalized to technical systems.

According to the nano-analysis, the low temperature breakdown of the magneto-resistivity in *Cu/Py* systems is related to the short range interdiffusion of *Ni* and *Cu* on a mixing width of about 1 nm, which happens homogeneously along the interfaces without destroying the clear layer structure.

6 Investigation of Aluminium/Copper multilayer structures

This chapter presents the experimental results obtained by atom probe tomography and electron microscopy on *Al/Cu* solid state interreaction. The experimental results are discussed within the frame of a newly developed analytic model of elasticity on curved substrates, Laplace tension and stress impact on the diffusion rate.

6.1 *Motivation and state of the art*

Already in the early days of microelectronics the study of thin-film reaction became popular, when silicides have been used to form suitable contacts for the first time. Very early, it was noticed that the understanding of bulk interdiffusion couples, defined by concurrent parabolic growth of all the expected equilibrium phases, is not sufficient in the case of thin films or more generally in the early stages of the reaction. Usually, only one product phase forms at the beginning which might be sometimes even a metastable one.

The early stages of reactive diffusion in thin films are still a challenging problem, if we consider the recent achievements of nano-electronics, since nucleation and transport through a layer of only a few nanometers in thickness have been studied for a few cases only. Moreover, the use of *Al/Cu* thin films and thin-film alloys for microelectronic interconnects stimulate the interest in understanding the reaction and compound formation at the interface.

Hentzell has studied the reaction in *Al/Cu* thin film couples with different *Cu* and

Al thicknesses ratios by X-ray diffraction, RBS spectroscopy, TEM and electron diffraction to determine the phase formation sequence and the reaction kinetics. In samples with an excess amount of Cu ($Al_{270\text{ nm}}/Cu_{500\text{ nm}}$) he found that $\theta-Al_2Cu$ forms first followed by η_2-CuAl and $\gamma_2-Cu_9Al_4$ [Hentzell 83]. For samples with excess Al, the $\theta-Al_2Cu$ is the first and only phase formed. Also, the growth rate of the compound follows a parabolic law. Using X-ray diffraction and RBS spectroscopy Hamm analyzed ($Al_{160\text{ nm}}/Cu_{90\text{ nm}}$ and $Al_{180\text{ nm}}/Cu_{160\text{ nm}}$) thin film bilayers during in situ annealing in the temperature range $157-200^\circ\text{C}$. He found, in agreement with Hentzell, that the growth kinetics of the $\theta-Al_2Cu$ and $\gamma_2-Cu_9Al_4$ phase follow a diffusion limited process but he claims that $\theta-Al_2Cu$ phase grows simultaneously with $\gamma_2-Cu_9Al_4$ from the beginning of the interface reaction [Hamm 84].

Choi [Choi 03] has investigated by atom probe tomography (APT) interreaction in $Al_{30\text{ nm}}/Cu_{2.5\text{ nm}}/Al_{30\text{ nm}}/Cu_{1\text{ nm}}$ multilayer deposited on tungsten tips with the aim of studying grain boundary segregation in Al/Cu system. Nevertheless, due to the columnary growth of the layers on tungsten tips no grain boundary segregation was detected. The concentration profiles showed some particular distribution of Cu in thermally treated samples.

In a recent study, the delayed nucleation of the first product phase was proved by APT in the case of Al/Co thin-films reactions [Vovk 04]. This experimental observation was explained by the concept of a critical gradient [Pasichnyy 05]. The nucleation of the first product phase is preceded by the mere interdiffusion of both components. This diffusion appears to a maximum depth of 3.5 nm (Fig. 6-1). The first product Al_9Co_2 is observed after heat treatments at 300°C for 5 min appearing as globular nuclei, which quickly form a dense layer by particle impingement.

Based on thermodynamics, a similar behaviour may be also expected for the reaction of Al and Cu, two important components of current day metallization in semi-conductor devices. Their initial reaction is interesting in view of technological applications as well as fundamental physics and this motivates us to start this complex investigation.

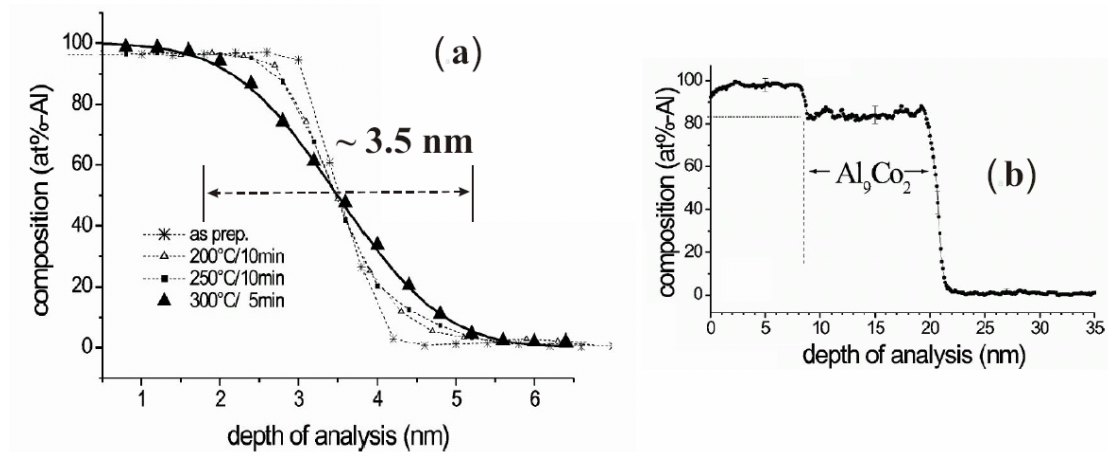


Fig. 6-1: Al/Co system: the nucleation is preceded by mere interdiffusion of both components to a maximum depth of 3.5 nm with a critical composition gradient for nucleation of 0.3 nm^{-1} (a). Composition profile showing the first product phase: Al_9Co_2 strict line compound (b). (Figures from [Vovk 03])

Assessed Al-Cu Phase Diagram

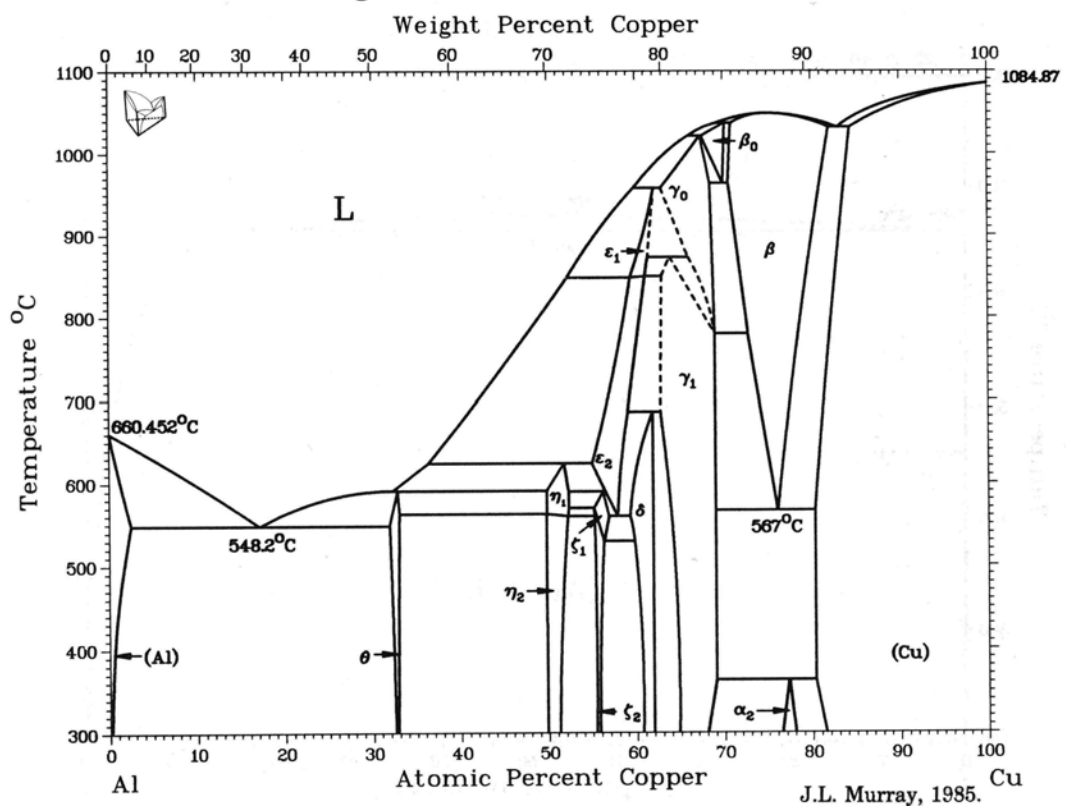


Fig. 6-2: Al-Cu phase diagram after [Murray 85].

6.2 Al–Cu System

The Al–Cu system is a very complex one with 14 stable phases [Brewer 90] as shown in the equilibrium phase diagram (Fig. 6–2) [Murray 85]. There is also a very large lattice mismatch of 12 % between the fcc Al with 0.404 nm and the fcc Cu with 0.361 nm as lattice parameters. It is straight forward that this lattice mismatch induces some elastic strain energy which is responsible for the relatively low mutual solubility. At room–temperature the solid solubility of Cu in Al is only $0.02 \text{ at. } \%$, the Al–Cu alloys tend to form precipitates of intermetallic phases.

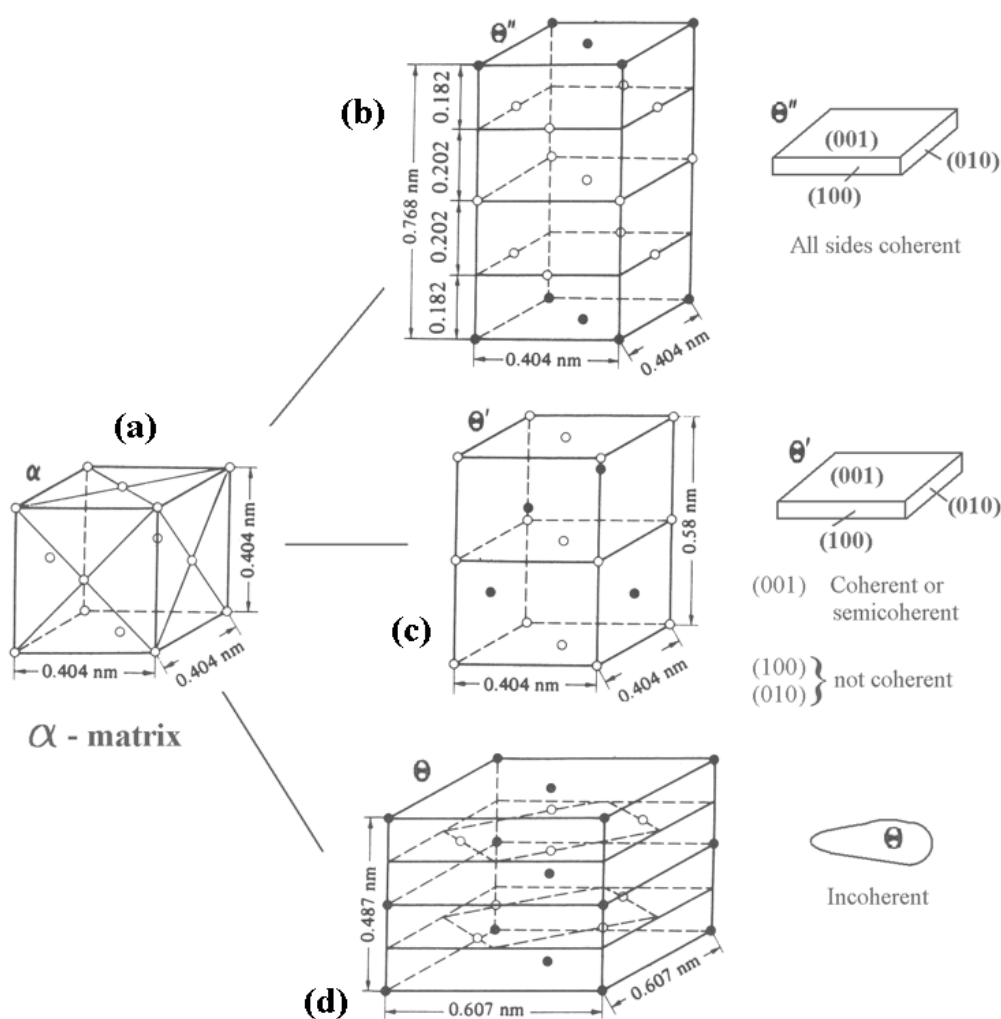


Fig. 6–3: Structure and morphology of θ'' , θ' and θ in α -Al–Cu (Al \circ , and Cu \bullet) (after [Haasen 96]).

Fig. 6–3 shows the crystal structures which appear during the precipitation process of supersaturated α -Al–Cu solid solutions (Cu concentrations higher than 2.5 at. %). According to the phase diagram (Fig. 6–2), the stable precipitate phase in equilibrium with α is the θ -Al₂Cu. As seen in Fig. 6–3 (d) it is tetragonal and completely incoherent with the matrix. That means a very high interfacial energy ($\tilde{E}_{\alpha\theta} > 1000 \text{ mJ/m}^2$ [Haasen 96]) and very high nucleation energy which permit the formation of some metastable phases *GP I* (Guinier–Preston zone), *GP II* or θ'' , and θ' (Fig. 6–3 (b, c)). These phases are more similar to the α -matrix and are partially or completely coherent with the matrix.

6.3 Experimental results in Al/Cu multilayers

The Al/Cu multilayers with typical single layer thickness of about 10 nm were deposited on tungsten pre-shaped tips and on planar Si, Cu and W substrates by ion beam sputtering using the parameters indicated in Table 4.1. The experimental results obtained in as-prepared state and after different thermal treatments are presented in the following. The different samples were investigated by Atom Probe Tomography (APT) and Transmission Electron Microscopy (TEM). The majority of the investigated samples deposited on W tips were of sandwich-type Al/Cu/Al. For comparison, a few samples were deposited in the reversed stacking sequence Cu/Al/Cu. Also, planar deposited multilayers like *Substrate/ (Cu/Al)_{3–12}* were investigated.

6.3.1 As-prepared state

In Fig. 6–4 a TEM micrograph of an as-prepared Al/Cu/Al sample is presented. The layers are symmetrically grown on the curved substrate. The typical volume reconstructions of the Al/Cu/Al and Cu/Al/Cu trilayers in the as-prepared state are shown in Fig. 6–5. The textured columnar growth is found here also as

reported earlier for the *Cu/Py* multilayers. Clearly resolved *Cu* {111} planes are presented in the inset in Fig. 6–5 (b).

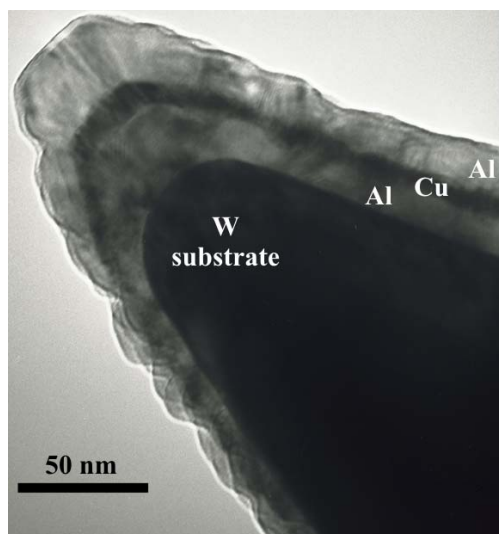


Fig. 6–4: TEM micrograph of an Al/Cu/Al trilayer with enlarged Al layer thickness deposited on a W substrate tip.

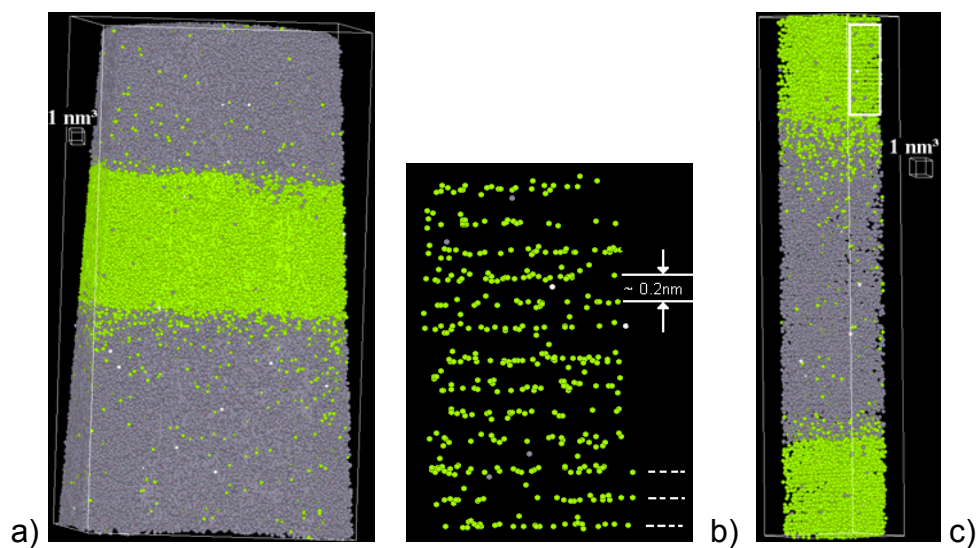


Fig. 6–5: (a) Three-dimensional reconstruction of the atom distribution of an Al/Cu/Al trilayer in the as-deposited state. In the inset (b), {111} atomic planes resolved in the Cu layer are shown. (c) 3 nm radius cylindrical detail of reversed stacking sequence Cu/Al/Cu in the as-prepared state.

The mass spectrum corresponding to the volume reconstruction shown in Fig. 6–5 (a) is presented below (Fig. 6–6). As in the case of *Cu/Py* multilayers, the mass spectrum reveals mainly single and doubly charged events for copper and aluminium, very small amounts of oxygen and carbon singly charged and aluminium triply charged. Due to the low evaporation field strength of *Al* (19 V/nm), a small amount of aluminium hydrate singly charged was detected, as well.

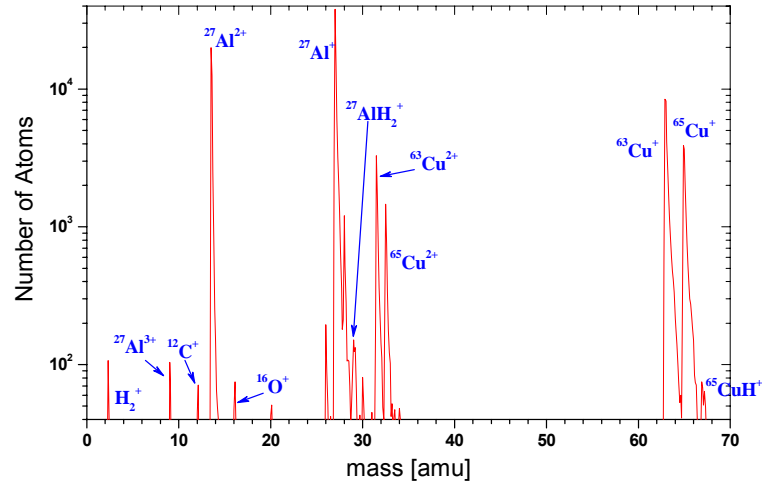


Fig. 6–6: Mass spectrum of a measurement as–prepared Al/Cu/Al. The different peaks are labelled in the figure. No W substrate was measured for this sample (tip fracture at the layer/substrate interface) of as–prepared state.

Composition profiles across the reconstructed volumes (Fig. 6–7) reveal a dense layer structure with significant asymmetry between the interfaces on both sides of the middle layer (either *Cu* or *Al* depending on the deposition sequence). Using the same definition for the transition zone thickness as in section 5.4 namely the width between 10% and 90% of the concentration amplitude, we obtain for the average over all the as–prepared measurements 1.4 ± 0.3 nm for the interface where *Al* was deposited on *Cu* and 2.1 ± 0.2 nm for *Cu* growing on *Al* interface. The higher degree of intermixing at the *Cu* on *Al*

interface is in agreement with SRIM simulations of the ion mixing process. The presence of the shoulders indicated by the blue arrows in Fig. 6–7 may be an indication for a phase formation during the deposition.

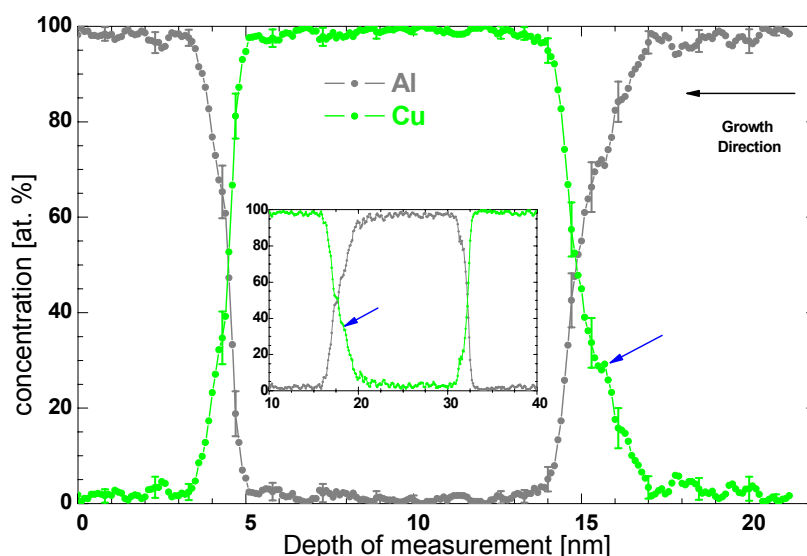


Fig. 6–7: Concentration depth profiles of the Al/Cu/Al trilayer with an inset of the reversed deposition sequence Cu/Al/Cu, both in as-sputtered state. These were taken perpendicularly to the local interfaces in cylindrically shaped volumes as the one shown in Fig 6–5. The error bars represent the statistical 2σ interval.

6.3.2 Thermally treated samples

Most of the specimens were annealed at 110°C for 5, 10, 20, 40 and 80 minutes. For comparison a few samples were also annealed at temperatures above 110°C , but already $130^{\circ}\text{C}/10 \text{ min}$ was found to be too high for the Al/Cu/Al multilayer configuration because the whole Cu layer was consumed in the reaction.

The local chemical analysis performed on these thermally-treated specimens show the direct formation of a dense layer of the reaction product. This is already present after 5 min annealing at 110°C . No precursory interdiffusion

and no distinct nucleation of the product in terms of isolated nuclei were observed, in remarkable contrast to the findings at Al/Co (Fig. 6–1). The following pictures (Fig. 6–8 and Fig. 6–9) present the three-dimensional reconstruction of the atom distribution and the concentration depth profiles of two samples: Al/Cu/Al and Cu/Al/Cu both annealed for 40 min at 110°C.

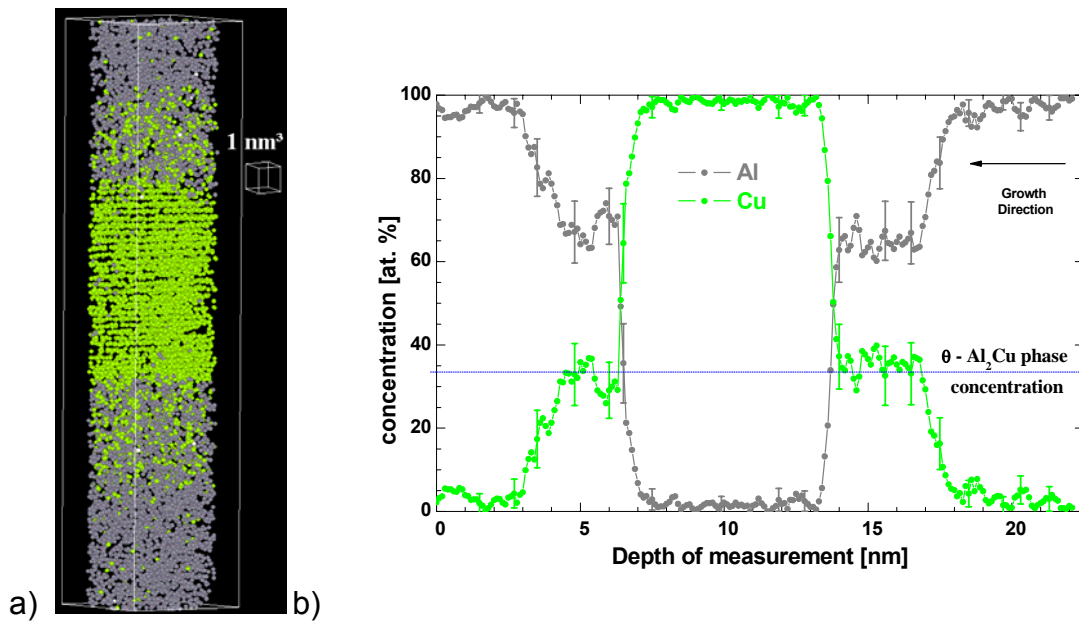


Fig. 6–8: (a) 2.5 nm cylindrical detail of an Al/Cu/Al trilayer annealed at 110°C for 40 min. (b) Concentration depth profiles of the volume. The error bars represent the statistical 2σ interval.

Most remarkably, the asymmetry seen already in the as-prepared state is preserved demonstrating different growth rates of the product phase at the interfaces of opposite stacking sequence. It is clearly seen in the two above figures that the thickness of the product layer at the Cu on Al interface differs from that at the Al on Cu interface. Moreover, changing the deposition sequence from Al/Cu/Al to Cu/Al/Cu, it was found that in one case the inner interface, directed towards the tungsten tip, grows faster, but in the other case, the outer interface is the faster growing one.

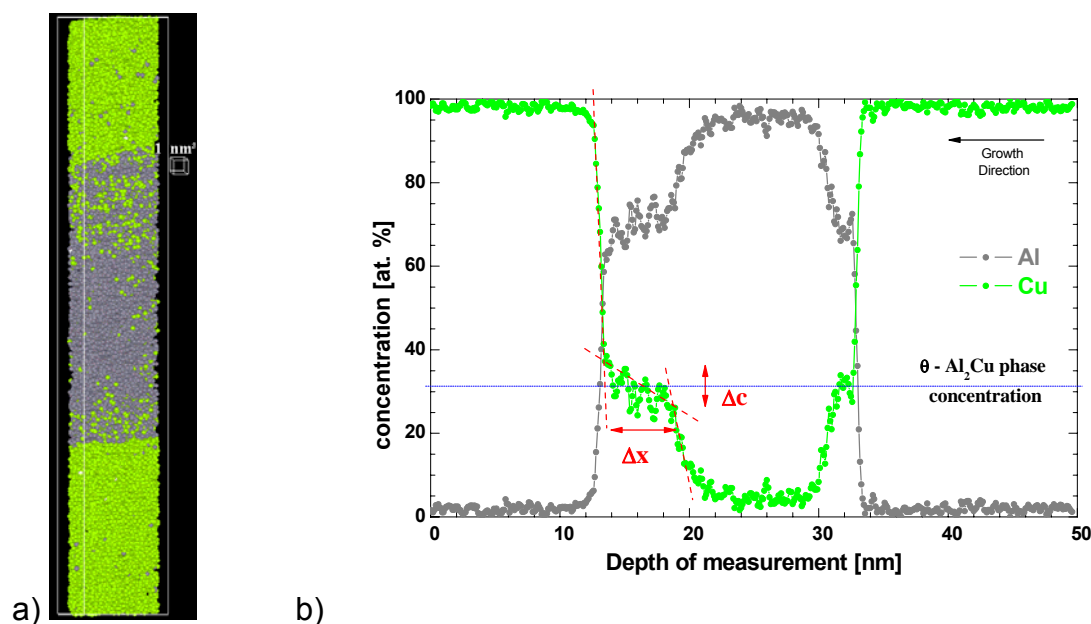


Fig. 6–9: (a) 3 nm cylindrical detail of a Cu/Al/Cu trilayer annealed at 110°C for 40 min. (b) Concentration depth profiles of the volume. The product phase thickness and the concentration range were determined as sketched by the red arrows.

As an example, the thickness of the phase grown after 80 min annealing at 110°C for Al/Cu/Al deposition sequence is found to be 5.9 ± 0.8 nm at the interface where Cu was deposited on Al and 3.8 ± 0.6 nm at the other interface at which Al was sputtered on top of an already deposited Cu layer. In figure (Fig. 6–10) a comparison between as prepared and annealed state (110°C/40 min) is made using 2–dimensional composition maps of Cu. One observes that the initial mixing at the interfaces is always thinner for the Al on Cu interface (Fig. 6–10 (a) upper interface and (c) lower interface) than for the Cu on Al interface. The evolution after the thermal treatment maintains the same trend with thinner reaction product layer at the initially sharper interface and vice versa.

A comparison between the chemical composition (Fig. 6–8 and Fig. 6–9) and the phase diagram of Al/Cu system (Fig. 6–2) suggests that the Al₂Cu – θ phase has formed as first reaction product. Previous investigations have shown

also the θ phase as the first or one of the first reaction products [Hentzel 83, Hamm 84]. Furthermore, using the effective heat formation rule, Pretorius predicts the θ phase as the first reaction product in the Al/Cu interreaction [Pretorius 91].

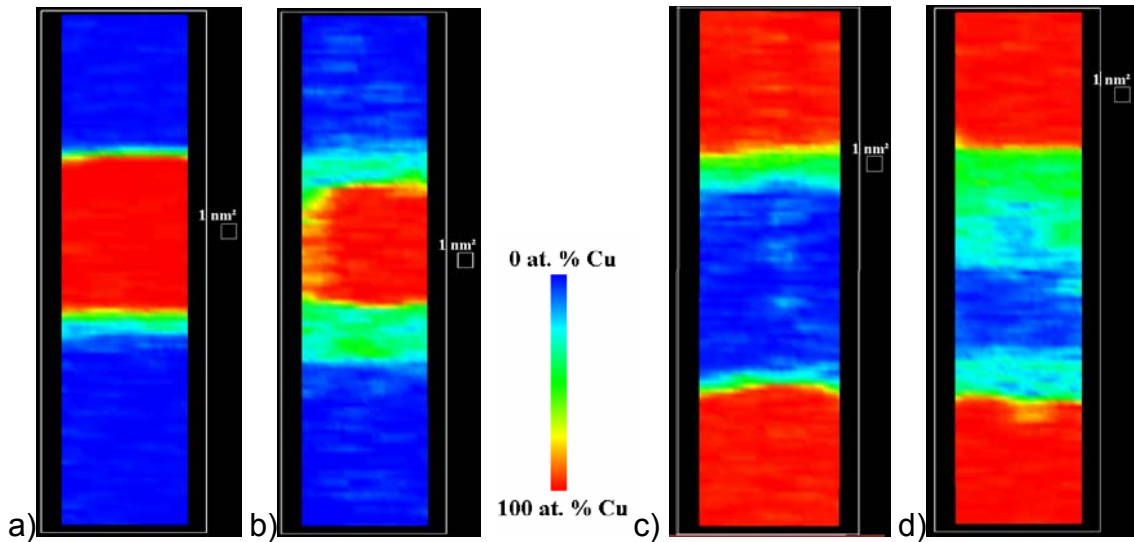


Fig. 6–10: 2-dimensional composition maps of $Al/Cu/Al$ ((a) as-prepared and (b) 110°C 40 min annealing) and $Cu/Al/Cu$ ((c) as-prepared and 110°C 40 min annealed (d)). Asymmetry in layer thickness is preserved from the as-prepared state to the thermally treated state.

It is presumably due to the absence of any other intermetallic phase of higher Cu concentration that the existence field of the phase is significantly broadened with respect to the equilibrium phase diagram and the macroscopic interdiffusion experiment (see Fig. 6–11 and Appendix A). Since the product layer forms from the beginning of the reaction without any nucleation barrier it is unlikely that the phase formed is the incoherent θ phase. But, at the same chemical composition, one finds the θ' metastable phase (see Fig. 6–3) which has coherent or at least semi-coherent interfaces to the terminating of fcc structure Al and Cu layers. Yet, very important, the θ' phase reveals an excess volume of 6% compared to the volume of the constituent pure metals which means that during the reaction elastic stress may develop.

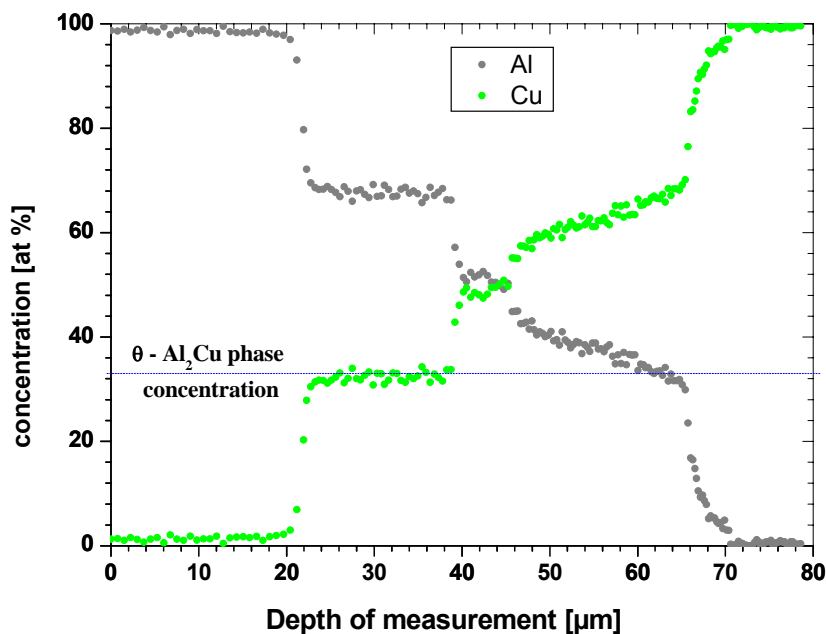


Fig. 6–11: Composition profiles of a macroscopic Al–Cu reaction couple after 120h annealing at 410°C as determined by electron microprobe analysis.

The average, calculated over all atom probe measurements, shows the composition range of the Al_2Cu product phase spreading from $c_{min} = (32 \pm 1)$ to $c_{max} = (39.5 \pm 1)$ at% Cu. However, the existence range of the phase field in the macroscopic reaction couples as well as in published phase diagrams hardly exceed 1 at%. The two concentrations, c_{min} and c_{max} , were determined as the interception of the tangents drawn on the product phase “plateau” and the interfaces between the phase and the Al layer and the phase and the Cu layer as sketched in Fig. 6–9 (b).

The growth of the product layer was determined by APT during a series of isothermal annealing at 110°C (see Fig. 6–12) in the Al/Cu/Al deposition sequence. At both interfaces the thickness of the product layer depends parabolically on time, though with a different growth rate.

Since no influence of grain boundary transport on the length scale of the reaction is seen in the atomic reconstructions, the experimentally determined growth rate may be used to evaluate the volume interdiffusion coefficient of the reaction product.

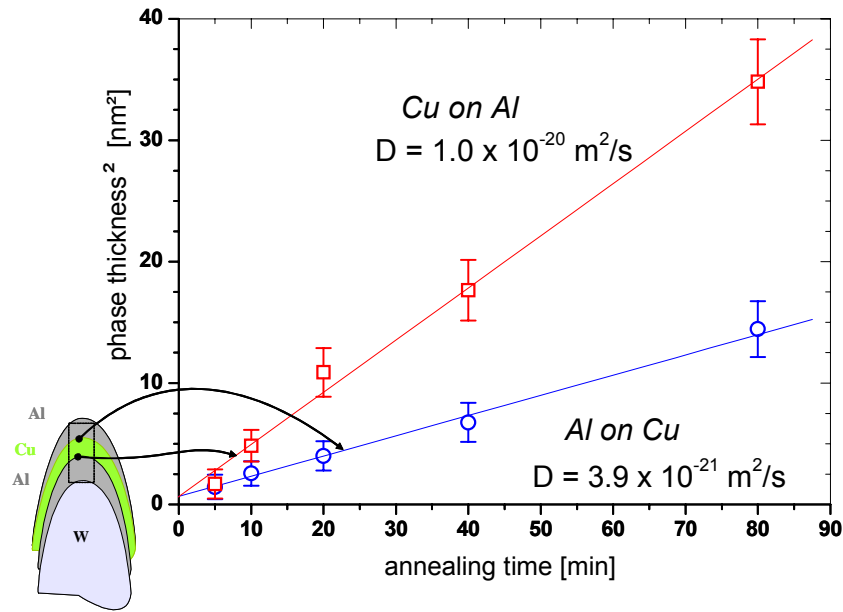


Fig. 6–12: Asymmetrical parabolic growth of the Al_2Cu product phase in the Al/Cu/Al stack. Isothermal annealing at 110°C .

In a first order approximation, the composition profile across a Cu/Al interface with an already formed intermetallic reaction product is modelled as sketched in Fig. 6–13. The terminating phases are almost pure Al and Cu and c_{\min} and c_{\max} at the product phase boundaries are determined by APT. The growth rate is determined by the diffusion flux across the product layer and the compositional discontinuities at the phase boundaries according to:

$$\frac{dw}{dt} = \frac{dx_2}{dt} - \frac{dx_1}{dt} = j\Omega \left(\frac{1}{c_{\min}} + \frac{1}{1 - c_{\max}} \right) \quad (6.1)$$

$$\frac{dw}{dt} = -\tilde{D} \frac{c_{\min} - c_{\max}}{w} \left(\frac{1}{c_{\min}} + \frac{1}{1 - c_{\max}} \right) \quad (6.2)$$

$$\Rightarrow \tilde{D} = \frac{1}{2} \left(\frac{c_{\max} - c_{\min}}{1 - c_{\max}} + \frac{c_{\max} - c_{\min}}{c_{\min}} \right)^{-1} \cdot \frac{d(w^2)}{dt} \quad (6.3)$$

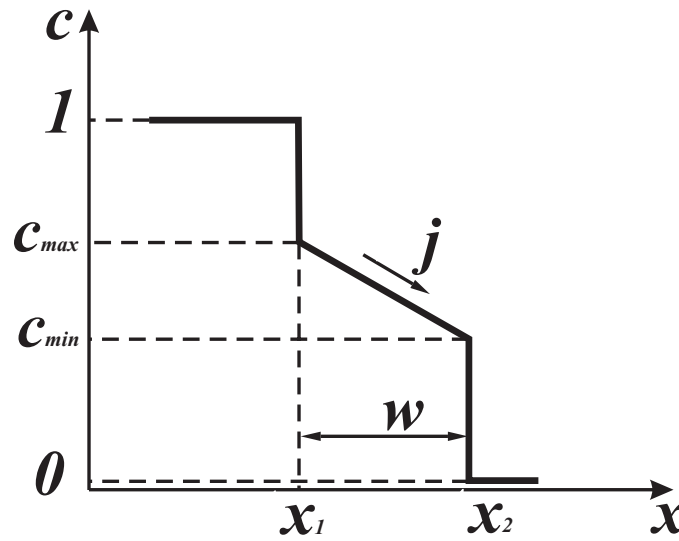


Fig. 6–13: Schematic composition profile through a reaction zone with one reaction product. For simplicity, the solubility of terminating phases is assumed to be negligible.

The variables \tilde{D}, Ω denote interdiffusion coefficient and atomic volume, respectively. Further symbols are defined in the schematic diffusion profile sketched in Fig. 6–13. As the annealing times t are known and the phase thicknesses w are determined from the APT derived composition profiles, volume interdiffusion coefficients can be evaluated using relation (6.3). This way, from the data in Fig. 6–12, interdiffusion coefficients were determined to be $D_{Cu \text{ on } Al} = 1 \times 10^{-20} \text{ m}^2/\text{s}$ and $D_{Al \text{ on } Cu} = 3.9 \times 10^{-21} \text{ m}^2/\text{s}$ [Ene2 07]. Besides the remarkable asymmetry, these values are more than one order of magnitude larger than the extrapolated literature value for interdiffusion coefficient in the $\theta - Al_2Cu$ phase $D_{Lit} = 1.9 \times 10^{-22} \text{ m}^2/\text{s}$ [Funamizu 71].

Owing to the severe preparation conditions, only a small fraction of the FIB-prepared specimens originating from planar substrates withstand the field evaporation in APT. The measured FIB-prepared samples show nearly complete mixing of the layers with a different composition as the one obtained in specimens deposited on curved substrates. In Fig. 6–14, the composition profile of an APT measurement using a FIB-prepared specimen is presented. The almost complete mixing of the multilayer is probably due to the ion–solid interaction which induces local heating above the interreaction temperature of the *Al/Cu* system. Hence, a comparison with reliable APT results of multilayers deposited on planar substrates is impossible.

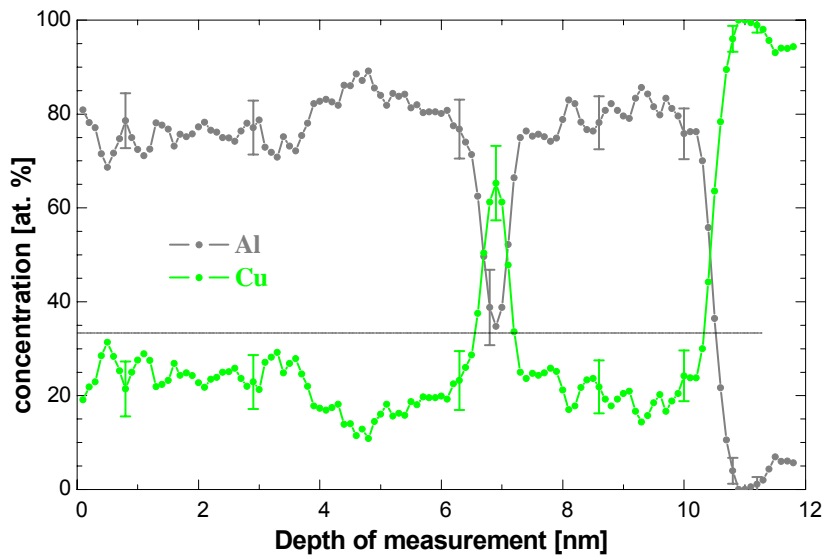


Fig. 6–14: Concentration depth profiles of the $(\text{Al/Cu})_4$ multilayer deposited on Cu planar substrate obtained by APT. The sample was annealed prior FIB preparation at 110°C for 80 min.

Nevertheless, a comparison with planar deposited layers was possible by the investigation of FIB-prepared TEM samples (Fig. 6–15). Within the error bounds of measurement, always identical growth rates are observed in both stacking sequences on the planar substrates while the average growth rate are in good agreement with the ones obtained on curved substrates.

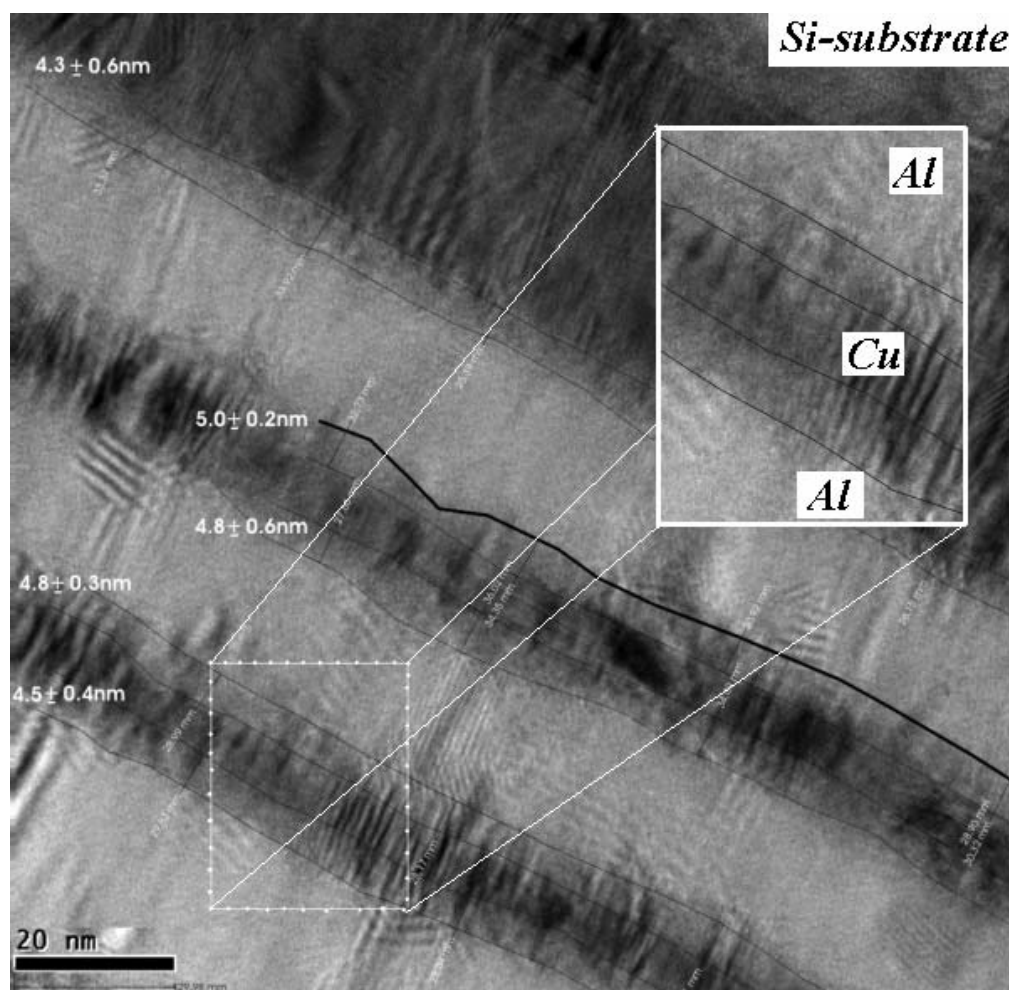


Fig. 6–15: TEM micrograph of a $\text{Cu}_{50\text{nm}}/\text{Al}_{20\text{nm}}/\text{Cu}_{10\text{nm}}/\text{Al}_{20\text{nm}}/\text{Cu}_{10\text{nm}}/\text{Al}_{100\text{nm}}$ multilayer deposited onto planar silicon. The sample was annealed 80min at 110°C . The thickness of the product phase is equal at both sides of the Cu layer.

The thickness of the reaction product in the case of the planar deposited sample was determined graphically by the contrast observed in the TEM micrograph as sketched in Fig. 6–15. Since no growth asymmetry of the product phase is observed in the case of planar samples, deposition-induced defect densities can be ruled out as potential reason for the asymmetry. Hence, the remarkable effect must be related to the spherical geometry of the tip-shaped samples.

6.4 Layer mismatch and elasticity on curved substrates

The starting point of this consideration is the presumable formation of the metastable θ' with a 6% excess volume as the first and only reaction product in the *Al/Cu* interreaction experiment. In the following, a theoretical model of the stress induced by volume expansion of the reaction product, its development and influence on the interreaction rate will be evaluated [Ene3 07].

Elastic stress induced by the solid state reaction might play a decisive role in explaining the above asymmetry if one takes into account the long-ranged nature of the elastic stress and therefore its dependence on the sample's geometry as a whole. Nevertheless, if only excess volume of the solid state reaction has to be accommodated on the planar geometry, then nature finds usually a way to relax a part of the stress. The simplest example is the volume expansion of a reaction product formed between two reactive layers on top of a planar substrate. This volume change may be obtained entirely by strain directed perpendicular with respect to the layer interfaces since the top surface of the thin film package can freely move (Fig 6–16 (a)). If the interfaces are incoherent or at least semi-coherent, if plastic relaxation or creep are possible within the newly formed material, this orientation of strain into the perpendicular direction can be always obtained. Thus, no stress is induced in the system by such an expansion mode. An analogous expansion mode without any induced stress is not possible in a curved geometry, as will be shown beneath.

In the following, the stress evolving during the reaction between a spherical calotte (I) of material *A* and a layer (III) of material *B* as well as between layer (III) and the topmost coating layer (V) of *A* material (see Fig. 6–16 (b)) will be calculated. This may serve as an approximate model for the situation at the tip apex. Around the curved two interfaces (I/III and III/V) at first layers of thickness w^{II} and w^{IV} (inner and outer product layer), containing appropriate amounts of *A* and *B* are cut out of the volume and transformed under stress-free expansion

into the new phase. In a second step, the reaction layer as well as the remaining sample structure is elastically deformed to refit the reacted material into the empty space. The stress required for this deformation is calculated in the frame of linear theory of elasticity assuming homogeneous and isotropic elastic constants throughout the specimen.

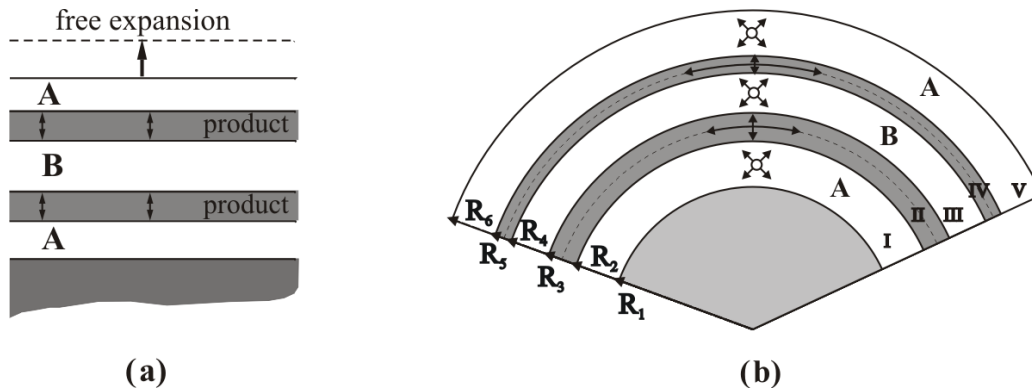


Fig. 6–16: Insertion of product layers with excess volume in between two reactive components in planar (a) and curved (b) layer geometry. Opposed to the planar case, in curved geometry the expansion to achieve the excess volume appears in both directions, normal and lateral as well. Elastic theory predicts compressive and dilatational stresses in the inner and outer terminating layers, respectively.

Due to the spherical symmetry of the problem any possible displacement is directed in radial direction. The strain to produce the excess volume might be split in perpendicular and lateral stress-free strain (ε_{\perp} , ε_l). A perpendicular strain will increase the thickness of the transformed material, while the intermediate spherical surface $4\pi(\bar{R}^{II})^2$ or $4\pi(\bar{R}^{IV})^2$ will be unmodified (\bar{R}^{II} , \bar{R}^{IV} is the average radius inside the new product phases – dotted circular arcs in Fig. 6–16 (b)). Thus, the inner and outer boundary of the transforming layers must be displaced symmetrically into opposite directions. On the other hand, lateral strain will keep the thickness w^{II} or w^{IV} unmodified, but increase the area of the intermediate surface, which means both radii (R_2 and R_3 or R_4 and R_5) need to be displaced outwards. Hence, the stress-free displacements have the following form:

$$u_2 = \varepsilon_l \cdot \bar{R}^{II} - \frac{1}{2} \varepsilon_{\perp} \cdot w^{II}; \quad u_3 = \varepsilon_l \cdot \bar{R}^{II} + \frac{1}{2} \varepsilon_{\perp} \cdot w^{II} \quad (6.4)$$

$$u_4 = \varepsilon_l \cdot \bar{R}^{IV} - \frac{1}{2} \varepsilon_{\perp} \cdot w^{IV}; \quad u_5 = \varepsilon_l \cdot \bar{R}^{IV} + \frac{1}{2} \varepsilon_{\perp} \cdot w^{IV} \quad (6.5)$$

were u_2 , u_3 , u_4 and u_5 are the stress-free displacement at the interfaces I/II, II/III, III/IV and IV/V respectively (see Fig. 6–16 (b)).

The stress-free expansion ($\varepsilon_{\perp}, \varepsilon_l$) can be combined in various ways. The amount of lateral and perpendicular strain can vary, but in order to obtain the required excess volume the following relation must be fulfilled:

$$\varepsilon_{\perp} + 2\varepsilon_l = 3\bar{\varepsilon} \quad (6.6)$$

with $\bar{\varepsilon}$ the average strain required by the volume excess. Since the displacements are not independent, it is more convenient to describe both strain components by a strain coefficient η leading to the following expressions:

$$\varepsilon_{\perp} = (1 + \eta) \bar{\varepsilon}; \quad \varepsilon_l = (1 - \frac{\eta}{2}) \bar{\varepsilon} \quad (6.7)$$

This aspect coefficient may vary in the range from $\eta = -1$ to $\eta = 2$ and these limits correspond to purely lateral and purely perpendicular strain. Replacing the strains in 6.4 and 6.5 by the new parameter η one obtains for the stress-free displacements:

$$\begin{aligned} u_2 &= (1 - \frac{\eta^{II}}{2}) \bar{\varepsilon} \cdot \bar{R}^{II} - \frac{(1 + \eta^{II})}{2} \bar{\varepsilon} \cdot w^{II} \\ u_3 &= (1 - \frac{\eta^{II}}{2}) \bar{\varepsilon} \cdot \bar{R}^{II} + \frac{(1 + \eta^{II})}{2} \bar{\varepsilon} \cdot w^{II} \end{aligned} \quad (6.8)$$

$$\begin{aligned}
 u_3 &= \left(1 - \frac{\eta^{IV}}{2}\right) \bar{\varepsilon} \cdot \bar{R}^{IV} - \frac{(1 + \eta^{IV})}{2} \bar{\varepsilon} \cdot w^{IV}; \\
 u_4 &= \left(1 - \frac{\eta^{IV}}{2}\right) \bar{\varepsilon} \cdot \bar{R}^{IV} + \frac{(1 + \eta^{IV})}{2} \bar{\varepsilon} \cdot w^{IV}
 \end{aligned} \tag{6.9}$$

The elasticity problem required for the second step can be solved analytically. In order to have mechanical equilibrium for a problem of spherical symmetry, the required elastic displacements must have the following form:

$$u^i(r) = a^i \cdot r + \frac{b^i}{r^2} \tag{6.10}$$

with two possible constants a^i and b^i as described by Landau and Lifschitz [Landau 89]. The superscript $i = I, II, III, IV, V$ indicates the material layers in sequence of growing radius. Thus, using the displacement field (6.10), one gets strain and stress components of the following form:

$$\varepsilon_{rr} = a^i - \frac{2 \cdot b^i}{r^3}; \quad \text{and} \quad \varepsilon_{\theta\theta} = \varepsilon_{\varphi\varphi} = a^i + \frac{2 \cdot b^i}{r^3} \tag{6.11}$$

$$\sigma_{rr} = \frac{E}{1 - 2 \cdot \nu} \cdot a^i - 2 \frac{E}{1 + \nu} \cdot \frac{b^i}{r^3} \tag{6.12}$$

$$\sigma_{\theta\theta} = \sigma_{\varphi\varphi} = \frac{E}{1 - 2 \cdot \nu} \cdot a^i + \frac{E}{1 + \nu} \cdot \frac{b^i}{r^3}$$

where E and ν are the Young modulus and Poisson ratio, respectively and they are assumed in first approximation to be identical for all materials. Due to spherical symmetry, all shear components vanish. The following conditions must hold in order to ensure the continuity of the matter at the interfaces:

$$\begin{aligned}
 u^I(R_1) &= 0 \\
 u^I(R_2) &= u_2 + u^{II}(R_2) \\
 u^{II}(R_3) + u_3 &= u^{III}(R_3) \\
 u^{III}(R_4) &= u_4 + u^{IV}(R_4) \\
 u^{IV}(R_5) + u_5 &= u^V(R_5)
 \end{aligned} \tag{6.13}$$

The balance of forces requires that the normal stresses at the interfaces must be identical and the normal stress at the external surface must be zero:

$$\begin{aligned}
 \sigma_{rr}^I(R_2) &= \sigma_{rr}^{II}(R_2) \\
 \sigma_{rr}^{II}(R_3) &= \sigma_{rr}^{III}(R_3) \\
 \sigma_{rr}^{III}(R_4) &= \sigma_{rr}^{IV}(R_4) \\
 \sigma_{rr}^{IV}(R_5) &= \sigma_{rr}^V(R_5) \\
 \sigma_{rr}^V(R_6) &= 0
 \end{aligned} \tag{6.14}$$

Solving the above ten equations one is able to determine the ten parameters if the stress-free strains u_2, u_3, u_4 and u_5 are taken for granted. The solutions for the a^i and b^i are of the form:

$$\begin{aligned}
 a^i &= a^{i-1} + (-1)^{(i-1)} \cdot \frac{1}{1+\gamma} \cdot \frac{u_i}{R_i} \\
 b^i &= b^{i-1} + (-1)^{(i-1)} \cdot \frac{\gamma}{1+\gamma} \cdot u_i \cdot R_i^2
 \end{aligned} \tag{6.15}$$

with $i = II, III, IV, V$ for a^i and $2, 3, 4, 5$ for b^i respectively and $\gamma = \frac{1+\nu}{2 \cdot (1-2 \cdot \nu)}$.

For a^I and b^I we have:

$$a^I = \frac{\frac{R_5^3}{R_6^3} \cdot \frac{u_5}{R_5} - \frac{R_4^3}{R_6^3} \cdot \frac{u_4}{R_4} + \frac{R_3^3}{R_6^3} \cdot \frac{u_3}{R_3} - \frac{R_2^3}{R_6^3} \cdot \frac{u_2}{R_2} - \frac{u_5}{R_5} + \frac{u_4}{R_4} - \frac{u_3}{R_3} + \frac{u_2}{R_2}}{(1+\gamma) \cdot \left(1 + \frac{1}{\gamma} \cdot \frac{R_3^3}{R_6^3}\right)} \tag{6.16}$$

$$b^I = -a^I \cdot R_I^3 \tag{6.17}$$

Since the stress-free strains u_2, u_3, u_4 and u_5 depend on the aspect coefficients η^{II} and η^{IV} , the final completely analytical expression for the elastic fields depends only on the two coefficients η^{II} and η^{IV} .

The strain aspect coefficient is not controlled a-priori by any simple geometric requirement but, as usual, the nature will find a way to establish the lowest elastic energy state and by that the optimum strain aspect coefficients. Thus, it

is necessary to calculate the elastic energy density (6.18), integrate on the total specimen volume (6.19) and afterwards to minimize the total energy expression with respect to η^{II} and η^{IV} .

$$w^i(r) = \frac{1}{2} \sigma_{rr} \varepsilon_{rr} + \sigma_{\theta\theta} \varepsilon_{\theta\theta} = \frac{3}{2} \cdot E \left[\frac{(a^i)^2}{(1-2\nu)} + \frac{2}{1+\nu} \cdot \frac{(b^i)^2}{r^6} \right] \quad (6.18)$$

$$W_{tot} = 4\pi \sum_{i=1}^5 \int_{R_i}^{R_{i+1}} w^i(r) \cdot r^2 dr \quad (6.19)$$

with $i = I, II, III, IV, V$ respectively 1, 2, 3, 4, 5.

In the following, the results of the above described calculations are exemplified for product layer thicknesses equal to the experimentally obtained reaction thicknesses. For the model calculation, a homogeneous Young modulus $E = 90$ GPa and a Poisson ratio of $\nu = 0.345$ as average of the values of Al and Cu were used. The total thickness of the layers is 45 nm (initial state $thickness_{layer I} = thickness_{layer III} = thickness_{layer V} = 15$ nm and afterwards $thickness_{layer I} = 15$ nm $- \frac{1}{2} w^{II}$, $thickness_{layer III} = 15$ nm $- \frac{1}{2}(w^{II} + w^{IV})$, $thickness_{layer V} = 15$ nm $- \frac{1}{2} w^{IV}$). The radius is $R_1 = 30$ nm except for the simulation of the curvature dependence where R_1 varies from 0.1 to 10 000 nm.

In Fig. 6–17 the hydrostatic stress within the specimen is presented for product layers thicknesses $w_i = 5.9$ nm and $w_o = 3.8$ nm vs. strain aspect. One can observe easily in the layer I the hydrostatic stress changes from compressional ($\sigma_{hydrost.} < 0$) to dilatational ($\sigma_{hydrost.} > 0$). Since the planes representing the hydrostatic stress in the layers I, III, V intersect each other, the difference between the stress in I and III as well as III and V may change their sign by variation of η^{II} and η^{IV} .

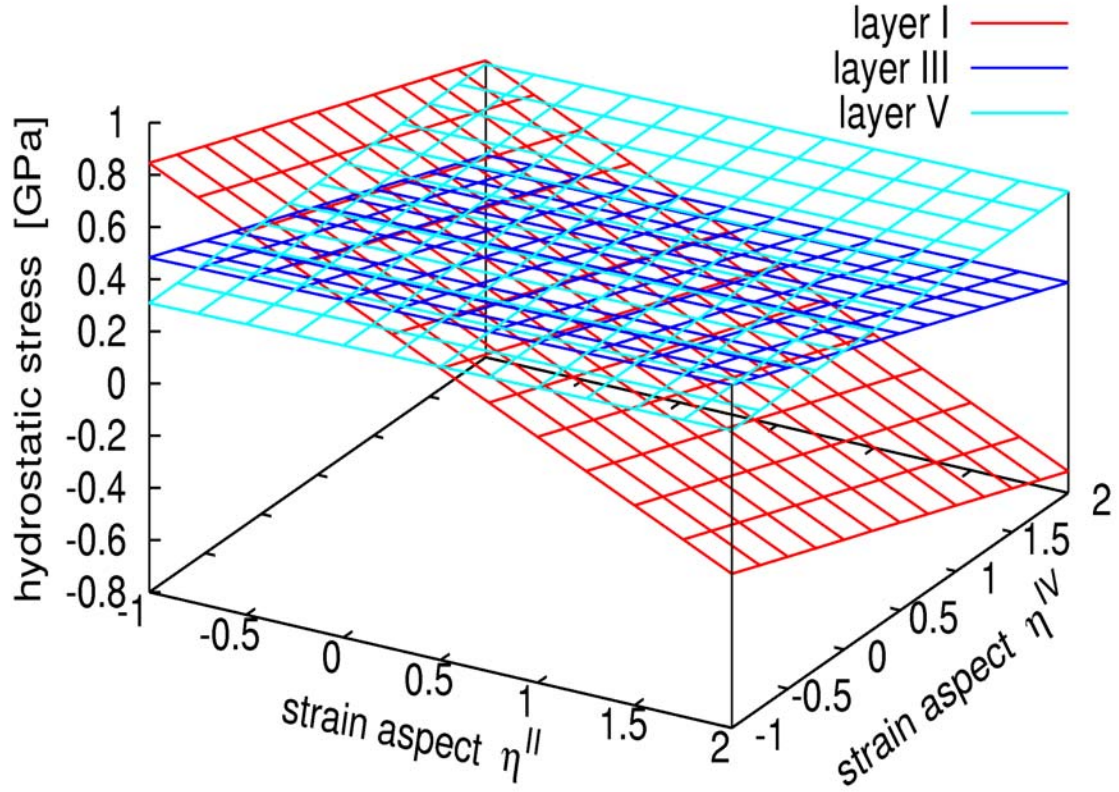


Fig. 6–17: Dependence of hydrostatic stress in layers I, III and V versus strain aspects η^{II} and η^{IV} . The actual geometry is R_1, R_2, R_3, R_4, R_5 and $R_6=30.00, 42.05, 47.95, 58.10, 61.90$ and 75.00 nm, corresponding to 5.9 and 3.8 nm thickness of the product layers.

Having the values for all the stress components it is easy to calculate the energy landscape as a function of the strain aspects η^{II} and η^{IV} and to determine the optimum strain aspects for which the elastic energy reaches its minimum value as exemplified in the next figure (Fig. 6–18).

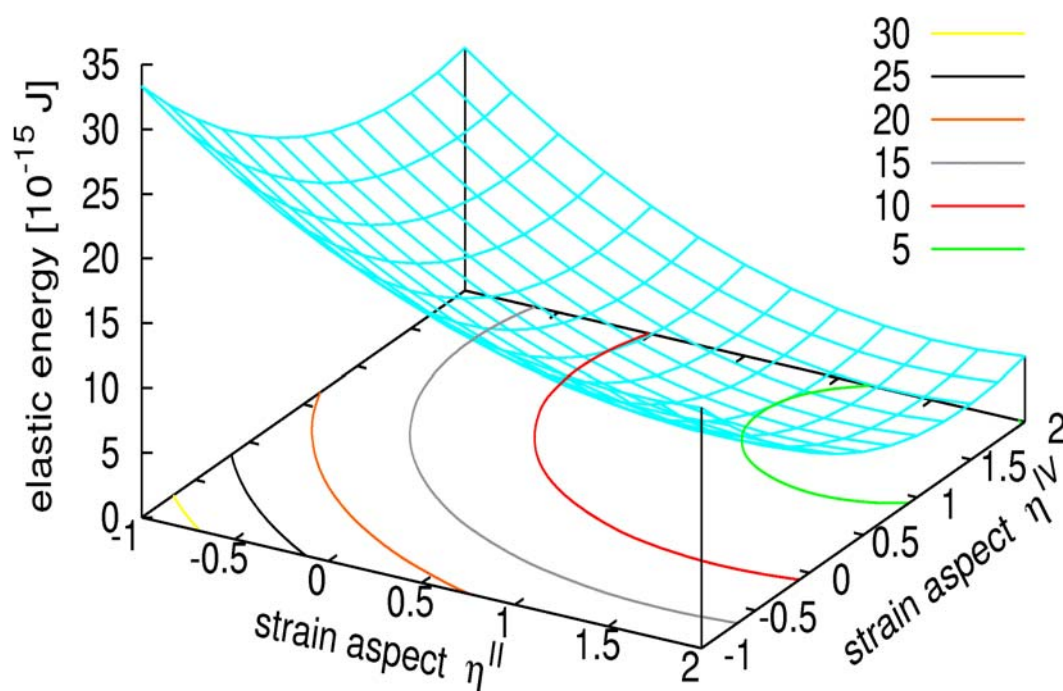
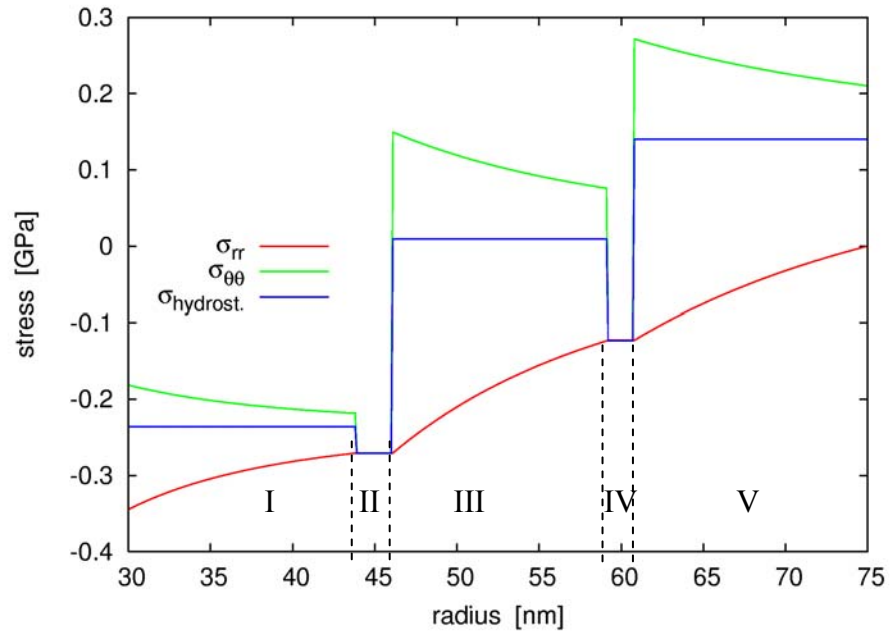
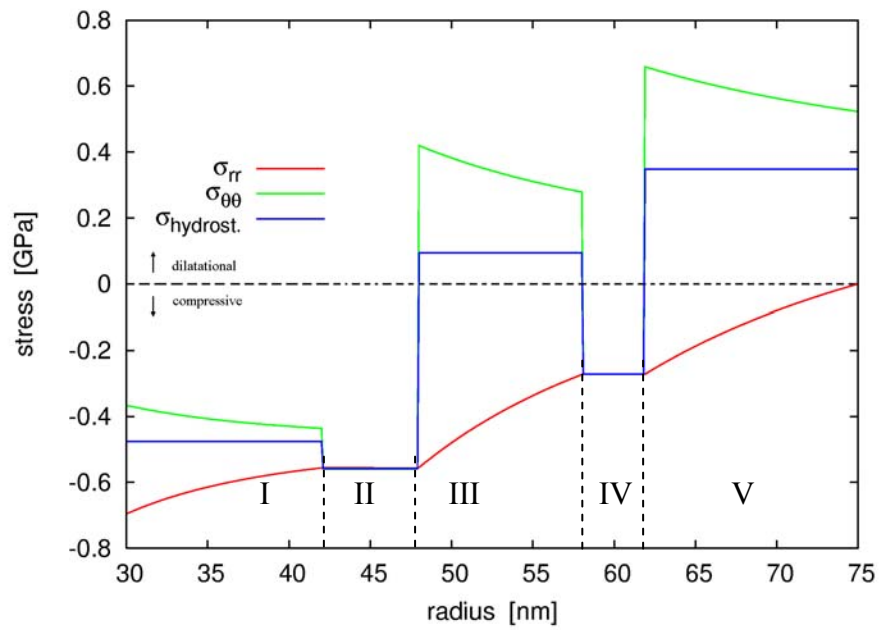


Fig. 6–18: Dependence of elastic energy versus strain aspects η^{II} and η^{IV} (actual geometry R_1, R_2, R_3, R_4, R_5 and $R_6=30.00, 42.05, 47.95, 58.10, 61.90$ and 75.00 nm, corresponding to 5.9 and 3.8 nm thickness of the product layers).

At the optimum strain aspect of minimum elastic energy ($\eta^{II}=1.58$, $\eta^{IV}=1.46$), the hydrostatic stress levels of the inner layer I and the reaction product layer II are not very different, but the difference becomes very high starting with layer III and further layers (see Fig. 6–19). To identify the origin of additional driving forces to the atomic transport, it is important to notice in Fig. 6–19 that the hydrostatic stress is always constant within a layer, but jumps discontinuously at the interfaces. This is a direct consequence of expressions (6.12), if appropriate components $3 \cdot \sigma_{hydrost.} = \sigma_{rr} + 2 \cdot \sigma_{\theta\theta}$ are added.



a)



b)

Fig. 6–19: Profile of hydrostatic stress and its two contributions plotted versus the radial position, calculated with the optimum strain aspect for two different thickness sets: 2.2 and 1.6 nm (a) and 5.9 and 3.8 nm (b).

The next figure (Fig. 6–20) demonstrates that the effects described and discussed here are dependent on the multilayer curvature. Doing the same calculation for a nearly planar system ($1/R \approx 0$) the hydrostatic pressure in all the layers vanishes and as observed from the optimum strain aspect the expansion is practically reduced to a perpendicular one. However, for curvature radii smaller than approximately 300 nm the elastic stress level may exceed 20 MPa . Such a value of the elastic stress allows a significant influence on diffusion as discussed in section 6.6 and may furthermore initiate plastic flow in the terminating layers.

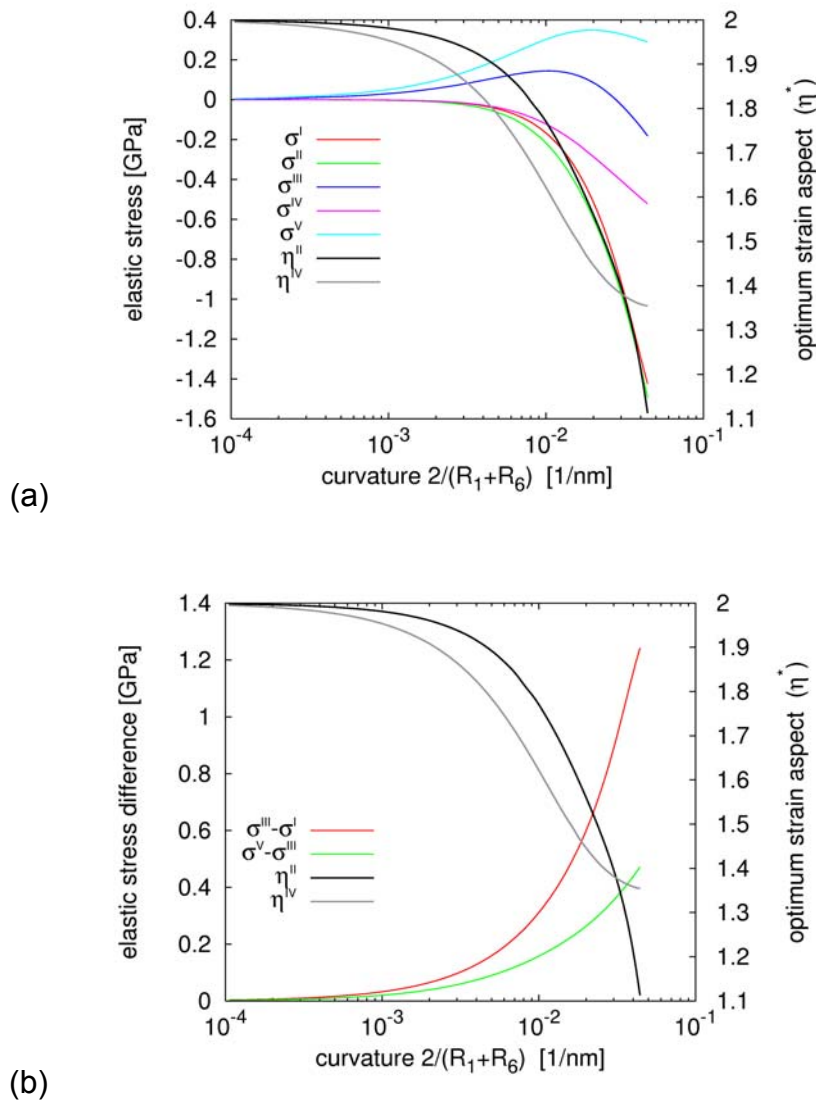


Fig. 6–20: Hydrostatic stress and optimum strain aspect (a) and stress difference (b) versus mean interfacial curvature (for 5.9 and 3.8 nm layer thicknesses)

The model calculation predicts a significant dependence of the optimum strain aspects as well as the hydrostatic stress on the thickness of the reaction product layers as shown in Fig. 6–21. Therefore, the elastic driving forces should increase during the reaction. However, the increase in the driving forces predicted by elasticity may be limited by relaxation or creep within the upper layers, particularly in the layers III and V where the stress reaches rather high values. As a consequence, it is possible that a nearly constant stress of opposite sign may establish on both sides of each product layer. This way, the absolute value of the stress may be controlled by the yield strengths of the materials.

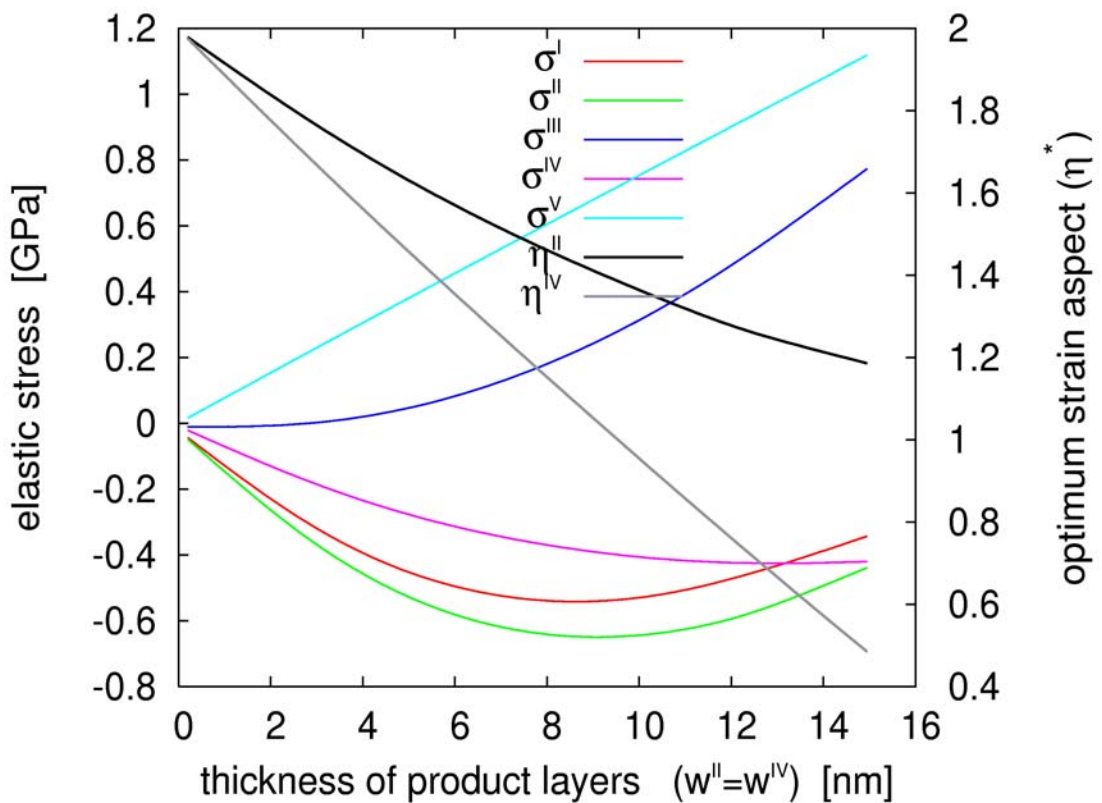


Fig. 6–21: Hydrostatic stress and strain aspect versus thickness of reaction product ($R_1 = 30$ nm, $R_6 = 75$ nm).

6.5 Laplace tension

Beside volume excess of the product phase presented in the previous section, a finite difference of hydrostatic pressure may be alternatively explained by Laplace tension if one takes into account the curved geometry of the samples.

During the formation of the product layer, two interfaces θ'/Cu and θ'/Al are produced. Let us assume, for the sake of simplicity, that they have the same surface tension γ .

By Laplace tension $\sigma = \frac{2\gamma}{r}$, the hydrostatic pressure increases when crossing an interface from the outer to the inner side. For example due to the formation of the inner phase sketched in Fig. 6–16 (b) a finite difference in hydrostatic stress

$$\Delta\sigma = \frac{2\gamma}{R_2} + \frac{2\gamma}{R_3} \approx \frac{4\gamma}{\bar{R}''} \quad (6.20)$$

(definition of radii according Fig. 6–16 (b)) exists between the two metals embedding the reaction product, while the stress inside each layer is constant. A mean radius of 30 nm and a surface tension of 150 mJ/m^2 , which are quite reasonable numbers for experimental conditions as presented in this work, lead to an estimation for the order of magnitude of the hydrostatic stress difference of about 20 MPa .

6.6 Stress impact on the diffusion rate

Hydrostatic pressure will modify the chemical potentials of the different species inside the sample. As previously mentioned, the hydrostatic stress is homogeneous inside the individual layer and therefore, gradients of the chemical potential may only be modified at the interlayer boundaries. Especially the equilibrium of vacancies may be significantly disturbed due to their large formation volume which is close to a complete atomic volume Ω . The mechanism which is described in the following is based on the Kirkendall effect. Shortly, this can be summarized as follows: If the two atomic species have different mobilities inside the newly formed intermetallic, the middle surface of the product layer will shift from its original position. If this shift is directed to lead to a relaxation of the stress induced by the volume expansion, the interdiffusion will be accelerated and vice versa.

Based on a vacancy mechanism and neglecting complicating aspects like thermodynamic factors, one may formulate for the transport currents of both atomic species the following expressions:

$$\begin{aligned} j_A &= -D_A \frac{dc_A}{dx} + D_A \frac{v_A}{v_V} \frac{dc_V}{dx} \\ j_B &= -D_B \frac{dc_B}{dx} + D_B \frac{v_B}{v_V} \frac{dc_V}{dx} \end{aligned} \quad (6.21)$$

In analogy to the Darken equations this leads to the interdiffusion current to:

$$\tilde{j} = -[v_B D_A + v_A D_B] \cdot \frac{dc_B}{dx} - \frac{v_A v_B}{v_V} [D_A - D_B] \cdot \frac{dc_V}{dx} \quad (6.22)$$

with D_A , D_B the individual diffusion coefficients of species A and B, v_A , v_B are the atomic fractions, c_A and c_B are the volume concentrations and c_V , v_V are the corresponding quantities for vacancies. The first term on the right hand side of the previous equation represents the conventional Darken interdiffusion term derived under the assumption of vacancy equilibrium throughout the diffusion

zone, while the second term represents the additional driving force induced by non-equilibrium vacancy densities.

Under the assumption $w \ll r$ in the steady state, the concentration profile across the newly formed product layer follows a linear function. In this case, the gradients might be written:

$$\frac{dc_B}{dx} = \frac{\Delta c_B}{w}, \quad \frac{dc_V}{dx} = \frac{\Delta c_V}{w} \quad (6.23)$$

with w the thickness of the product layer.

Taking for example the case of the inner interface in Fig. 6–16 (b), a difference in vacancy density is induced by the hydrostatic stresses on both sides of the product layer inside the layers *I* and *III*. Since the formation volume of a vacancy equals approximately the atomic volume Ω , we have

$$\Delta c_V = \Delta c_0 \left(\exp \left[\frac{\sigma_{hydrost.}^{III} \Omega}{kT} \right] - \exp \left[\frac{\sigma_{hydrost.}^I \Omega}{kT} \right] \right) \approx c_0 \cdot \frac{\Delta \sigma \Omega}{kT} \quad (6.24)$$

where c_0 denotes the equilibrium density of vacancies.

At this point one can estimate the possible effect on the difference in vacancy density. Let us assume the mole fractions $v_A=2/3$, $v_B=1/3$ and $D_A \gg D_B$, so that all terms containing D_B may be neglected. There are no data available in the literature for the individual mobilities inside the metastable θ' phase. Therefore, we just guess that the majority component of the ordered intermetallic is the much faster diffusing species. Experimentally by APT measurements, the compositional existence range of the reaction product was determined to $\Delta c_B = 7.5 \text{ at.}\%$ and the apparent diffusion coefficients of the two inverse stacking sequences differ by a factor 2.6 ($D_{Cu \text{ on } Al} = 1 \times 10^{-20} \text{ m}^2/\text{s}$ and $D_{Al \text{ on } Cu} = 3.9 \times 10^{-21} \text{ m}^2/\text{s}$), so that the required stress difference on both sides of the growing product is estimated to:

$$\frac{\tilde{j}_{CuonAl}}{\tilde{j}_{AlonCu}} \approx \frac{\frac{1}{3} D_A \frac{\Delta c_B}{w} + \frac{2}{9} D_A \frac{1}{kT} \frac{\Delta \sigma}{w}}{\frac{1}{3} D_A \frac{\Delta c_B}{w} - \frac{2}{9} D_A \frac{1}{kT} \frac{\Delta \sigma}{w}} = \frac{\Delta c_B + \frac{2}{3} \frac{\Delta \sigma}{kT}}{\Delta c_B - \frac{2}{3} \frac{\Delta \sigma}{kT}} = 2.6 \quad (6.25)$$

$$\Rightarrow |\Delta \sigma| \approx 0.67 \cdot kT \cdot \Delta c_B \cong 18 \text{ MPa} \quad (6.26)$$

Similarly, for the Laplace tension model, the phase boundaries may serve as effective point defect source or sink. Thus, by inwards transport of a vacancy and annihilation at the inner interface, elastic energy is relaxed. The resulting driving force to the transport of vacancies is conveniently expressed by a finite difference of the vacancy concentration at opposite boundaries of the product layer analogous to the previous excess volume model:

$$\Delta c_v = \Delta c_0 \left(1 - \exp \left[\frac{\Delta \sigma_{hydrost.} \Omega}{kT} \right] \right) \approx 4 c_0 \cdot \frac{\gamma \Omega}{r kT} \quad (6.27)$$

where Ω denotes the atomic volume which approximates the formation volume of a vacancy, and c_0 is the equilibrium density of vacancies.

For $\bar{R}^{II} = 35 \text{ nm}$ and $\bar{R}^{IV} = 45 \text{ nm}$ curvature radii, using the same parameter as earlier for mole fractions, compositional existence range of the phase ($v_A=2/3$, $v_B=1/3$ and $\Delta c_B=7.5 \text{ at.}\%$) and the same assumptions concerning the mobilities and the steady state diffusion ($D_A \gg D_B$ and $w \ll r$) one can estimate the mean interfacial energy from the ratio of the atomic currents:

$$\frac{\tilde{j}_{CuonAl}}{\tilde{j}_{AlonCu}} = \frac{\Delta c_B + \frac{8}{3} \frac{\gamma}{\bar{R}^{II} kT}}{\Delta c_B - \frac{8}{3} \frac{\gamma}{\bar{R}^{IV} kT}} = 2.6 \quad (6.28)$$

Solving quantitatively the latter equation, a value of $\gamma = 190 \text{ mJ/m}^2$ is determined which leads straight forward to an equivalent hydrostatic pressure of about 18 MPa per interface.

Measuring reliably interfacial energies of a metastable phase is a difficult task and no experimentally determined literature data were found. However, very recently theoretical treatments concerning the energy of the θ'/Al interface by first principle [Vaithyan. 04] or embedded atom methods [Hu 06] have been published. For the coherent interface, values from 156 to 190 mJ/m² are calculated which are in very good agreement with the estimated values required in order to explain the experimentally observed asymmetry in product phase thickness during the reaction of Al/Cu multilayers deposited on curved substrate.

6.7 Discussion and conclusions

The experimental results presented above demonstrate clearly that atomic transport on the nanometer length scale can deviate significantly from a near to equilibrium situation that could be described by a unique diffusion coefficient. It is practically impossible to understand different reaction rates induced by a different layer stacking sequence in the case of a macroscopic planar diffusion couple. Compared to macroscopic samples, in the nano-structured ones distinctive features are present like very high concentration gradients and interfacial contributions. Consequently, during the solid state reaction considerable local stress may develop leading to significant deviation from the thermodynamic equilibrium of point defect densities.

For the hydrostatic pressure which develops during the reaction two different models were presented. The first one is based on the excess volume of the θ' product phase under the assumption of equal partial volume of Al and Cu. The second model is based on the Laplace tension which implies an increase in the hydrostatic pressure by crossing the interface from the outer to the inner side due to surface tension contributions.

The very simple and clear experimental observation requires a complicated theoretical explanation based on excess volume model. In order to describe the effect quantitatively atomic mechanisms of diffusion, elasticity, plasticity and creep must be intercorrelated.

Taking into account how complex the model should be in order to consider the effects of all these complicated mechanisms, the presented quantitative analysis is still incomplete, since it does not include the plasticity and creep mechanisms in a stringent manner. The elastic description, based on the adaptation of stress-free reaction induced strain to the sample geometry, is at least able to predict hydrostatic stresses of opposite sign at both sides of each of the reaction products. The direction of the stress difference is indeed compatible to the direction of the observed asymmetry and the expected kinetic properties of the forming intermetallic. Furthermore, the calculated levels of stress are more than sufficient to explain the magnitude of the observed difference in growth rate. Thus, the validity of this interpretation in terms of reaction-induced stress is very reasonable.

Furthermore, additionally to the excess volume calculated stress values one can take into account also a contribution of the different partial volumes of *Al* and *Cu*. Thus, the hydrostatic stress evolve for all the product phase thicknesses from compressive in the inner layers (usually *I* and *II* and *IV*) to dilatational for the outer layers, e.g. Fig. 6–19. Comparing the simulation results concerning the hydrostatic stress with the experimentally obtained thicknesses of the product layer it is easy to observe that the stress will be reduced if *Al* – with a volume of 16.603 \AA^3 compared to 11.809 \AA^3 *Cu* volume – diffuses away from the layer under compressive stress. That means the *Al* current will have an extra component due to stress reduction – extra driving force for *Al* diffusion towards layers with a larger radius of curvature. Vice versa, diffusion of *Al* from dilatational region to compressive region will increase the stress which means that there is an unfavourable situation – an extra driving force against the *Al* diffusion towards smaller radii regions. Thus, the stress reduction effect may explain the thickness difference of the reaction products at the two different

interfaces. This explanation, which is actually an example of the Le Chatellier Principle, is schematically summarised in the following picture (Fig. 6–22).

Remarkably, in contrast to the Gösele and Tu model [Gösele 82] which predicts parabolic growth only for simultaneously growing phases, the experiment revealed clear parabolic growth for a single product phase for both layer stacking sequences (*Al* on *Cu* and vice versa). This implies that the total driving force across the complete reaction zone must obviously stay constant, so that the growth rate decreases inversely proportional to the layer thickness. By contrast, the elastic calculation predicts an increase in the stress with respect to the thickness growth. This means that a kinetic exponent significantly larger than $\frac{1}{2}$ would be expected in the purely elastic model. This discrepancy to the experiment suggests that relaxation of the very pronounced stress must take place during the diffusive reaction. This way, the stress becomes limited to an almost constant value that is controlled by yield strength or creeping properties of the sample materials. At present, this model is not able to take these influences into account.

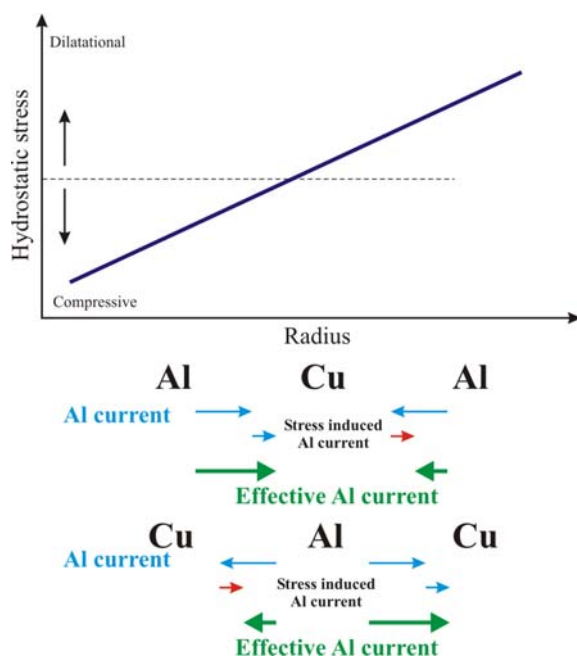


Fig. 6–22: Schematic representation of Al transport current under the influence of the hydrostatic stress.

However, turning it into an advantage, experiments of the described scheme may be used to determine experimentally the actual level of stress evolving during the reaction. In the studied case, the stress difference amounts to 18 MPa , which may be equally distributed with opposite sign to both sides of the reaction layer so that a local hydrostatic stress of $\sigma_{\text{hydrost.}} = \pm 9 \text{ MPa}$ results. This specific value determined by the analysis still depends on the partial mobilities inside the forming intermetallic. For the particular intermetallic phase studied in this work there is no reliable data in the literature. Therefore, it is recommended to repeat analogous experiments with reaction couples, for which the required kinetic data are known more completely.

On the other hand, taking into account the Laplace tension $\sigma = \frac{2\gamma}{r}$, one finds reliable values of the interfacial energy and hydrostatic pressure. Thus, the asymmetry in growth rate might be explained very well by this approach, since the hydrostatic stress is constant during the reaction and this explains also the experimentally observed parabolic growth on both interfaces.

Nevertheless, since both theoretical approaches predict a difference in the hydrostatic stress between the two initial interfaces it is presumable that the experimentally observed asymmetry is a result of a combination of the two of them.

7 Summary and outlook

In this work very small length scale *Cu/Py* and *Al/Cu* thin films required by modern electronic applications were successfully investigated regarding their thermal reaction and stability, the early interreaction stages and stress influence, respectively. These investigations were possible only by using new experimental tools like Atom Probe Tomography and Focussed Ion Beam (FIB) with outstanding spatial and chemical resolution. The local chemical analyses were conducted by APT and they showed considerably more complex reaction mechanisms than usually assumed in the layered geometry models.

For the first time, the *Cu/Py* multilayer system exhibiting giant magneto-resistance effect was microscopically analyzed over a large temperature range using APT with its outstanding spatial resolution. Contrary to the usual presumption that a destroyed layered geometry is the cause of the vanishing GMR effect, the nano-investigation shows remarkably stable layered geometry up to 500°C although annealing at temperatures higher than 250°C already leads to the loss of the GMR effect. It was shown during the reactions in the FIM specimens that the observed microstructural transformations are comparable to the behaviour of planar layer systems with the temperature dependence of the resistivity. This suggests strongly that the identified basic features of the thermal reaction may be reasonably generalized to technical systems.

According to the nano-analysis, the low temperature breakdown of the magneto-resistivity in *Cu/Py* systems is related to the short range intermixing at the interfaces on a width of about 1 nm, which happens homogeneously along the interfaces after annealing at temperatures of 250°C and slightly above,

without destroying the clear layered structure. The degree of intermixing is very well explained by the equilibrium interface Cahn-Hilliard model.

The early stage interreaction at *Al/Cu* sandwich-type thin films showed in contrast to previously investigated *Al/Co* no precursory interdiffusion, but direct formation of a layer of a single reaction product with a 7.5 at.% existence range around the $Al_2Cu - \theta$ phase composition. Since the product phase formed without any nucleation barrier, this was interpreted as a strong suggestion that the product phase is the metastable θ' phase.

Remarkably, a significant asymmetry in the reaction rate with the stacking sequence of the materials was found: although different, the reaction product thicknesses at the two interfaces develop parabolically in time. This was explained as a particularity of the tip-shaped tungsten substrates which enables stress development during the solid state reaction.

An analytical model for the elastic problem was proposed and the results of the simulation could explain the direction of the asymmetry in a good agreement with experimental results. A second interpretation based on the Laplace tension provides an explanation for the parabolic growth of the new product phase. Since both approaches predict an asymmetry of the product layers, it is very probable that the experimental observation is a consequence of a combination of the two approaches.

Thus, this investigation and the models proposed to explain the experimental results may be a starting point for further investigation of actual levels of stress evolving during the reaction if analogous experiments are repeated with reaction couples, for which the required kinetic data are known more completely.

Bibliography

- [Al–Kassab 02] Al–Kassab T, Wollenberger H, Schmitz G and Kirchheim R, „*High resolution imaging and spectrometry of materials*“, Chapt. „*Tomography by Atom Probe Field Ion Microscopy*“, Springer Verlag Berlin, 2003.
- [Allenspach 98] Allenspach R and Weber W, *IBM J. Res. Develop.* **42** (1998) 7.
- [Baibich 88] Baibich M N, Broto J M, Fert A, Van Dau F N, Petroff P, Etienne P, Creuzet G, Fridrich A and Chazelas J, *Phys. Rev. Lett.* **61** (1988) 2472.
- [Bas 95] Bas P, Bostel A, Deconihout B and Blavette D, *Appl. Surf. Sci.* **87/88** (1995) 298.
- [Bennett 90] Bennett W R, Schwarzacher W and Egelhof W F, *Phys. Rev. Lett.*, **65** (1990) 3169.
- [Binasch 89] Binasch G, Grünberg P, Saurenbach F and Zinn W, *Phys. Rev. B* **39** (1989) 4828.
- [Blavette 98] Blavette D, Deconihout B, Chambrelan S and Bostel A, *Ultramicroscopy* **70** (1998) 115.

-
- [Brewer 90] Brewer L, *J. Phys. Chem.* **94**, No. 3 (1990) 1196.
- [Brückner 00] Brückner W, Baunack S, Hecker M, Mönch J I, Van Loyen L and Schneider C M, *Appl. Phys. Lett.* **77** (2000) 358.
- [Cahn 58] Cahn J W and Hilliard J E, *J. Chem. Phys.* **28** (1958) 258.
- [Choi 03] Choi P –P, *Doctoral Thesis*, Universität Göttingen 2003.
- [d’Heurle 97] d’Heurle FM, Gas P and Philibert J, *Def. Diff. Forum* **143–147** (1997) 529.
- [Divinski 02] Divinski S, Hisker F, Kang Y, Lii J S and Herzig Chr., *Z. Metallknd.*, **93** (2002) 256.
- [Divinski 03] Divinski S, Hisker F, Kang Y, Lii J S and Herzig Chr, *Interf. Sci.* **11** (2003) 67.
- [Ene 05] Ene C B, Schmitz G, Kirchheim R and Hütten A, *Acta Materialia* **53** (2005) 3383.
- [Ene1 07] Ene C B, Schmitz G, Kirchheim R and Hütten A, *Surf. Interface Anal.*, **39** (2007) 227.
- [Ene2 07] Ene C B, Schmitz G, Al-Kassab T and Kirchheim R *Ultramicroscopy* **107** (2007) 802.

-
- [Ene3 07] Ene C B, Nowak C and Schmitz G, *Solid State Phen.*, in press.
- [Funamizu 71] Funamizu Y, Watanabe K, *Transp. Jpn. Inst. Met.* **12** (1971) 147.
- [Galinski 07] Galinski H, *Diploma Thesis*, Universität Münster 2007.
- [Giannuzzi 98] Giannuzzi L A, Drown J L, Brown S R, Irwin R B, and Stevie F A, *Microscopy Research and Technique*, **41** (1998) 285.
- [Gösele 82] Gösele U and Tu K N, *J. Appl. Phys.* **53** (1982) 3252.
- [Haasen 96] Haasen P, *“Physial Metallurgy”*, 3rd Edition, Cambridge University Press (1996), 218–219.
- [Hamm 84] Hamm R A and Vandenberg J M, *J. Appl. Phys.* **56** (1984) 293.
- [Hecker 02] Hecker M, Tietjen D, Wendrock J, Schneider C M, Cramer N, Malkinski L, Camley R E and Celinski Z, *J. Magn. Magn. Mater.* **247** (2002) 62.
- [Heitmann 00] Heitmann S, Hütten A, Hempel T, Schepper W, Aloff C, *J. Appl. Phys.* **87** (2000) 4849.
- [Hentzell 83] Hentzell H T G, Thompson R D and Tu K N, *J. Appl. Phys.* **54** (1983) 6923.

-
- [Hu 06] Hu SY, Baskes M I, Stan M and Chen L Q, *Acta Materialia* **54** (2006) 4699.
- [Hütten 99] Hütten A, Mrozek S, Heitmann S, Tempel T, Brückl H and Reiss G, *Acta Materialia* **47** (1999) 4245.
- [Jeske 01] Jeske T, *Doctoral Thesis*, Universität Göttingen 2001
- [Kidson 61] Kidson G V, *J. Nucl. Mat.* **3** (1961) 21.
- [Kirkaldy 58] Kirkaldy J S, *Can. J. Phys* **36** (1958) 917.
- [Kuduz 04]. Kuduz M, *Doctoral Thesis*, Universität Göttingen 2004.
- [Landau 89] Landau L D and Lifschitz E M, „*Elastizitätstheorie*“, Akademie–Verlag Berlin 1989, p. 23.
- [Lang 03] Lang Ch, Schmitz G, *Mat. Sci. Eng. A* **353** (2003) 119.
- [Larson 00] Larson D J, Clifton P H, Tabat N, Cerezo A, Petford-Long A K, Martens R L and Kelly T F, *Appl. Phys. Lett.*, **77** (2000) 726.
- [Larson 01] Larson D J, Cerezo A, Clifton P H, Petford-Long A K, Martens R L, Kelly T F, and Tabat N, *J. Appl. Phys.* **89** (2001) 7517.
- [Larson 04] Larson D J, Petford-Long A K, Ma Y Q and Cerezo A, *Acta Materialia* **52** (2004) 2847.

-
- [Lopez 93] Lopez V M, Sano N, Sakurai T and Hirano K, *Acta metal. Mater.* **41** (1993) 265.
- [Massalski 90] Massalski T B, editor. “*Binary alloy phase diagrams*”, Materials Park OH, ASM International 1990.
- [Matano 33] Matano C, *Japan J. Physics*, **8** (1933) 109.
- [Miller 04] Miller M K, Russel KF, Thompson G B, *Ultramicroscopy* **102** (2004) 287.
- [Miller 89] Miller M K, ‘*Atomprobe Microanalysis*’, MRS Pittsburgh 1989.
- [Miller 96] Miller M K, Cerezo A, Hetherington M G and Smith G D W, “*Atom Probe Microanalysis*”, Claredon Press Oxford 1996.
- [Pretorius 91] Pretorius R, Vredenberg A M, Saris F W and de Reus R, *J. Appl. Phys.* **70** (1991)
- [Mott 36] Mott N F, *Proc. Royal Soc.* **156** (1936) 368.
- [Mott 64] Mott N F, *Adv. Phys.* **13** (1964) 325.
- [Murray 85] Murray J L, *Int. Met. Rev.* Vol. 30, no. 5 (1985) 211–233.
- [NIMS] National Institute for Materials Science – online diffusion database. Available at <http://diffusion.nims.go.jp>
- [Nowak 04] Nowak C, *Diploma Thesis*, Universität Göttingen 2004.

-
- [Parkin 91] Parkin S S P, *Phys. Rev. Lett.* **67** (1991) 3598.
- [Pasichnyy 05] Pasichnyy M O, Schmitz G, Gusak AM and Vovk V, *Phys. Rev. B* **72** (2005) 014118.
- [Ruderman 54] Ruderman M A and Kittel C, *Phys. Rev.* **96** (1954) 99.
- [Schleiwies 01] Schleiwies J, *Doctoral Thesis*, Universität Göttingen 2001.
- [Schmitz 01] Schmitz G, *Habil. Thesis*, Universität Göttingen 2001.
- [Schmitz 07] Schmitz G, Howe J M, Chapt. “*Experimental Methods: High-Resolution Microscopy*” in “*Alloy Physics*” ed. Pfeiler W, Wiley 2007.
- [Thompson 04] Thompson G B; Miller M K, Fraser H L, *Ultramicroscopy* **100** (2004) 25.
- [Tsymbal 01] Tsymbal E Y and Pettifor D G, in “*Solid State Physics*”, edited by Ehrenreich H and Spaepen F (Academic, New York), **56** (2001) 113.
- [Vaithyan. 04] Vaithyanathan V, Wolverton C and Chen L Q, *Acta Materialia* **52** (2004) 2973.
- [van Loyen 00] van Loyen L, Elefant D, Tietjen D, Schneider CM, Hecker M, Thomas J, *J. Appl. Phys.* **87** (2000) 4852.
- [Vovk 03] Vovk V, *Diplome Thesis*, Universität Göttingen 2003.

-
- [Vovk 04] Vovk V, Schmitz G, and Kirchheim R, *Phys. Rev. B.*, **69** (2004) 104102.
- [Zhou 98] Zhou X W and Wadley H N G, *J. Appl. Phys.* **84** (1998) 2301.

Appendix: Macroscopic experiment on the interdiffusion of Cu/Al couple

With the aim to obtain interdiffusion coefficients and to determine the migration of the welding plane, macroscopic diffusion experiments were performed. For that, cylindrically-shaped *Al* and *Cu* disks – 7 mm in diameter, 3 mm thickness – were prepared from 99.9 at% *Al* and 99.999 at% *Cu*. The disks were mechanically polished to less than 0.3 μm roughness. In order to avoid any influence of the natural Al_2O_3 in the diffusion process, the *Al* disks were inserted in the IBS chamber and cleaned by ion beam sputtering. Afterwards, without breaking the vacuum, a 50 nm *Cu* protection layer was deposited. In this way prepared, *Al* and *Cu* disks were clamped together using the holder sketched in Fig A–1. The holder consists of a 50 mm long, 13 mm outer and 8.5 mm inner diameter tube with inner winding and two screws. The specimens are pressed together by the two screws. To avoid any contact with the screws, additionally *Al* and *Cu* 8 mm diameter and 10 mm thick cylinders were placed in between the disks and the screws. Before closing the screws, the samples were centred inside the tube using three small screws posted at 120° as sketched in the Fig. A–1 right hand side. Afterwards, the large screws were tightened and the three small ones used for centring were removed to enable the holder to be sealed in a 15 mm diameter glass tube under *Ar* atmosphere. After sealing, the tubes were placed in a furnace and isothermally annealed at 410°C for 120, 360 and 720 hours and at 525°C for 12 and 24 hours. After the heat treatment the samples are mechanically polished (see Fig. A–2). Composition profiles were determined perpendicular to the initial interface using Energy Dispersive X-ray Microanalysis (EDX).

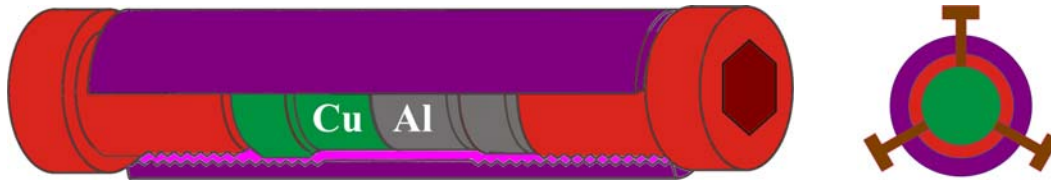


Fig. A–1: Sketch of the specimen holder used for interdiffusion annealing. In the right hand side the sample centring geometry is sketched.

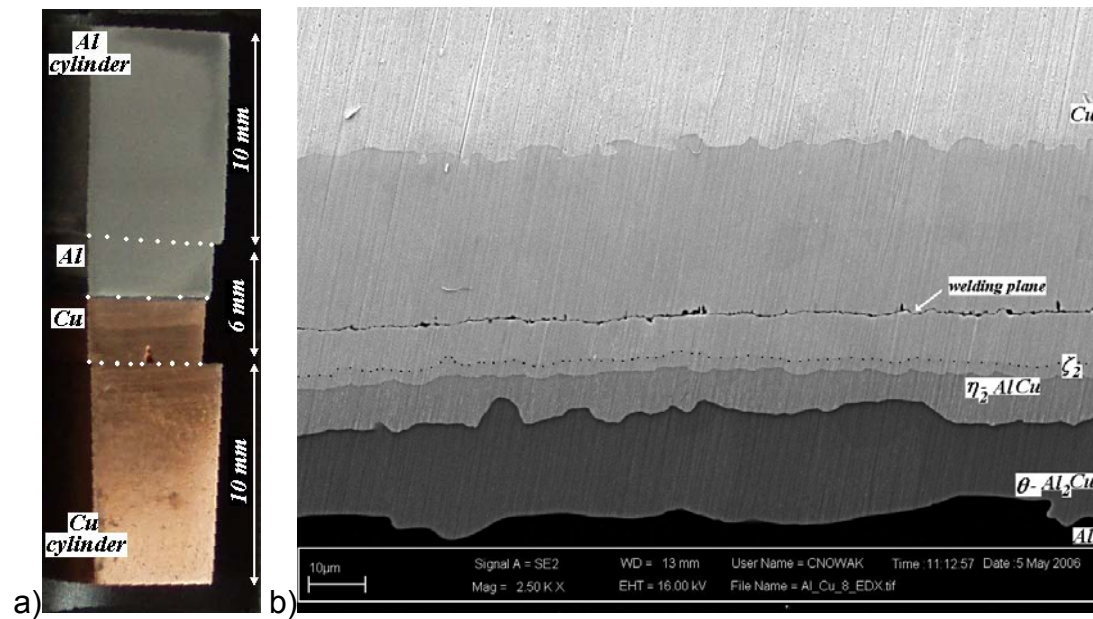


Fig. A–2: (a) Micrograph of the sample used for interdiffusion in an Al/Cu couple. (b) SEM micrograph of a sample after annealing for 360 hours at 410°C.

The composition profiles measured by electron microprobe analysis were used to calculate interdiffusion coefficients. If the sample is annealed for a certain time t at a given temperature T and if the composition profiles is known, then it is possible to determine the interdiffusion coefficient for each concentration using the Matano method [Matano 33]:

$$\tilde{D}(c) = -\frac{1}{2t} \cdot \frac{dx}{dc} \bigg|_c \cdot \int_0^c x(c') dc', \text{ with the condition } \int_0^l x(c') dc' = 0 \quad (\text{A.1})$$

For that, the gradient of the $c(x)$ curve $\frac{dx}{dc}$ and the value of the integral

$\int_0^c x(c') dc'$ must be graphically determined from the concentration curve (Fig.

A-3).

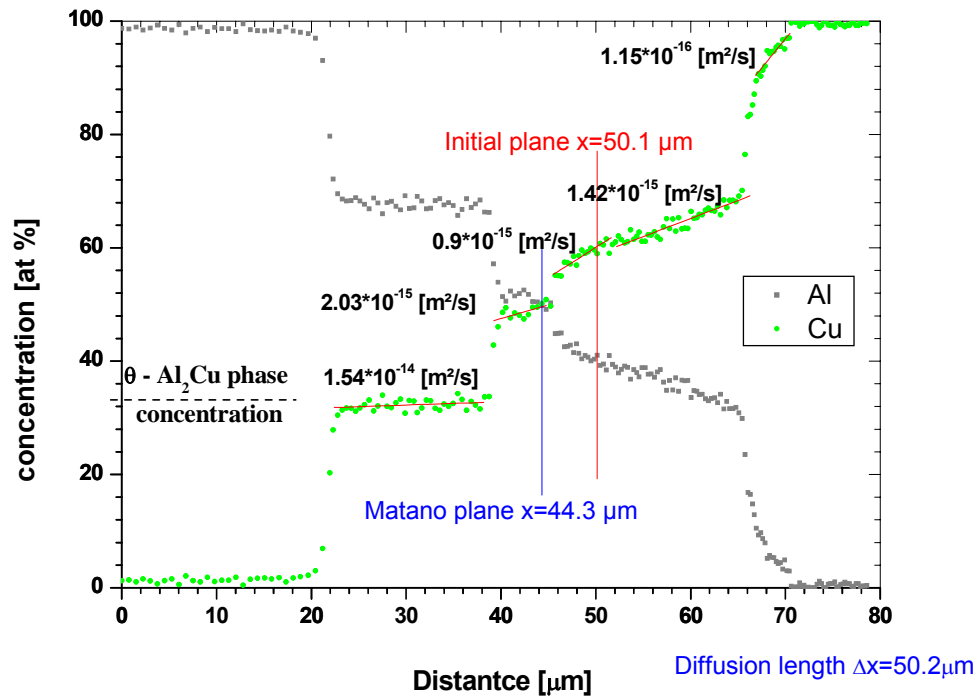


Fig. A-3: Matano evaluation of the interdiffusion coefficients after 410°C annealing for 120 hours. The values of the interdiffusion coefficients are indicated on the figure.

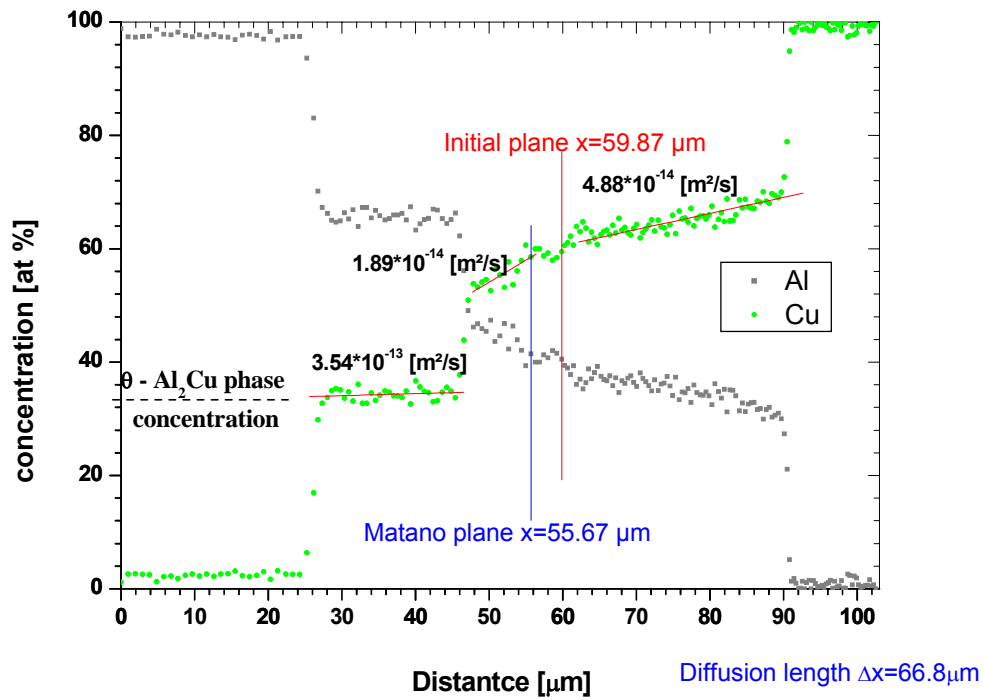


Fig. A-4: Matano evaluation of the interdiffusion coefficients after 525°C annealing for 12 hours. The values of the interdiffusion coefficients are indicated on the figure.

Hence, the literature data [Funamizu 71] for the bulk interdiffusion coefficient of the θ phase were reproduced very well by our macroscopic diffusion experiment. For the 410°C isothermal annealing temperature we obtained $D_{\text{exp}} = 1.1 \times 10^{-14} \text{ m}^2/\text{s}$ while [Funamizu 71] reports $D_{\text{Lit}} = 0.9 \times 10^{-14} \text{ m}^2/\text{s}$. For the sample annealed at 525°C we determined for the interdiffusion coefficient $D_{\text{exp}} = 3.6 \times 10^{-13} \text{ m}^2/\text{s}$ which is in very good agreement with the one reported in the literature $D_{\text{Lit}} = 2.3 \times 10^{-13} \text{ m}^2/\text{s}$.

Acknowledgements

I wish to express my sincere thanks and gratitude to Prof. Dr. Reiner Kirchheim who accepted me as a PhD student and gave me the opportunity to work at the Institute of Material Physics of the University of Göttingen. His scientific support during all this study is particularly acknowledged.

My special thanks to Prof. Dr. Guido Schmitz for reacting to a presentation e-mail I sent, late in one cold winter night of 2002 from Bucharest. I am grateful for the challenging and constructive supervision although he moved shortly after the start of my work to the University of Münster.

I would like to thank PD Dr. Talaat Al-Kassab for the art of always being there and his willingness for scientific and private discussions. I am also thankful to Prof. Dr. H. Teichler, PD. Dr. A. Pundt, Prof. Dr. H.U. Krebs and Prof. Dr. H. Hofsäss for the interesting scientific discussion we have had.

Special thanks to Dr. R. Schwarz for his interest in my work from the first day we met when he surprised me with “*eu vorbește puțin românește*” (I speak a bit Romanian). Our discussions were always useful and run out of time.

I am thankful to Dr. F. Danoix and Prof. Dr. D. Blavette for the pleasant work atmosphere and for the scientific discussions during my short stage in the *Groupe de Physique de Matériaux – Université de Rouen*.

Dr. C. Borchers and Dr. D. Baither (Univ. Münster) I would like to thank for helping me with TEM and for the discussions of these investigations.

Carsten Nowak I address a special Thank You for our cooperation and for the numerous scientific and private discussions we had as last “*Schmitz group*” members. I would like to thank all my former and actual group colleagues like Dr. Christian Lang, Dr. Mario Kuduz, Dr. Christian Kluthe, Dr. Pyuck-Pa Choi, Dr. Daniel Wolde-Giorgis, Dr. Alexander Heinrich, Dr. Ahmed

Shariq, Catharina Wille, Torben Boll, Alexander Mackel, Thomas Rademacher, Malte Schmidt, Michael Sobol, Vitaliy Vovk and Jens Görlich for their help, the scientific discussions and for the very nice time I experienced here.

I would like to thank the technical staff and especially T. Schulz for the nearly problem-free experimental work. The friendly administrative team C. Kuba, I. Saalfeld and K. Haacke I am indebted for helping me with all kind of papers.

I use this opportunity to thank my country mates Elena, Ciprian, Ovidiu, Dante, Mirela, Lucian, Alina, Vlad, Rodica, Ana, Catalin, Mara, Marian and many others, all young scientists in Göttingen or in the neighbourhood for our Romanian evenings brilliantly organized by my wife Emilia.

Last, but definitely not least, I want to thank my family: my wife Emilia, my son Vlad Constantin and our close relatives, for their unconditioned help and support, for their love and patience during these years. *Vă mulțumesc tuturor!*

Lebenslauf

Persönliche Daten

Name:	Ene
Vorname:	Constantin Buzau
Geburtstag und -ort:	08. April 1975, Buzau, Rumänien
Eltern:	Aurelia und Constantin Ene
Staatsangehörigkeit:	rumänisch

Ausbildung

09/1981 – 07/1989	„Scoala Generala Mihailesti“ Grundschule und Gymnasium, Mihailesti/Buzau, Rumänien
09/1989 – 07/1993	„Grup Scolar Industrial Transporturi C.F. Buzau“ Kollegium, Buzau, Rumänien
10/1995 – 07/1999	Physikstudium an der Universität Bukarest, Rumänien
10/1999 – 02/2001	Master in Physik an der Universität Bukarest, Rumänien
Seit 08/2002	Wissenschaftlicher Mitarbeiter am Institut für Materialphysik der Georg - August - Universität zu Göttingen in der Arbeitsgruppe von Prof. Dr. R. Kirchheim

Vorherige Tätigkeiten

11/1999 – 06/2002	Testingenieur Halbleiterbauelemente und Leitung der Testabteilung SC Baneasa SA, Bukarest, Rumänien
-------------------	---

